

pubs.acs.org/CR Review

### **Gas Evolution in Water Electrolysis**

Published as part of Chemical Reviews special issue "Green Hydrogen".

Paul A. Kempler,\* Robert H. Coridan, and Long Luo

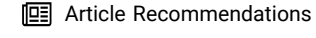


Cite This: Chem. Rev. 2024, 124, 10964-11007

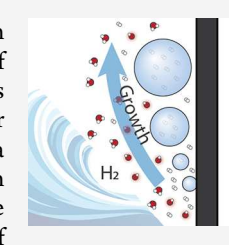


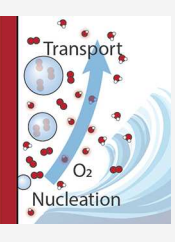
ACCESS I

Metrics & More



**ABSTRACT:** Gas bubbles generated by the hydrogen evolution reaction and oxygen evolution reaction during water electrolysis influence the energy conversion efficiency of hydrogen production. Here, we survey what is known about the interaction of gas bubbles and electrode surfaces and the influence of gas evolution on practicable devices used for water electrolysis. We outline the physical processes occurring during the life cycle of a bubble, summarize techniques used to characterize gas evolution phenomena in situ and in practical device environments, and discuss ways that electrodes can be tailored to facilitate gas removal at high current densities. Lastly, we review efforts to model the behavior of





individual gas bubbles and multiphase flows produced at gas-evolving electrodes. We conclude our review with a short summary of outstanding questions that could be answered by future efforts to characterize gas evolution in electrochemical device environments or by improved simulations of multiphase flows.

#### **CONTENTS**

1. Introduction	10965
1.1. Motivation	10965
1.2. Scope	10966
2. Electrochemical Measurements of Gas-Evolving	
Reactions	10966
3. Terminology, Physics, and Dynamics of Bubbles	10967
3.1. What Is a Bubble?	10967
3.2. Physical Processes Governing Gas Bubbles	
in Electrolyzers	10967
3.2.1. Concentrations, Henry's Law, and	
(Super)saturation	10967
3.2.2. Surface Tension, Laplace Pressure, and	
Contact Angles	10968
3.2.3. Buoyancy Forces	10969
3.2.4. Convective Forces	10969
3.2.5. Electrostatic Forces and Surface	
Charges	10969
3.3. Evolution of Bubbles	10969
3.3.1. Bubble Nucleation	10969
3.3.2. Growth	10971
3.3.3. Detachment	10971
3.3.4. Coalescence	10971
4. In Situ Characterization Techniques	10971
4.1. Electrochemistry	10972
4.1.1. Microelectrode-Based Methods	10972
4.1.2. Nanoelectrode-Based Methods	10974
4.1.3. Nanopore-Based Methods	10975
4.1.4. Scanning Electrochemical Microscopies	10976
4.2. Atomic Force Microscopy (AFM)	10977
4.3. Optical Microscopy	10977

4.3.1. Conventional Microscopy	10977
4.3.2. Fluorescence and Luminescence Mi-	
croscopy	10979
4.3.3. Interference Reflection Microscopy	10980
4.3.4. Dark Field Microscopy	10980
4.3.5. Surface Plasmon Resonance (SPR) Mi-	
croscopy	10980
4.3.6. Particle Tracking Measurements	10981
4.4. Transmission Electron Microscopy (TEM)	10981
4.5. Electrochemical Quartz Crystal Microba-	
lance (EQCM)	10981
5. Electrode- and Device-Level Impacts of Gas	
Bubbles	10982
5.1. Electrode-Level Impacts of Gas Bubbles	10982
5.1.1. Ohmic Contributions	10982
5.1.2. Hyperpolarization and Concentration	
Overpotentials	10982
5.1.3. Bubble-Induced Microconvection	10983
5.2. Device-level impacts of gas bubbles	10983
5.2.1. Gas Evolution in Liquid Alkaline Water	
Electrolysis	10983
5.2.2. Gas Evolution in Proton Exchange	
Membrane Electrolysis	10985
6. Operando Characterization of Water Electrolysis	10986

Received: March 19, 2024 Revised: August 22, 2024 Accepted: August 26, 2024 Published: September 11, 2024





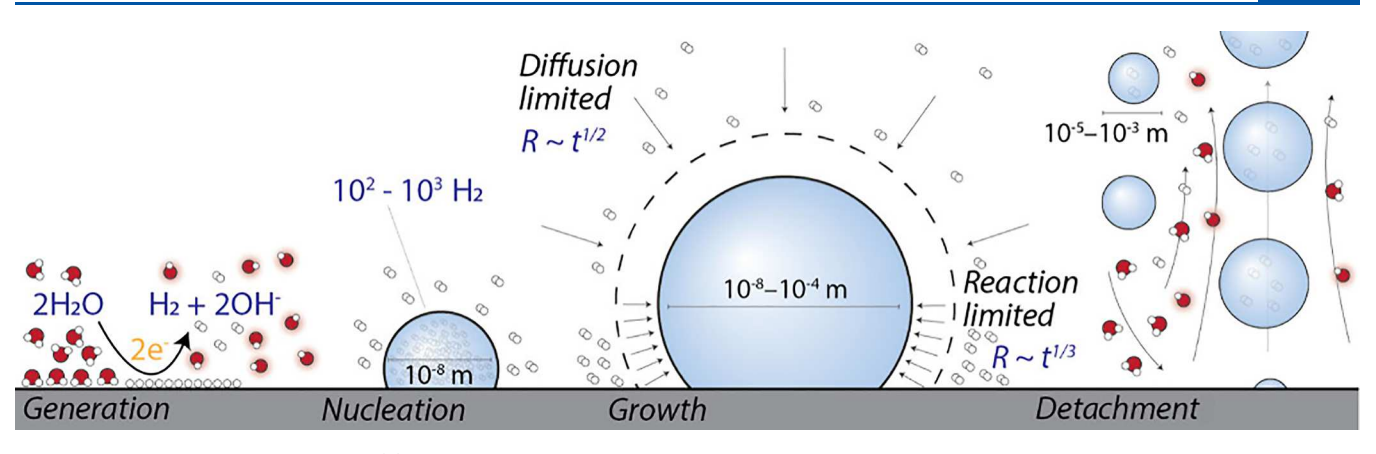


Figure 1. Schematic "life cycle" of a  $H_2(g)$  bubble during the hydrogen evolution reaction from an alkaline electrolyte. Molecules are illustrative in nature and not drawn to scale. The generation of  $H_2$  occurs via the two-electron reduction of water to form hydroxide. Gas bubbles nucleate from as few as a few dozen  $H_2$  molecules on the electrocatalyst surface and then rapidly grow from < 10 nm to reach 10s of  $\mu$ m in diameter. The growth of small bubbles is typically limited by radial diffusion of dissolved  $H_2$  whereas the growth of larger bubbles is limited by the generation of gas at the substrate. Departing gas bubbles at radii 10  $\mu$ m to >1 mm in diameter bring dissolved reaction products away from the electrode surface and are replaced by fresh electrolyte.

6.1. Optical Operando Characterization	10986
6.2. Neutron Radiography Operando Character-	
ization	10987
6.3. X-ray Radiography Operando Characteriza-	
tion	10989
7. Modeling and Simulation	10990
7.1. Molecular Dynamics Simulation of Nano-	
bubbles	10991
7.2. Continuum Models of Individual Bubbles	10991
7.2.1. Nucleation	10992
7.2.2. Steady-State	10992
7.2.3. Dynamics	10992
7.3. Continuum Models of Electrodes	10992
8. Functional Materials for Gas Transport in Electro-	
lyzers	10993
8.1. Controlling Electrode/Gas Interactions	10993
8.1.1. Modified Electrode Surfaces	10993
8.1.2. Control of Catalyst Structure	10995
8.2. Directed Gas Transport	10995
9. Outlook	10996
Author Information	10997
Corresponding Author	10997
Authors	10997
Author Contributions	10997
Notes	10997
Biographies	10997
Acknowledgments	10998
Glossary of Symbols and Abbreviations	10998
References	10998

#### 1. INTRODUCTION

#### 1.1. Motivation

"Green hydrogen" produced via water electrolysis is poised to serve a crucial role in sectors for decarbonization, including ammonia production, heavy-duty vehicles, manufacture of iron and steel, and long-duration energy storage. The devices used to drive water electrolysis, electrolyzers, can be powered by solar or wind electricity in a scalable approach to hydrogen production without concomitant greenhouse gas emissions. The deployment of flexible electrolyzers, following intermittent

and clean electricity, can be accelerated by reducing the upfront capital cost of electrolysis and developing strategies to mitigate system degradation experienced during frequent shutdown. Efficient removal of gases from electrode surfaces can improve the practical current density of a cell, thereby improving the economics and scalability of hydrogen generation via water electrolysis. In terms of energy efficiency, gas bubbles lead to increased electrode overpotentials such that control of gas/liquid interfaces is an important component of electrolyzer design. Moreover, gas bubbles have been implicated in catalyst failure modes that arise during frequent load cycling. Thus, an improved understanding gas—liquid interfaces during water electrolysis can improve electrolysis technologies for producing hydrogen.

A few introductory texts and reviews cover the basic theories of gas evolution at electrodes. Sides is one of the early pioneers of electrochemical engineering aspects of gas evolution and authored a textbook chapter on phenomena occurring during electrolysis. 11 Lubetkin authored an early, tutorial review on the principles governing general bubble evolution. <sup>12</sup> In the past decade, Zhao et al. reviewed recent advancements in understanding bubbles caused by gas-evolving reactions and Angulo et al. reviewed the various ways in which bubbles affect (photo)electrochemical reactors. 10,13 Lohse reviewed both the simulations and experiments on surface attached nanobubbles. 14 Swiegers summarized engineering approaches for managing bubble effects in water electrolysis, with a focus on alkaline electrolysis. 15 Most recently, Li et al. summarized recent literature related to micro- and nanostructured electrodes engineered to control bubbles produced from water splitting. 16 Several more reviews summarize the principles of water electrolysis and the state-of-the-art examples of devices for hydrogen generation. The aim of this review is to provide a comprehensive summary of how gas evolution controls the behavior of electrodes evolving hydrogen and oxygen gas, with a specific emphasis on material relevant to producing hydrogen via water electrolysis installed at the megawatt scale today. Investigations of gases produced at electrode surfaces are as old as the idea of a kinetic overpotential, and this review thus spans well over a century of scientific research.<sup>20</sup> We do not discuss gas-liquid interfaces in the electroreduction of CO2, or photoelectrochemical

devices for water splitting, except where the underlying electrochemical studies have some relevance to physics or design principles for low temperature (<200  $^{\circ}$ C) water electrolysis.

#### 1.2. Scope

A holistic understanding of gas evolution in water electrolysis begins with the fundamental physics of gas liquid interfaces, from the definition of a bubble to the processes controlling the "life cycle" of a gaseous phase on an electrode surface (Figure 1). We first review the physics of gas bubbles, the ways they have been measured, and their implications for water electrolysis. Throughout the review we have endeavored to connect the results of these studies to what is known about the device-level effects of gas bubbles within proton-exchange membrane and alkaline water electrolyzers. We additionally survey the micro- and nanoscale characterization techniques that have been used to study the nucleation, growth, and detachment cycle of individual bubbles at gas-evolving interfaces as well characterize their influence on the local electrochemical environment. We introduce the principles and applications of in situ and operando characterization techniques used to study population level effects of gas bubble films and porous electrodes that are instrumental components of practical water-splitting electrolyzers. Because our understanding of device level impacts of bubbles has been heavily supported by theory and simulations, we review the approaches to modeling gas evolution behavior. Lastly, we discuss the use of functional materials for controlling gas transport and highlight the most promising approaches for controlling gas transport at electrodes evolving hydrogen and oxygen. We conclude our review with a summary of the opportunities for improving our understanding of gas-liquid interfaces in electrochemical devices and designing efficient electrolyzers removing hydrogen and oxygen gases at high current densities.

# 2. ELECTROCHEMICAL MEASUREMENTS OF GAS-EVOLVING REACTIONS

Electrochemical measurements are used to understand the physical processes governing the relationship between current (i) and potential (E) at polarized, gas-evolving interfaces. Most researchers rely on three-electrode measurements to characterize the *i-E* behavior of independent electrodes employed for the hydrogen evolution reaction (HER) or the oxygen evolution reaction (OER). In a typical experiment, the potential of the working electrode (WE) is controlled with respect to a reference electrode (RE) in solution while a counter electrode (CE) drives a complementary half-reaction in a separate region of the cell leading to the measured current response. Only gas bubbles generated between the WE and RE affect the applied WE potential—primarily by increasing the ohmic drop and reducing the effective overpotential at the WE surface (Figure 2a).

The primary benefit of a three-electrode measurement is that it allows for independent assessment of the polarization response for a single gas-evolving WE, which makes it simpler to correlate changes in *E* with changes in the size, coverage, and dynamic behavior of gas bubbles. The limitation is that the configuration of the WE and RE is often impractical and unrealistic compared to the configuration of the same electrode when integrated into an electrolyzer. Thus, the measured effect of gas-evolution on the *i-E* response may only be loosely

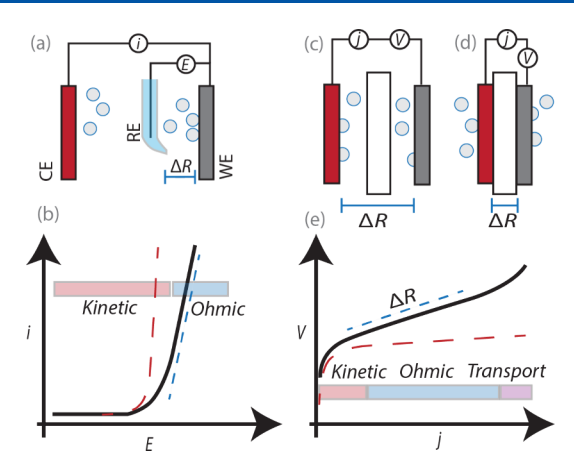


**Figure 2.** (a) Representative configuration for a three-electrode measurement of a WE. The measured potential includes overpotentials at the cathode and resistance between the WE and RE. (b) Representative *i-E* trace for a three-electrode measurement, where the kinetically controlled region is seen to follow an exponential *i-E* relationship (dashed red line) and the potential region under ohmic control is expected to follow a linear *i-E* relationship (dashed blue line). (c,d) Two representative configurations for a two-electrode measurement, (c) traditional and (d) zero-gap, where gas bubbles between the anode and cathode contribute to changes in resistance. (e) Representative *J-V* trace for a two-electrode device, where the process controlling the marginal overpotential transitions from kinetic- to ohmic control, and eventually to transport control with increasing applied current density.

related to device performance. This illustrates the need for methods to characterize electrode performance in practical device architectures.

Practical measurements of the effects of gas bubbles on electrolyzers are often reported based on the cell potential, V, as a function of the applied current density, J, normalized to the projected area of the electrodes. The specific effects of gas bubbles on the electrolyzer can be understood by changes in the J-V behavior of a cell and are often combined with operando characterization of the gas-evolving behavior within the device (Section 6). Two-electrode measurements are typically conducted by measuring the steady-state cell V at a fixed current after allowing the device to reach a pseudo steady-state condition. Reference electrodes have been integrated with solid electrolytes and used to separate the individual polarization response of both the anode and cathode, but these measurements require careful consideration of potential gradients within thin layers of electrolyte.<sup>21,22</sup> Following the nomenclature developed by Sides, the contributions of bubbles to the measured potential at a gasevolving electrode can be separated into ohmic resistance, kinetic overpotentials, and concentration overpotentials. Although the kinetic, ohmic, and transport-controlled regions of the *I-V* response need not occur at the same range of *I*, the general trend of the cell potential being controlled by kinetics at low *J*, ohmic overpotentials dominating the voltage response near the operating current ( $\sim$ 2 A cm<sup>-2</sup> for proton exchange membrane (PEM) electrolyzers), and transport overpotentials only being observed at very high J holds across many devices.

The equilibrium potential,  $E_{eq}$ , for a generalized gas-evolving reaction (eq 1)

$$\nu_{w}W + ze^{-} \rightleftharpoons \nu_{x}X + \nu_{y}Y \tag{1}$$

may be defined by the measured potential at a metallic electrode surface at which the oxidation and reduction reactions occur at equal rates. This potential can be predicted by the Nernst equation (eq 2)

$$E_{eq} = E^0 - \frac{RT}{zF} \sum_{i} \nu_i \ln(\gamma_i c_i)$$
 (2)

where  $\nu_i$  is the stoichiometric coefficient and is taken to be negative for the reactants in the reduction reaction,  $c_i$  is the concentration of a species within the cell,  $\gamma_i$  is the activity coefficient necessary to correct for nonideal solutions (e.g., Section 3.2.1), and  $E^0$  is the standard electrode potential, defined as the equilibrium electrode potential when all species are at standard state. In a gas-evolving experiment, the potential is held away from  $E_{eq}$  leading to a net oxidation or reduction current and the generation of a dissolved gas species which will nucleate and grow new gas bubbles within the electrolyte and further perturb the measured potential between the electrodes in a complex manner.

The kinetic overpotential at the electrode surface  $\eta = (E-E_{eq})$ , after correcting for other potential differences within the cell, is predicted to follow a Butler–Volmer-type relationship with the applied J (eq 3),

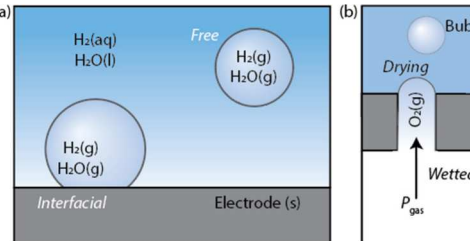
$$J = J_0 \left( e^{\alpha_a F / RT(E - E_{eq})} - e^{-\alpha_e F / RT(E - E_{eq})} \right)$$
(3

where  $\alpha_a$  and  $\alpha_c$  are the anodic and cathodic transfer coefficient, respectively, and  $J_0$  is the exchange current at the electrode surface at  $E_{eq}^{23}$  At |J| < 10 mA cm<sup>-2</sup>,  $H_2$  and  $O_2$ remain dissolved in solution, few bubbles will be observed at the electrode surface, and the polarization response is primarily controlled by heterogeneous reaction kinetics. 24,25 An appreciable amount of current will flow once the onset overpotential, here arbitrarily defined to be the overpotential required to reach |J| > 10 mA cm<sup>-2</sup>, has been exceeded; typical onset overpotentials for the HER in 1 M NaOH ranging from 30 to 300 mV on metals such as Pt, Ru, or Ni.<sup>26</sup> A transition from an exponential *J-E* relationship to a linear *J-E* relationship indicates the onset of ohmic control of the electrode potential, indicating the presence of an uncompensated potential drop between the WE and RE. Because the presence of gas bubbles affects the solution resistance (Section 5.1.1) researchers should not assume the solution resistance measured at I = 0 is consistent with the effective solution resistance during gasevolving reactions.

## 3. TERMINOLOGY, PHYSICS, AND DYNAMICS OF BUBBLES

#### 3.1. What Is a Bubble?

A bubble is defined as a finite volume of gas enclosed within one or more continuous solid or liquid phases. We further define two broad subcategories based on the organization of the gas interfaces: *interfacial bubbles*, located at the interface of two bulk phases <sup>14</sup> (e.g., the solid/liquid electrolyte interface in an alkaline water electrolysis (AWE)), and *free bubbles*, those enclosed in a single phase (Figure 3). Bubbles regularly transition from an interfacial state to a free state through the process of detachment (Figure 1). Within porous electrodes, used to facilitate multiphase transport in electrolyzers, bubbles can be understood to exist as *wetted pores* or extended three-phase contact regions (Figure 3b). The more conventional descriptions of flooding and drying come from pores that are



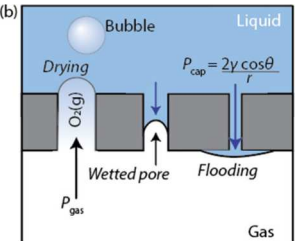


**Figure 3.** (a, b) Schematics of broad categories of  $H_2$  bubble as defined by their topology. (Left to right): Interfacial bubble, free bubble, porous electrode. (b) Organization of bubbles within porous electrodes, showing pores in a flooded, dried, and wetted state.<sup>27</sup>

saturated with liquid water/electrolyte or gas. Pores are governed by the same physical phenomena as interfacial bubbles, where the wetting state is a delicate balance of surface forces (Section 3.2.2), but at extreme current densities, the wetting state of a pore is likely to be controlled by reaction and diffusion of liquid water and vapor.

Although the energetics of all the constituent interfaces (and the corresponding effects of changing interfacial areas on the free energy of the system) should be accounted for, the unique topology of each type of bubble dictates which interfaces and physical processes are dominant when predicting their behavior. While all bubbles possess a finite gas—liquid interface, the behavior of interfacial bubbles and wetted pores is dependent on the properties of the porous solid (Section 3.2, Section 8).

## 3.2. Physical Processes Governing Gas Bubbles in Electrolyzers

The properties of bubbles and their evolution over time are governed by the physics of multiphase flows, which includes the physics of phase transfer (dissolved species into the gas phase) and of the forces on interfaces between phases. In this section, we detail the major physical drivers relevant to  $H_2$  and  $O_2$  bubbles in water electrolyzers. We do not discuss bubble physics that pertain only to vapor bubbles, which have some importance for hydrogen fuel cells and electrolysis at elevated pressures and temperatures; we instead refer the interested reader to a notable general review of bubbles.<sup>28</sup>

**3.2.1. Concentrations, Henry's Law, and (Super)**-saturation. Gas-evolving electrochemical reactions, such as the HER, quickly produce dissolved concentrations of species that are thermodynamically unstable. First, the current density, J toward HER causes a flux of  $H_2$ ,  $J_{H_2}$ , normal to the electrode surface with a rate defined by eq 4

$$\mathbf{J}_{\mathbf{H}_2} \cdot \hat{\underline{n}} = \frac{J}{\mathbf{z}\mathbf{F}} \tag{4}$$

where F is Faraday's constant, z=2 for two-electron HER, and  $\hat{n}$  is the unit normal vector. For a constant flux, the dissolved concentration of hydrogen,  $c_{\rm H_2}$ , will increase adjacent to the electrode surface, following eq 5,

$$\mathbf{J}_{\mathrm{H}_{2}} = c_{\mathrm{H}_{2}} \mathbf{v} - \mathrm{D}_{\mathrm{H}_{2}} \nabla c_{\mathrm{H}_{2}} \tag{5}$$

where  $D_{\rm H_2}$  is the diffusion coefficient and  ${\bf v}$  is the fluid velocity as a function of time and position. In the absence of gas interfaces and in a stagnant electrolyte,  $c_{\rm H_2}$  can be solved analytically in time and space but once multiple gas interfaces

are formed, the solution requires numerical methods for estimation (Section 7).

The partial pressure of hydrogen in solution  $(P_{H_2})$  is determined from the concentration through Henry's law (eq 6).

$$P_{\rm H}, k_{\rm H}, = c_{\rm H}, \tag{6}$$

where  $k_{\rm H_2}$  is the Henry's law constant, measured for a specific solution composition and temperature. The partial pressure describes the free-energy difference which drives bubble formation and growth. The ratio of the partial pressure to the ambient partial pressure,  $P_{\rm H_2}/P_0$ , is the saturation, S. When S=1 the solution would be in equilibrium with a pure hydrogen gas reservoir above the electrolyte, whereas electrolytes with  $P_{\rm H_2}$  more than  $P_0$  (S>1) are supersaturated. Supersaturation indicates that the free energy of the system will be reduced through the generation or growth of gas phases—although the kinetics of formation may preclude their formation (Section 3.3.1).

Henry's law (eq 6) provides an idealized linear relationship between concentration and partial pressure that holds well over a wide range of ambient pressures (e.g., concentrations of dissolved gas). However, at elevated pressures relevant to those observed in the nucleation of nanobubbles (> 100 atm), <sup>29,30</sup> activities are more appropriate, and small deviations from linearity are observed. In this case, experimental pressuresolubility relationships should be used. 31 For example, the experimental relationships determined by Weibe et al. 32 were used to calculate the internal pressure of a nascent nanobubble as studied by German et al.<sup>29</sup> Electrolysis frequently occurs in concentrated electrolytes where the activity of H<sub>2</sub>, O<sub>2</sub>, and other nonpolar gases will differ substantially from the concentration due to the "salting out effect". 33,34 In this case, a generalized version of Henry's Law is appropriate which accounts for the activity coefficient,  $\gamma$ , of the dissolved species which is itself a function of the electrolyte composition and temperature (eq 7).

$$P_{\rm H_2} k_{\rm H_2} = \gamma_{\rm H_2} c_{\rm H_2} \tag{7}$$

Consider that the reported  $\gamma_{\rm H_2}$  rises from  $\sim 1.3$  in 1 M KOH at 25 °C to  $\gamma_{\rm H_2} \sim 9$  in 7 M KOH at 80 °C, which is a representative environment for alkaline water electrolysis. The general implication is that effective supersaturation of gases will be greater than what is predicted from measurements in acids and bases at ionic strengths more commonly tested in the literature.

**3.2.2.** Surface Tension, Laplace Pressure, and Contact Angles. The imbalance of cohesive forces between solvent molecules at the interface of a liquid phase with a second phase (gas/liquid/solid) is defined as surface tension, a line force that acts to minimize the surface area of an interface.<sup>35</sup> Surface tension is an intrinsic property that depends on the identity of the two phases, including any dissolved species,<sup>36</sup> and is substantially modified by surfactants that adsorb at the interface. An alternate expression of surface tension (N/m) is a surface energy (J/m²), which can be interpreted as the energetic penalty for creating an interface—such as during the nucleation of gas bubbles (Section 3.3.1)

The outward pressure of the gas within a bubble counteracts the spontaneous reduction in surface energy caused by shrinking a gas—liquid interface at equilibrium. The YoungLaplace equation relates the curvature and the pressure difference across the interface,  $\Delta P$ 

$$\Delta P = \gamma \left( \frac{1}{r_x} + \frac{1}{r_y} \right) \tag{8}$$

where  $\gamma$  is the surface tension, and  $r_x$  and  $r_y$  are the radii of curvature in the axes to the surface;  $\Delta P$  is also known as the *Laplace pressure*. For a spherical/spherical cap bubble, we have  $r_x = r_y = r$  and eq 8 simplifies to eq 9.

$$\Delta P = 2\gamma/r \tag{9}$$

Noting that  $\Delta P = P_{\text{bubble}} - P_0$ , where  $P_{\text{bubble}}$  is the gas pressure inside the bubble and  $P_0$  is the ambient partial pressure of the gas, a simple rearrangement gives the internal pressure of the bubble as eq 10.

$$P_{\text{bubble}} = P_0 + \frac{2\gamma}{r} \tag{10}$$

Standard addition-of-pressure measurements have shown good agreement with eq 10 for bubbles down to 7 nm radius. This suggests that breakdown of this continuum description only occurs at molecular length scales.

For a free bubble, it is only the surface energy of the gas—liquid interface which must be balanced by the internal pressure of the gas. However, for interfacial bubbles, the free energy of the system includes additional contributions to the total surface energy, including the surface energies of the newly formed gas—solid interface, which has an area equal to the bubble's footprint on the electrode surface, and the correspondingly smaller area of the liquid—solid interface. A summary of the forces controlling interfacial bubbles is depicted in Figure 4. Balancing the three surface energies

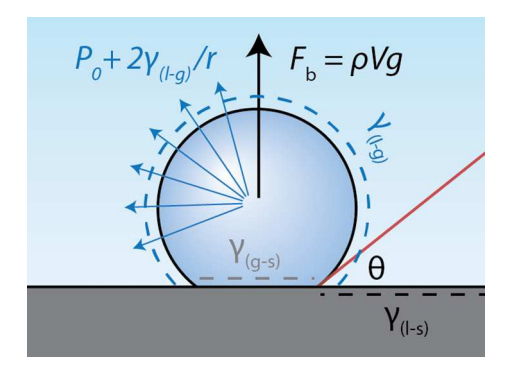


Figure 4. Interfacial forces on bubbles at electrode surfaces.

results in the Young equation, which predicts that the contact angle of the bubble with the electrode surface,  $\theta$ , (by convention, measured through the liquid phase) varies with the relative surface energies  $\gamma_{a-b}$ , where the subscripts indicate the two phases of the interface (gas, liquid, and solid)

$$\gamma_{l-s} - \gamma_{g-s} = -\gamma_{l-g}\cos(\theta) \tag{11}$$

The quantity  $\gamma_{l-s}$  -  $\gamma_{g-s}$  is often referred to as the work of adhesion,  $W_a$ ; it represents the free energy difference between the surface-attached bubble and the new solid—liquid interface.  $W_a$  for gas bubbles on *real* surfaces is not described by the idealized Young equation but instead by either the Wenzel or Cassie—Baxter equations, which account for surface roughness and heterogeneous surface chemistry, respectively. The

hysteresis observed in advancing/receding contact angle measurements is inconsistent with a true equilibrium measurement of surface forces and indicates that the effective  $W_a$  is controlled by the features present at the three-phase contact line. Indeed, Gao and McCarthy have provided experimental evidence that contact angle measurements are descriptive of interactions at the three-phase contact line alone, and the three-phase interface often remains stationary as the contents of the bubble vary.

**3.2.3. Buoyancy Forces.** The dominant force driving bubble motion at the interface is buoyancy, which generally causes bubbles to rise. Buoyancy results from a spatial variance in pressure as described by,

$$P_0 = \rho g h + P_{\text{atm}} \tag{12}$$

where  $\rho$  is the density of the solution, h is the depth of solution normal to the gravitational vector, and g is the acceleration due to gravity. As a result, all bubbles experience a gradient in pressure over the surface of the bubble and an uplift force caused by buoyancy,  $F_{\rm b}$ . For an object partially or wholly immersed in a fluid, this pressure acts as a force in the opposite direction to the gravitational vector which is equal to the weight of the displaced volume of solution,  $V_{\rm b}$ ,

$$F_{\rm b} = \rho V_{\rm b} g \tag{13}$$

Because buoyancy forces arise from gravitational interactions, measurements in micro- or zero-gravity environments can minimize or eliminate them, allowing researchers to isolate the effects of other contributions.<sup>43</sup>

3.2.4. Convective Forces. In addition to affecting the transport of dissolved gas (eq 5), any motion of the continuous fluid phase will impart a pressure on the surface of the bubble that may influence a bubbles size, shape, motion, and evolution. Movement of the solution most often results from the displacement of liquid motion by nearby growing and rising bubbles, 44,45 but forced convection due to pumping of water or electrolytes is common in water electrolyzers.<sup>4</sup> Previous works have also explored agitation via ultrasonication and also electrokinetic phenomena. 48-50 In addition to forced convection, bubbles lead to microconvection at the electrode surface, caused by motion of the gas-liquid interface and various types of convection (Section 4.1.1 and Section 5.1.1). 40,48,31-54 In particular, convection driven by gradients in surface tension—originally described by Block and Pearson but commonly referred to as Marangoni convection 55,56—has been proposed to result from gradients in temperature,<sup>54</sup> dissolved gas, 53 or electrolyte. 51 Multiple sources of convection at the three phase boundary lead to complex phenomena, including bubbles which depart and return to the electrode surface, <sup>57</sup> large bubbles which draw smaller bubbles to coalesce through radial fluid flow,<sup>58</sup> and rising gas bubbles which move toward and away a vertical electrode surface in a periodic fashion.<sup>59</sup> These and other phenomena related to convection have been considered and summarized by Lubetkin.<sup>60</sup>

**3.2.5. Electrostatic Forces and Surface Charges.** The surface of a bubble in liquid electrolytes frequently bears an electrical charge, which is a function of the solution composition. The pH is a dominant contributor to the surface charge on the gas—liquid interface, with bubbles at pH < 2 holding a positive charge buta negative charge at pH > 3. The electric field present at the solid/electrolyte interface can attract or repel charged bubble surfaces and may, in principle, affect the contact angle of the gas bubble via electrowetting;

here we note that active electrocatalysts are relatively nonpolarizable interfaces, and electrowetting has been found to exert a relatively minor influence over a wide range of applied voltages. In practice, it is difficult to predict the departure diameter of gas bubbles based on *static* force balances, and the detachment of bubbles appears to be dominated by kinetic phenomena. S1-53

#### 3.3. Evolution of Bubbles

This section considers the temporal evolution of bubbles because of the driving forces described above, which contribute to a dynamic life cycle of bubbles on gas-evolving electrodes (nucleation, growth, coalescence, detachment). At different gas bubble sizes and applied currents, one or a combination of factors may dominate the life cycle.

**3.3.1. Bubble Nucleation.** Nucleation is the first step of bubble formation and can generally be described by classical nucleation theory. The Gibbs free energy,  $\Delta G$ , required to form a bubble from a solution of dissolved  $H_2$  or  $O_2$  is the sum of the surface energy for forming a gas—liquid interface and the volume energy for forming a gas phase (Figure 5). Forming the

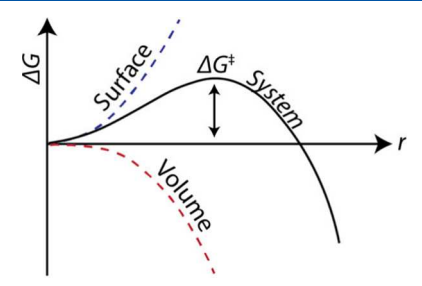


**Figure 5.** Contributions to the free energy of bubble nucleation as described by classical nucleation theory. <sup>22</sup>

gas—liquid interface within a solution is nonspontaneous, and the energy required is proportional to  $r^2$ . On the contrary, forming a gas phase from a supersaturated solution is energetically favorable, with the corresponding volume energy proportional to  $r^3$ . As a result, an energy barrier arises for bubble formation due to the opposing effects of increasing volume energy and surface energy of the bubble and corresponding interfaces as a function of the bubble radius. The maximum value of this energy barrier corresponds to the activation free energy for bubble nucleation,  $\Delta G^{\ddagger}$ , which occurs at a critical bubble radius. Substituting this activation energy into the Arrhenius equation, the nucleation rate is calculated as (eq. 14):

$$\Gamma = \Gamma_0 \exp\left(-\frac{16\pi\gamma^3 \Phi(\theta)}{3k_b T (P_{gas} - P_0)^2}\right)$$
(14)

where  $\Gamma_0$  is the pre-exponential factor,  $\gamma$  is the surface tension,  $k_{\rm B}$  is Boltzmann's constant, T is the temperature,  $P_{\rm gas}$  is the partial pressure of gas in the bubble, and  $P_0$  is the ambient pressure. See Edwards et al.<sup>30</sup> for a complete derivation.  $\Phi(\theta)$  is a geometric factor, which is a function of the contact angle  $(\theta)$  of the critical nucleus on the surface (eq 15).

$$\Phi = \frac{(2 - \cos \theta)(1 + \cos \theta)^2}{4} \tag{15}$$

Based on eq 14,  $\Gamma$  is expected to be strongly affected by  $P_{\rm gas}$ . According to Henry's law (eq 7),  $P_{\rm gas}$  is proportional to the

		•
In situ characterization	Advantages	Limitations
Microelectrode methods	• Ensemble characterization of bubble evolution or dynamic overpotentials	<ul> <li>Transport phenomena at microelectrodes may not trans</li> </ul>

(Section 4.1.1)

Nanoelectrode methods (Section 4.1.2)

Nanopore-based methods (Section 4.1.3)

Scanning electrochemical microscopy (Section 4.1.4)

Atomic Force Microscopy (Section 4.2)

Conventional optical microscopy (Section 4.3.1)

Fluorescence and luminescence microscopy (Section 4.3.2)

Interference reflection microscopy (Section 4.3.3)

Dark field microscopy (Section 4.3.4)

Surface plasmon resonance microscopy (Section 4.3.5)

Transmission electron microscopy (Section 4.4) • Compatible with optical imaging modalities for simultaneous characterization

Table 1. Summary of the In Situ Characterization Methods Used to Study Bubble Evolution Considered in This Review

- Single entity (bubble) characterization in controlled microenvironments
- Unambiguous characterization of electrochemical dynamics
- Single-entity measurements in well-controlled microenvironments
- Simpler electrode fabrication—the nanopore fabrication is decoupled from the electrochemical experiment
- Adds spatial resolution to nanopore-based methods
- Simultaneous characterization of multiple single entities
- Imaging changes in topology of an electrode surface (e.g., the growth of bubbles) with subnanometer spatial resolution
- Enables the integration of electrodes and force measurements on AFM probe, which allows for single entity force measurements (e.g., bubble adhesion forces)
- Commonly available imaging technique, compatible with high-speed (> 60 frames per second) imaging
- Nonperturbative and compatible with other in situ characterization techniques
- Simultaneous imaging of large electrode areas
- Potentially higher spatial resolution (including in super-resolution or 3D imaging via confocal measurements) than conventional optical methods.
- Chemical information can be measured via spectroscopy of fluorescent molecules (e.g., pH sensitive fluorophores 186,187) or electroluminescence
- 3D information embedded in 2D imaging by interference patterns within the image (colors or varying intensity along an interface)
- · Compatible with high-speed imaging.
- Common reflectance modality on optical microscopes that is sensitive to edges
- 3D information in 2D imaging due to nonparallel
- Spectral discrimination (e.g., imaging via Stokes-shifted light) is sensitive to local dielectric environment, such as the thickness of bubbles on a surface
- High-resolution (> 1 nm) imaging via electron optics
- Integrated electrochemical cells in TEM sample holders

- nslate to large-area planar electrodes
- Fabrication of electrodes requires sophisticated procedures
- Sensitive electrochemical measurements can require shielded experimental environment (e.g., Faraday cage)
- Electrochemical detection (e.g., ionic current) is decoupled from the electrochemistry of bubble
- · Generally, a slower process than single electrode measurements
- Motion of the electrode or probe may perturb bubble evolution processes
- Generally, a slower process than other forms of imaging
- Cantilever probe can perturb objects and interfaces at the electrode surface
- Lower, diffraction-limited (> 200 nm) spatial resolution compared to other techniques
- Relies on reflectance or transmission contrast, which can obscure features (e.g., overlapping bubbles on surfaces)
- Slower temporal resolution than conventional optical imaging (especially for confocal or superresolution imaging)
- Imaging is limited in opaque, structured electrodes

Extracting 3D information requires significant understanding/modeling of the optical properties of complex interfacial modulation in refractive indices (e.g., bubbles forming on nucleation sites).

- More complicated interpretation of imaging than other 3D-sensitive modalities
- Lower, diffraction-limited resolution than other methods.
- Relatively complex instrumentation requiring lasers and spectrometers
- Spectral discrimination may limit the accessible dynamic/temporal resolution of imaging
- Specifically tailored cell environments, including submicron layers of electrolyte
- Electrons are perturbative probes which can, for example, generate bubbles via heating or radiolytic generation of hydrogen.1

concentration of dissolved gas. Together, it suggests a supersaturation of dissolved gas is needed to reach a reasonable nucleation rate. Formally, the pressure differential in eq 14 should include the partial pressures of all gases in solution, with the resultant bubble composing of all gases in ratios equal to their partial pressures. However, gas-evolving electrodes typically produce purified gases such that the partial pressure of one gas frequently dominates that of all others (including water vapor), and the contributions of other gases may be neglected. One notable exception to this assumption might be electrolysis conducted at high temperatures and pressures, which offers substantial improvements in energy efficiency and will also lead to a more significant water vapor pressure. 66-68 Classical nucleation theory, as described above, treats phases using continuum approximations. While such methods have shown good agreement with experimental measurements of bubble nucleation, <sup>69,70</sup> the small number of species involved in forming new gas nuclei mean that these are inherently approximations of molecular processes. Molecular descriptions of bubble nucleation, such as those described by Molinero et al.,69 may give more detailed insight and are discussed further in Section 7. Lastly, it has been noted that nucleation behavior is very sensitive to the presence of defects and pre-existing gas cavities,<sup>71</sup> which are likely to play a substantial role in the gas evolution behavior of large area, rough, or porous catalyst layers used in practical water electrolyzers.

3.3.2. Growth. The growth of a bubble occurs due to net mass transfer into the bubble, which occurs when internal pressure (Section 3.2.2) exceeds the partial pressure of gas in the solution. Three key physical processes determine whether a bubble grows: (1) the flux of gas at the electrode surface (e.g.,  $J_{H_2}$ ) (2) the transport of gas in the solution phase, and (3) the internal pressure within the bubble. The bubble grows when  $P_{\rm H_2}$  exceeds the internal pressure of the bubble, resulting in molecular transfer from the solution to the gas phase. When the influx and outflux of gas at the interface are equal, a bubble neither shrinks nor grows, but exists at a fixed volume. Such behavior is observed on nanoelectrodes and the steady-state configuration determined through numerical calculations. 72 Growth of gas bubbles exerts an outward force on the solution and the electrode surface; the stress generated by gas bubbles has frequently been hypothesized to serve as a driving force for degradation of the electrocatalysts in the electrolyzer.<sup>8,73</sup> Bubble-induced delamination has been directly observed during liquid cell TEM measurements where gas was generated by the electron beam (Section 4.4),<sup>74</sup> but this behavior has yet to be quantified in a device-relevant environment.

**3.3.3. Detachment.** Detachment is the process by which an interfacial bubble separates from the surface to form a free bubble containing some or all its constituent gas, and is controlled by convective and interfacial forces which can have an attractive or repulsive influence on a bubble. An adhesive force results due to the increased energy of the liquid—gas interface compared to the solid—gas interface (Section 3.2.2, this is expected to be small for clean metals and metal oxides/hydroxides/oxyhydroxides which are hydrophilic, wetting surfaces) and fluid flow caused by local gradients in temperature and solute concentration (Section 3.2.4). Buoyancy, forced convection of the electrolyte, and coalescence between neighboring gas bubbles (Section 3.3.4), lead to forces which can drive detachment. These forces have been simulated at microelectrodes and compared to experiments

which image local fluid flow profiles at the microscale as well as gradients in refractive index (Section 4.3.6). 52,53,75 In practice, gas bubbles at pits<sup>76</sup> and solid surfaces<sup>51</sup> are observed to depart at smaller diameters than would be predicted by equilibrium force balances suggesting that other dynamic processes are important for predicting the departure diameter. Recently, Wang and co-workers reported a new regime of bubble departure from a solid wall owing to the coalescence of two bubbles.<sup>77</sup> They found that the evolution of the three-phase contact line at the bubble base lowered the bubble adhesion force, leading to a departure diameter much smaller than the conventional buoyancy limit. They further unified the relationship between bubble departure diameter and nucleation site density under both buoyancy-driven and coalescenceinduced bubble departure regimes. Gong and co-workers have also studied the effects of the two bubbles' dynamic contact angles on coalescence-induced bubble departure, 78 finding a critical contact angle of 76° from a surface energy analysis, beyond which the coalesced bubble does not depart from the

3.3.4. Coalescence. Two bubbles in proximity may combine to form a single bubble in a process known as coalescence. Coalescence is typically an energetically favorable process as it reduces the total gas-liquid and gas-solid interfacial area. The precise energetic balance depends on the resultant geometry, the surfaces involved, and the pressures in the initial bubbles and final bubble. The mechanism involves the drainage of the thin liquid film dividing the two bubbles, the joining of the bubbles in a nonequilibrium dumbbell-like shape, and a reversion to a more energetically favorable (quasispherical/sphere-cap) geometry. 79-81 Coalescence is dependent on the identity of the salts in the electrolytic solution, 82,83 and while the effect is generally understood to be related to the influence of cations on the local structure of water, some salts have a stronger effect on coalescence than others. The behavior and coalescence of evolved bubbles during and after detaching from a solid surface depend on solution properties, such as electrolyte, 82,84 liquid phase rheology, 85 the presence of organic additives such as surfactants and nonsurface-active ethylene glycol, most of which influence the electrical properties of the gas-water interface.<sup>88</sup>

#### 4. IN SITU CHARACTERIZATION TECHNIQUES

In situ characterization techniques have been developed to study the static and dynamic behavior of gas bubbles from millimeters to the nanometer scale. Electrochemical methods are well-suited for characterizing the direct impacts of gas bubbles on the local microenvironment and we distinguish in situ techniques from operando techniques based on the size and geometry of the electrode. Atomic force microscopy is suitable for characterizing very small surface-attached bubbles in liquid electrolyte. Optical microscopy is a nonperturbative technique well suited for studying the dynamic behavior of gas bubbles so long as they are larger than a few hundred nanometers in diameter. Transmission electron microscopy can directly image gas bubbles during nucleation, but beam-induced gas generation may convolute measurements. Electrodes integrated with a quartz crystal microbalance allow measurements of gas coverage via changes to the density of the electrolyte adjacent to the electrode surface. The relative advantages and disadvantages of these techniques are summarized in Table 1 at the end of Section 4.

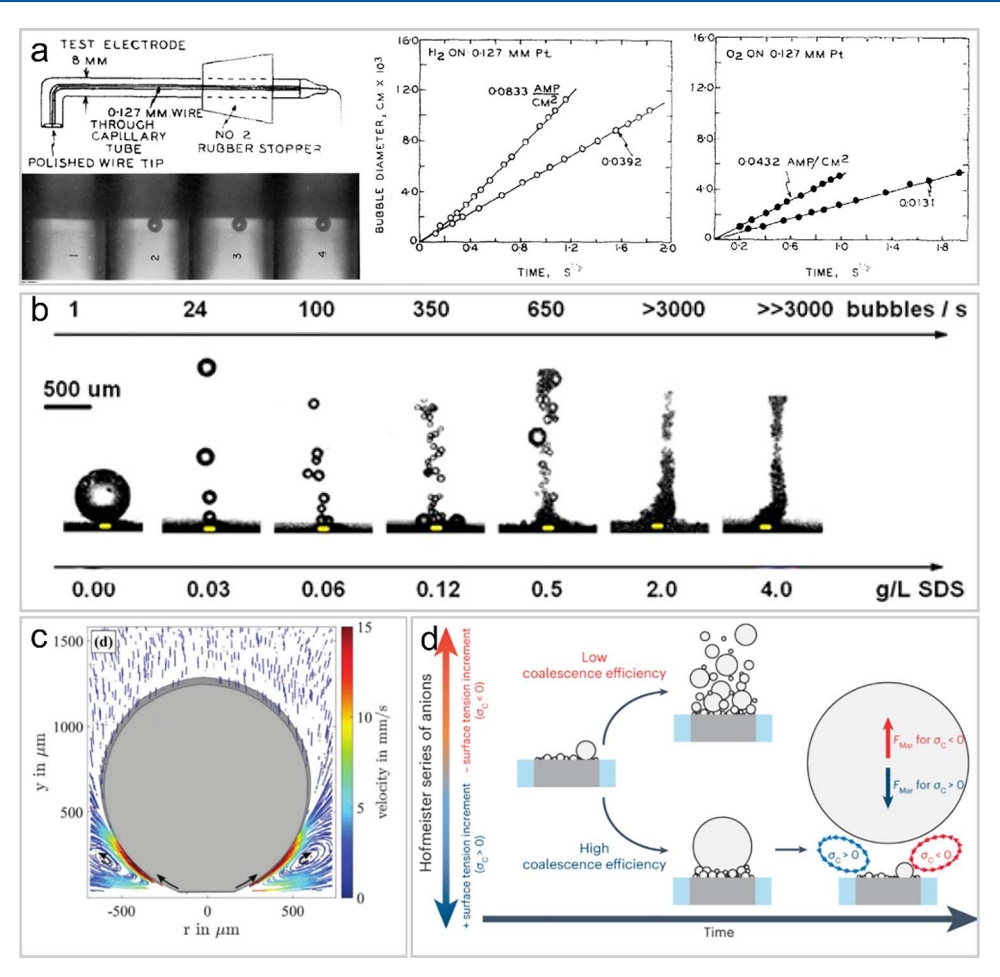


**Figure 6.** (a) Left: Schematic of a handmade 127-μm-diameter disk electrode and the photographs of an H<sub>2</sub> gas bubble growing on the disk electrode. Right: Typical growth data for H<sub>2</sub> and O<sub>2</sub> bubbles in 1.0 N H<sub>2</sub>SO<sub>4</sub>. Adapted with permission from reference. <sup>89</sup> Copyright 1964 Elsevier. (b) Photographs of the bubble release frequency from a Pt microelectrode after adding sodium dodecyl sulfate (SDS) to reduce the surface tension. Reproduced with permission from reference. <sup>62</sup> Copyright 2014 American Chemical Society. (c) Particle trajectories and corresponding velocity field around the growing bubble on a microelectrode. Reproduced with permission from reference. <sup>53</sup> Copyright 2018 Royal Society of Chemistry. (d) Illustration of the anionic effect on bubble coalescence efficiency during water reduction at a microelectrode. Reproduced with permission from reference. <sup>51</sup> Copyright 2023 Springer Nature.

#### 4.1. Electrochemistry

The physical properties of electrochemically generated gas bubbles at all stages of the life cycle (nucleation, growth, and detachment, Figure 1) can be probed with electrochemical tools that are comparable in size to individual gas bubbles, including microelectrodes, nanoelectrodes, nanopores, and scanning electrochemical cell microscope.

4.1.1. Microelectrode-Based Methods. Gas bubbles form randomly on the surface of macroscopic electrodes, making it difficult to study a single bubble and understand its behavior. Researchers have used nano- or microelectrodes to hold a single bubble in place to overcome this challenge. In the 1960s, Westerheide and Westwater investigated the growth of single hydrogen bubbles generated at a 127  $\mu$ m diameter Pt disk electrode prepared using a Pt microwire surrounded by glass capillary tubing, leaving the end of the tip exposed (Figure 6a).<sup>57</sup> An optical microscope and camera were used to record the physical behavior of bubbles, and the radial growth of a single bubble was observed to follow the square root of time  $(t^{1/2})$ , as predicted by a model based on diffusioncontrolled bubble growth in an infinite medium. The supersaturation, S, of dissolved H2 in the solution around these bubbles was determined from data fitting to be from

8=24 for J=100 to 200 mA cm<sup>-2</sup>. Interesting and complex bubble behaviors were reported at the microelectrodes, including bouncing, coalescence, and slip on the solid surface. Later, the same group studied the growth of various gas bubbles, including H2, O2, Cl2, and CO2, on platinum, nickel, copper, and iron electrodes using the same experimental setup. Similarly, they observed the bubble radius grew linearly with  $t^{1/2}$  for all electrogenerated gas bubbles on microelectrodes (Figure 6a). The computed supersaturation of dissolved gas around the gas bubbles ranges from ~1 for CO<sub>2</sub> and Cl<sub>2</sub> to up to 20 for H<sub>2</sub>. The late-stage growth rate of gas bubbles was found to be independent of the electrode for Pt, Fe, Cu, and Ni, whereas the early growth behavior did depend on the metal surface. These differences were attributed to different surface defects on the metal electrodes, which may have resulted from the electrode polishing step due to the varied metal hardness. Also, the observed contact angle of bubbles on the microelectrodes had a modest effect on the gas bubble growth.

Following the pioneering work by Westwater and colleagues, several other groups have used similar microelectrode setups to investigate factors affecting electrolytic gas bubble production. For example, Brandon and Kelsall reported similar growth

kinetics of electrogenerated H2, O2, and Cl2 gas bubbles at microelectrodes, <sup>90</sup> which follows an exponential function:  $r \propto$  $t^x$ . The time dependence of growth (classified by the exponent x) varied for different stages of bubble growth, decreasing from a value near 1 at short times (< 10 ms) through 0.5, characteristic of radial diffusion-controlled bubble growth in an infinite medium, to 0.3 at long times (> 100 ms), expected for the direct collection of the hydrogen produced at the microelectrode base into the bubble. Gabrielli et al. used microelectrodes to establish the relationship between gas evolution reaction overpotential caused by bubble-induced resistance increments and bubble size.  $^{91}$  Uhlemann et al. studied the dissolution behavior of a single  $H_2$  bubble electrochemically generated at a Pt microelectrode by monitoring the open circuit potential relaxation. 92 The rate of dissolution process is not as fast as expected from the generally applicable Epstein-Plesset model, which describes the dissolution behavior of a single spherical gas bubble in an infinite medium driven purely by diffusion. This slower rate is due to several factors, including the dissolved O2 and N2, and the supersaturation of H<sub>2</sub> between the electrode surface and bubble caused by the preceding electrode polarization.

The growth and dynamics of gas bubbles at a microelectrode is also a function of additives and the local environment around the electrode. Möbius, Coey et al. investigated the influence of additives, including sodium dodecyl sulfate (an anionic surfactant) and ethylene glycol (used to tune the solvent viscosity) on the oscillatory release of bubbles.<sup>62</sup> Coalescence of bubbles at the electrode surface was inhibited by the presence of surfactants, which led to swarms of small ( $\sim$ 50  $\mu$ m) bubbles released in an aperiodic stream (Figure 6b). Specifically, the abrupt transition from periodic to aperiodic release occurred when the surface tension fell below 70 mN m<sup>-1</sup>. The proposed explanation for the smaller detachment bubble diameter than the expected value from a force balance considering only buoyancy and surface tension was that the presence of micron-sized bubbles adhering to the surface interrupted the gas/electrode interface for the large, detaching bubble. Eckert et al. further explored detachment and growth dynamics for Pt microelectrodes surrounded by different insulating materials, glass, and epoxy. The growth of the bubble radius scaled with  $t^{0.30\pm0.02}$  law regardless of the insulating material type, despite the variations in  $\theta$  based on different interactions between the gas and the material surrounding the electrode. The coalescence of the smaller bubbles at the foot of the larger bubble was again shown to be an important growth mechanism. Eckert et al. also studied the oscillatory growth dynamics of H<sub>2</sub> bubbles. 94,95 They found that it was controlled by a competition between buoyancy and the electrostatic attraction between a negatively charged electrode and positively charged bubble surface, the magnitude of which depends on the thickness of the microbubble carpet beneath the single, larger bubble. The electric force on the single bubble reaches a maximum at a carpet thickness of about 30  $\mu$ m, which corresponds well with the carpet thickness at which the bubble detaches in their experiment.

Magnetic fields have been shown to influence the convection and stabilizing forces on microsized gas bubbles. Coey et al. studied the effect of a magnetic field that is perpendicular to the electrode surface on an electrogenerated gas bubble. They found that the bubbles on both horizontal and vertical microelectrodes grew to a greater size in a magnetic field, doubling in diameter before they broke away. Pan et al.

proposed that the changed Lorentz force distribution on a microelectrode formed a low-pressure region in the lower part of the bubble, stabilizing the bubble at the microelectrode surface under an external magnetic field. However, Baczyzmalski et al. found that the magnetohydrodynamic flow imposed only a small stabilizing force on the bubble and observed that a secondary flow enhanced the mass transfer toward the electrode and may reduce the local supersaturation of dissolved hydrogen and contributed to the bubble stabilization. The research community lacks consensus on the effects of magnetic fields on gas evolution.

There has been longstanding debate about the physics controlling mass transfer in the region near the gas/electrode interface (Section 5.1.1). Researchers have more recently turned their attention to single electrogenerated gas bubbles to resolve the fluid physics at and around the three-phaseboundary. Eckert et al. studied the Marangoni convection at a single electrogenerated hydrogen bubble on a microelectrode.<sup>53</sup> They presented evidence of Marangoni convection near growing hydrogen bubbles generated by water electrolysis, resulting from concentration gradients of dissolved gas or temperature gradients caused by ohmic heating of the electrolyte. Using time-resolved particle tracking velocimetry (PTV, Figure 6c), they found a clear correlation between the magnitude of Marangoni convection and the electric current. Later, Massing et al. evaluated the contribution of thermocapillary and electrocapillary effects to the Marangoni convection. 98 They measured the velocity and temperature of the electrolyte near the bubble interface using PTV data and luminescent lifetime imaging, noting a considerable amount of ohmic heating in the vicinity of the microelectrode which was accompanied by robust flow away from the interface. Simulations and experimental results showed a remarkable consistency in velocity and temperature fields, suggesting that the thermocapillary effect was the principal driving force of convection for microelectrodes driven at  $I \sim 10^2 \text{ A cm}^{-2}$ . Bashhatov et al. studied the dynamics of single hydrogen bubbles at Pt microelectrodes in microgravity produced during parabolic flights, thus isolating effects related to buoyancy.9 They found (1) the electrolysis current is smaller under microgravity by a factor of more than two, compared to under normal/hyper-gravity due to minimal buoyant forces; and (2) the lateral motion of bubbles plays an important role, allowing enhanced mass transfer toward the electrode and continuous hydrogen production.

The development of continuum-based models for the physics of gas bubble evolution in water has led to a better understanding of the unclear impacts of external stimuli on single-gas bubble dynamics (Section 7.3). Kristof and Pritzker conducted early studies on the effect of electrolyte composition on the dynamics of hydrogen gas bubbles at copper microelectrodes, 100 finding that the electrode response in HCl solutions was noisier and showed much larger cathodic polarization and oscillation frequency and amplitude compared to H<sub>2</sub>SO<sub>4</sub> solutions. The addition of Na<sub>2</sub>SO<sub>4</sub> and NaCl to the acid solutions promoted the nucleation and growth of numerous small bubbles at any one time and diminished the electrode potential oscillations. Most recently, Koper et al. revisited the effect of anions including SO<sub>4</sub><sup>2-</sup>, Cl<sup>-</sup>, NO<sub>3</sub><sup>-</sup>, and ClO<sub>4</sub><sup>-</sup> in acidic electrolytes on bubble dynamics.<sup>51</sup> They found that gas bubble detachment is a sensitive function of the anion identity due to differences in microbubble coalescence efficiency, which follows the Hofmeister series of anions in

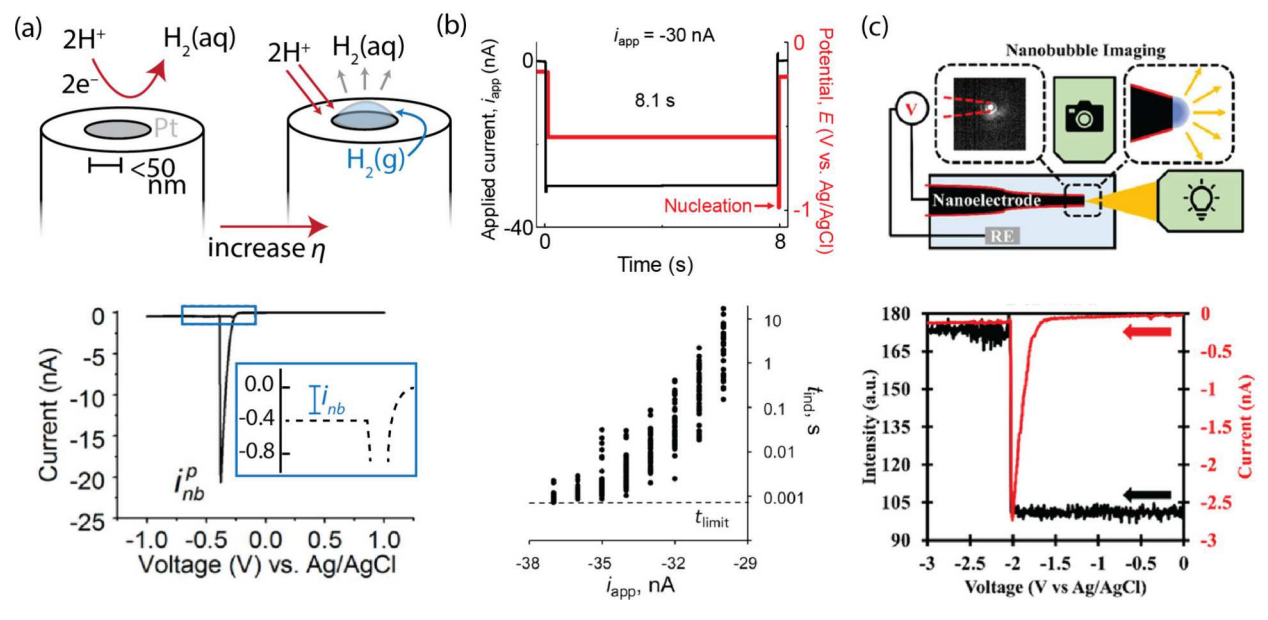


Figure 7. (a) Top: Schematic of the electrochemical formation of an individual nanobubble at a Pt nanodisk electrode with a radius < 50 nm. Bottom: The characteristic peak-shaped voltammogram of the nanoelectrode associated with bubble nucleation. Adapted from reference. (b) Top: A potential-time trace during electrochemical bubble nucleation under galvanostatic control. Bottom: The stochastics of nucleation times at various applied currents. Reproduced from reference. (c) Top: Schematic of an off-axis dark-field microscopy setup for imaging a single  $H_2$  nanobubble generated at a carbon nanoelectrode. Bottom: Correlated electrochemical (red) and optical (black) responses during a voltammetric scan to drive the formation of a single  $H_2$  nanobubble. Reproduced from reference.

the electrolyte. They concluded that a solutal Marangoni force induced by ion concentration gradients (as opposed to dissolved gas  $^{60}$ ) determines bubble detachment at practically relevant current densities ( $J < 17 \text{ A cm}^{-2}$ ). In contrast, the thermal Marangoni force becomes relevant at large overpotentials (Figure 6d). Thus, the identity of the anions in the bulk electrolyte has an influence on Marangoni convection near the gas/electrode interface.

Most recently, Bashkatov and co-workers used a dual Pt microelectrode system to study coalescence-induced detachment dynamics. Coalescence was demonstrated to enhance the performance of electrocatalytic hydrogen evolution by promoting more frequent detachment, and the conditions leading to bubble detachment followed by return to the electrode surface (previously reported at microelectrodes as well as transparent electrode surfaces) 77,58 were systematically quantified as a function of the interelectrode spacing and the applied current density.

4.1.2. Nanoelectrode-Based Methods. Although microelectrode measurements provide information about bubble dynamics at a micrometer scale, they lack the spatial resolution required to analyze the earliest stages of bubble growth, occurring just after nucleation at the nanoscale. Luo and White employed nanoelectrodes to study electrochemical H2 bubble nucleation. 102 Figure 7a schematically illustrates the experimental design and shows a characteristic voltammogram of the electrochemical nucleation of an H2 nanobubble formed by proton reduction to molecular hydrogen. Once the dissolved H<sub>2</sub> concentration at the electrode was sufficiently high, a bubble nucleated and quickly grew until the gas blocked nearly the entire surface of the nanoelectrode, causing a nearly instantaneous reduction in the absolute current. Further cathodic polarization of the electrode did not result in notable changes in the current. This stable, diminished current after bubble formation was explained by a steady-state flux of H

species at the electrode surface, where the flux of  $H_2$  electrogenerated by proton reduction at the three-phase boundary equals the outflux of  $H_2$  from the bubble into its surrounding solution. The critical concentration of dissolved  $H_2$  gas required for bubble nucleation was calculated to be  $\sim 0.23$  M from the peak current in the voltammogram, equivalent to  $S \sim 310$ .

Further investigations on gas nucleation at nanoelectrodes by the same research group characterized the effects of electrode size, anions, cations, and surfactants on bubble nucleation and stability. <sup>103,104</sup> The peak current scaled linearly with nanoelectrode radii and was independent of the anion identity (e.g., H<sub>2</sub>SO<sub>4</sub>, HCl, and H<sub>3</sub>PO<sub>4</sub>), indicating that the critical concentration of dissolved gas required for bubble nucleation is not a function of electrode size or acid type. 103 Both nonionic and ionic surfactants (including Triton X-100, TEGME, and CTAB) enable bubble nucleation at a lower level of supersaturation, but the effect of highly charged cations and anions, including Ru(NH<sub>3</sub>)<sub>6</sub><sup>3+</sup>, La<sup>3+</sup>, Fe(CN)<sub>6</sub><sup>3-</sup>, and Fe- $(CN)_6^{4-}$ , on the nucleation of  $H_2$  bubbles is significant and highly complex. They observed that the presence of the two redox ions (i.e.,  $Ru(NH_3)_6^{3+}$  and  $Fe(CN)_6^{1}^{3-}$ ) and nonredox active cation, La3+, resulted in a decrease in the H2 supersaturation required for nucleation, but Fe(CN)<sub>6</sub><sup>4-</sup> had only a minor effect on the H2 supersaturation. Similar methods were used to show that the concentrations required for nucleating gas bubbles of D2, N2, and O2, bubble nucleation from deuterium chloride reduction, hydrazine oxidation, hydrogen peroxide oxidation, respectively, are consistent at different platinum electrodes but vary as a function of the gas and properties of the cell:  $0.23 \pm 0.02$  M for  $H_2$ ,  $^{37,105}$   $0.11 \pm$ 0.01 M for  $N_2$ ,  $^{106,107}$  0.24  $\pm$  0.04 M for  $O_2$   $^{108}$ 

The chemical nature of the solid interface can influence gas evolution. Studies by the Luo group found that the bubble nucleation on Au and Pd nanodisks occurred at similar

supersaturation levels as previously observed on Pt.  $^{109,110}$  However, due to the additional electrochemical hydrogen insertion into Pd, the observed faradaic current at the bubble nucleation for Pd is higher than that for Au.  $^{110}$  Later, the Li group fabricated Ag nanoelectrodes and Ag nanoelectrodes modified by MoS $_2$  quantum dots (Ag@MoS $_2$ ) and found that the bubble nucleation condition on Ag and Ag@MoS $_2$  nanoelectrodes required a much lower supersaturation level of  $\sim\!50\text{-fold}$  than on Pt, Pd, and Au nanoelectrodes.  $^{111}$ 

Bubble nucleation from electrochemical gas evolution is a rare event and follows stochastic patterns, occurring by a heterogeneous mechanism with nuclei forming on the electrode surface. The stochastic processes of bubble nucleation can be characterized using chronopotentiometry, where a nanoelectrode is held at a constant current to control the flux of dissolved H2 at the nanoelectrode surface while monitoring the electrode potential (Figure 7b, top).<sup>37</sup> For a fixed current, the induction time prior to the single-bubble nucleation events in a predictable manner, where German et al. found the probability of observing an  $H_2(g)$  nucleation event increases rapidly across a narrow range of concentrations (0.21-0.26 M) (Figure 7b, bottom). The kinetics of phase nucleation were obtained by statistically analyzing hundreds of individual induction times at different applied currents, and from the relationship between the measured nucleation rate and the calculated supersaturation level, the activation energy for forming a critical nucleus was determined to be ~14 to 26  $k_bT$ . Whereas previously the use of pressure-addition electrochemistry was used to infer a nucleation radius for  $H_2(g)$  at Pt of ~10 nm, 112 these data simultaneously predicted a radius of curvature for critical nuclei of 4.4 to 5.3 nm, corresponding to 33 to 55 H<sub>2</sub> molecules per nuclei, and a contact angle of  $\sim 150^{\circ}.^{37}$  Most recently, Zhang et al. successfully imaged a single H2 nanobubble on a nanoelectrode using off-axis darkfield microscopy (Figure 7c). 113 Correlating optical and electrochemical responses provides new insight into surface nanobubble dissolution after removing the electrochemical H<sub>2</sub> supply, primarily that the bubble restructures during this process. The above studies using nanoelectrodes have provided a comprehensive understanding of gas bubble nucleation during the HER, which had been elusive for a long time.

Similar methods have been used to analyze the nucleation of O<sub>2</sub> bubbles in HClO<sub>4</sub> (aq). 114 A wider range of nucleation behavior was observed in comparison to H<sub>2</sub> bubble nucleation, with activation energies ranging from 6 to 30  $k_hT$ , contact angles to the electrode surface of 135-155°, and the number of O<sub>2</sub> molecules contained in the nucleus (50 to 900 molecules). Later, a voltammetric method was developed to determine the stochastic formation rate and geometry of individual H<sub>2</sub>, N<sub>2</sub>, and O<sub>2</sub> bubble nuclei.<sup>30</sup> In contrast to the chronopotentiometric method which is based on induction times, this method uses repeated potential scans to characterize the statistical distribution of the peak current prior to nucleation. Once again, the properties of single critical nuclei, including contact angle, the radius of curvature, activation energy, and Arrhenius pre-exponential factor, can be measured from the distribution of peak currents from hundreds of voltammetric cycles.

**4.1.3.** Nanopore-Based Methods. Nanopores have been used to analyze gas bubbles using similar principles to nanoelectrode measurements. Instead of blocking the electrode surface for charge transfer, nanoscale gas bubbles block an ionic path between two driving electrodes, producing an

electrical signal.  $^{115,116}$  Long et al. demonstrated the characterization of the dynamic growth of a  $\rm H_2$  nanobubble produced from a chemical reaction between  $\rm H_2O$  and  $\rm NaBH_4$  within a confined glass nanopore (Figure 8a).  $^{117}$  The nanopore was

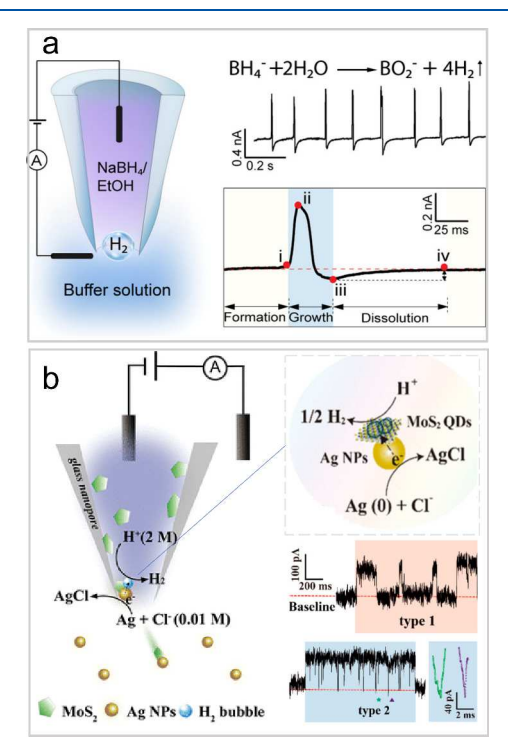


**Figure 8.** (a) Schematic showing the setup for nanopore characterization of dynamic growth of nanobubbles produced by the NaBH<sub>4</sub>—  $\rm H_2O$  reaction. Reproduced from reference. (b) Left: Schematic showing the experimental design for evaluating the HER activities of  $\rm MoS_2$  quantum dots via a bipolar electrochemistry mechanism at the orifice of the nanopore. Right: Current traces of two types of signals. A spike-like signal arises from generating  $\rm H_2$  bubbles blocking the nanopore. Reproduced from reference. (120)

backfilled with NaBH<sub>4</sub> in ethanol solution, and tetrabutylammonium hexafluorophosphate was used as an external solution. The reaction between NaBH<sub>4</sub> and H<sub>2</sub>O forms H<sub>2</sub> bubbles, resulted in the biphasic current pulse corresponding to the bubble growth and subsequential dissolution. Later, the same authors studied the temperature effects on H2 nanobubble nucleation from the NaBH<sub>4</sub>-H<sub>2</sub>O reaction using a similar nanopore-based experimental design and measured that the activation energy for nucleation was  $8.1 \times 10^{-20}$  J. This nanopore setup was further modified to evaluate the HER activities of individual MoS2 quantum dots as shown in Figure 8b. 120 MoS<sub>2</sub> quantum dots and Ag nanoparticles form a composite, which undergoes bipolar electrochemical reactions (HER at the MoS<sub>2</sub> quantum dots and Ag oxidation to AgCl at the Ag nanoparticle) at the orifice of the nanopore due to the large localized potential drop. The electrocatalytic ability of single MoS<sub>2</sub> quantum dots for HER was evaluated via the frequency of the blockages, opening a new route to monitor the electrocatalytic behavior of single catalytic particles. A similar design has also been used to monitor the HER on single Au microparticles, 121 Ag nanoparticles, 122 and catalytic decomposition of H2O2 on single MnO2 nanosphere and cubes.1

**4.1.4.** Scanning Electrochemical Microscopies. *4.1.4.1.* Scanning Electrochemical Cell Microscopy (SECCM). Scanning electrochemical cell microscopy uses a scanning probe to measure the local electrochemical behavior of a surface with nanoscale resolution. SECCM relies on an electrolyte-filled nanopipette as a scanned probe, which creates a nanosized electrochemical cell when the electrolyte nanodroplet at the tip of the pipet touches a surface (Figure 9a).

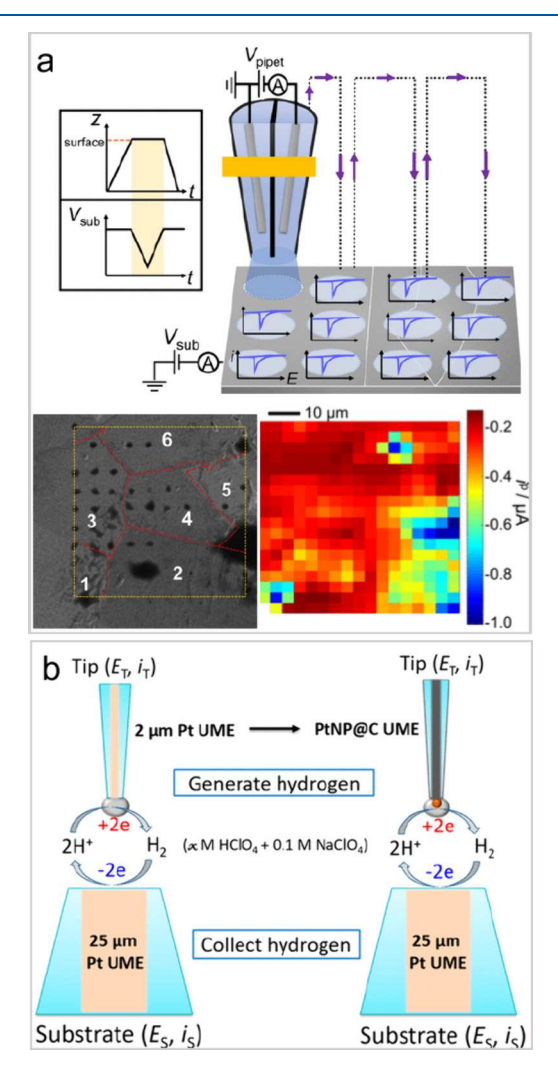


**Figure 9.** (a) Top: Schematic showing the SECCM measurement of  $H_2$  bubble nucleation on a polycrystalline Pt surface. Bottom: (left) SEM image of a polycrystalline Pt surface and (right) distribution of the peak currents for  $H_2$  bubble nucleation ( $i^p$ ) from voltammetric scans on a polycrystalline Pt surface by SECCM. Reproduced from reference. (b) Schematic of an SECM setup for electrochemical analysis of  $H_2$  bubble generation at a Pt ultramicroelectrode and a single Pt nanoparticle on a carbon ultramicroelectrode in a tip generation/substrate collection mode. Reproduced from reference. (131)

Ren et al. demonstrated using SECCM to map the  $\rm H_2$  bubble nucleation conditions on a polycrystalline Pt surface. <sup>123</sup> They observed similar characteristic peak-shaped voltammograms as the voltammogram at a nanoelectrode for  $\rm H_2$  bubble nucleation in Figure 7a. From the local voltammograms, they obtained the distribution of nucleation energetics for  $\rm H_2$  bubbles on the Pt surface but did not observe a noticeable correlation between bubble nucleation condition and crystal grains or grain boundaries (Figure 9a). At approximately the

same time, Perera et al. used a single-barrel nanopipette probe to obtain similar information about H2 bubble nucleation and growth on polycrystalline Pt and Au surfaces. 124 They observed repeated current spikes under a fixed electrode potential that drives hydrogen evolution reaction, which they assigned to individual bubble nucleation-growth-detachment life cycle described in Figure 1. Since then, the SECCM method has been applied to map the gas bubble nucleation conditions on various electrode substrates by Chen et al., including Pt, <sup>125</sup> Au and MoS<sub>2</sub>, <sup>126</sup> a nanostructured, superaerophobic MoS<sub>2</sub> electrode, <sup>127</sup> and silica nanoparticlesdecorated glassy carbon electrodes. 128 Consistent with prior results at Pt nanoelectrodes, SECCM results revealed a high S for H<sub>2</sub> prior to nucleation (218, 137, and 157 mM) with contact angles of critical nuclei ~156°, 161°, and 160° on polycrystalline Pt, Au, and ultrathin MoS<sub>2</sub>, respectively. The bubble nucleation energy barrier was significantly reduced on the nanostructured electrode surface relative to its flat counterpart, where the presence of silica nanoparticles significantly promoted the heterogeneous bubble nucleation process, 128 but no clear correlation was observed between the HER activity and the bubble nucleation energy barrier. 127 The promotion effect was observed to be nonmonotonically correlated with the silica nanoparticle size with an optimal size of ~10 nm in radius, which was explained by the theoretical free energy barrier trend calculated from classical nucleation theory.

SECCM has also been used to characterize bubble formation at individual Pt nanoparticles on a conductive but electrocatalytically inert substrate. In a system that mimics some electrolyzer cathode designs, Georgescu et al. deposited particles at a sufficiently low density such that zero or one nanoparticles were found within the SECCM pipet meniscus. The formation of H<sub>2</sub> nanobubbles at the surface of electrocatalytic Pt NPs during HER was confirmed by SECCM measurements of the change in conductivity. Finite element simulations show the nanoparticle catalyst geometry significantly affects the dissolved hydrogen gas concentration distribution for bubble nucleation. The work of Gao et al. 130 focused on hydrogen evolution in the absence of bubble formation at nanoparticle catalysts within a Nafion thin film, presenting an interesting example where SECCM was used to measure a buried interface. Such an interface contrasts the solid-liquid interface and is more closely related to the solid-PEM interface found in many water electrolysis devices.

4.1.4.2. Scanning Electrochemical Microscopy (SECM). Scanning electrochemical microscopy (SECM) has been used to study electrogenerated bubbles on surfaces. Unlike SECCM, SECM employs a mobile micro- or nanosized electrode at which a redox reaction occurs as the scanned probe tips. 132 For example, Bard's group<sup>131</sup> pioneered the use of SECM to measure and perturb  $H_2$  bubble formation in the tip generation/substrate collection experiment shown in Figure 9b. Two microelectrodes are situated facing each other; one electrode (top electrode) is swept to a potential sufficient to undergo HER and generate H2, while the other (bottom electrode) is poised at a potential to undergo hydrogen oxidation. The hydrogen oxidation current reports on the flux of H<sub>2</sub>; it also acts to deplete the local H<sub>2</sub> concentration. They also observed a peak-shaped voltammogram associated with a gaseous H2 bubble formation. When they deposited single Pt nanoparticles with sizes down to 1 nm onto the SECM tip, they found similar blocking effects on Pt nanoparticles

resulting from hydrogen bubble formation. Schuhmann et al. performed SECM measurements to study gas bubble evolution during water electrolysis, <sup>133–135</sup> but unlike Bard's experimental design, they mainly used the substrate generation-tip collection mode of SECM. They identified the most active catalytic sites from the noises recorded at the SECM tip associated with the dynamic characteristics of gas-bubble departure. Similar substrate generation-tip collection SECM experiments were conducted by Battistel et al. to study the local concentration of dissolved hydrogen produced during water electrolysis. 136 They found that at low currents, S temporarily rose to  $\sim$ 50. . In contrast, once a large current was reached, the concentration dropped, increasing the concentration of hydrogen inside gas bubbles, and became independent of the current. Recently, Kim et al. analyzed fluctuations in current recorded at an SECM tip to characterize the local rate of detachment of O<sub>2</sub> bubbles from a thin film Ir catalyst used for PEM electrolysis (Section 5.2.2).<sup>137</sup>

#### 4.2. Atomic Force Microscopy (AFM)

AFM uses tip—surface interactions to measure surface chemistry, topology, or the energetics of interfaces with extremely high resolution (down to individual atoms) related to the motion of a piezoelectric stage. A few studies have used AFM to measure *in situ* bubble characteristics in water electrolysis systems. For example, Zhang et al. observed electrochemically controlled formation and growth of hydrogen nanobubbles on bare highly oriented pyrolytic graphite surface in sulfuric acid solution via in situ tapping mode AFM (Figure 10a). <sup>138</sup> Specifically, nanobubbles were only observed

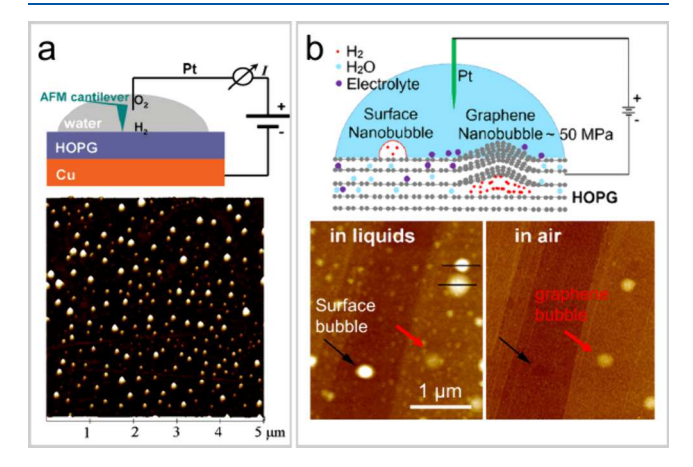


Figure 10. (a) Schematic of an experimental setup for AFM imaging of electrogenerated hydrogen and oxygen nanobubbles on a highly oriented pyrolytic graphite (HOPG) surface and an AFM image of surface nanobubble formation at  $-2.0~\rm V$  vs a Pt quasi-reference electrode. Reproduced from reference  $^{138}$  and reference.  $^{140}$  (b) Schematic showing the formation of surface nanobubbles and graphene nanobubbles during water electrolysis, supported by different images captured in electrolyte solutions (left) and in air (right). Reproduced from reference.  $^{143}$ 

beyond a voltage threshold of -1.2~V vs Pt quasi-reference electrode in 0.01 M  $\rm H_2SO_4$ . The formation, growth, and coalescence of nanobubbles and eventual release of merged microbubbles from the surface could be well controlled by tuning the applied voltage and the reaction time (Figure 10a). The observed gas nanobubbles typically have curvature radii of <2.0  $\mu m$  and heights of <100 nm, suggesting the possible instability of these nanobubbles beyond these dimensions. <sup>139</sup> A

similar experimental design was adopted by Lohse et al., 140 who studied electrogenerated H2 and O2 nanobubbles on highly oriented pyrolytic graphite surface in both pure H<sub>2</sub>O and a 10 mM NaCl(aq) electrolyte. These data indicated that (i) the nanobubble's surface area and its volume growth are highly correlated, with the authors suggesting that either the electrolytic gas is produced at the whole surface of the nanobubbles or it is generated at the electrode's surface and diffuses to the surface of the nanobubbles, and (ii) the aspect ratio of the nanobubbles and the electric current that flows between the two electrodes are correlated. Most recently, Sun et al. combined AFM measurements and electrochemical surface plasmon resonance imaging to demonstrate that surface bubbles produced by the HER grow from pancake-shaped nanobubbles, 141 followed by increasing the coverage and roughly pinned three-phase boundaries, increasing the contact angle and height. Molecular dynamics simulations further supported such pinned-rising growth mechanism. Mita et al., used a different AFM electrochemical cell design with a high scanning speed to study the hydrogen and oxygen nanobubble evolution on highly oriented pyrolytic graphite electrodes. 142 Their video data shows that the two gases exhibited different bubble nucleation and growth behaviors: the hydrogen bubbles grew with active coalescence while the oxygen bubbles were smaller and irregularly moved on the graphite surface.

AFM techniques not only allow studies of surface nanobubbles but also may detect formation of subsurface gas bubbles during water electrolysis. For example, An et al. reported the formation of nanobubbles between highly oriented pyrolytic graphite layers with electrolysis (Figure (10b), where the trapped  $H_2(g)$  between layers was reported to reach ~5 wt %. Similarly, Dollekamp et al. observed nanobubbles created between graphene and mica by reducing intercalated water to  $H_2$ . The nanobubbles have a typical radius of several hundred nm, a height of a few tens of nm, and an internal pressure of 0.5-8 MPa. AFM was also used to measure the bubble-surface interactions that prolong bubble presence at active interfaces. For example, Donose et al. developed a Pt-coated Ag<sub>2</sub>Ge needle attached to the tip of an AFM cantilever, 145 which can generate a controlled H<sub>2</sub> bubble on the tip. This allowed them to measure the forces of bubblesurface adhesion on hydrophilic surfaces as a function of microbubble diameter.

#### 4.3. Optical Microscopy

Optical microscopy is useful for large-scale imaging of bubble evolution and dynamics at electrode interfaces. The imaging resolution is diffraction limited, so systems that may be imaged by high resolution imaging such as SECCM or AFM are not accessible. However, the benefits of optical methods include the high temporal resolution offered by high-frame-rate cameras and the ability to easily couple real-time imaging to electrochemical experiments. Unlike other imaging modalities described above, optical methods typically avoid perturbing the system from conventional conditions because the light intensity required for imaging is low and physical contact with the surface is not generally necessary. Though some special cell design may be necessary to match the working distance of the objective to the electrochemical environment.

**4.3.1. Conventional Microscopy.** Conventional optical microscopy that uses reflected light for imaging has been widely used in studying micrometer-sized and larger gas bubbles. Due to the large literature, we only list some examples

here. Kou et al. used high-speed optical microscopy to measure bubble transport from the surface of 3D-printed Ni electrodes as a function of the periodic structure of the electrode. 146 They identified a critical bubble diameter (dependent on the characteristic porosity of the electrode) that trapped bubble migration through the porous structure. The regularity of the 3D printed electrode increased the observed critical diameter compared to a random, porous Ni foam electrode, which the researchers attributed to the irregularity and odd distortions required for bubble migration through the random network. The regularized 3D structure maintained significant contact with the electrolyte and avoided mass transport issues due to bubble persistence. Li et al. used a total internal reflection microscopic mode to characterize the onset potential distribution of a catalytic electrode surface. 147 At sufficiently negative potentials, the equivalent refractive index of the electrolyte on the electrode surface decreases due to H<sub>2</sub> microbubbles generation, leading to an optical signal. Using this method, they found catalytic electrodes fabricated by depositing Pt/C catalysts on porous carbon support with Nafion polymer binders show poor uniformity, reproducibility, and durability.

Kempler et al. used optical microscopy to study the nucleation and detachment of electrocatalytically generated H<sub>2</sub> bubbles on the Pt-coated Si microwire electrodes. <sup>148</sup> They showed that the structure of the surface is critical to the generation and clearance of bubbles at a surface evolving H2 at low current densities (a regime that is more important to solar fuels photoelectrochemistry) and inverted electrodes, where buoyancy will lift gas bubbles against the electrode and even drive infiltration into structured interfaces. They used highspeed optical microscopy and particle tracking analysis to measure the distribution of bubble nucleation sites as a function of the microwire structure (diameter and spacing) and electrode potential, demonstrating that bubbles are important for relieving the saturation of dissolved H<sub>2</sub>, which can induce an unwanted Nernstian shift in the reversible hydrogen evolution potential. Additionally, the microwire structure promoted bubble detachment and local convection to reduce the gas-saturated electrolyte layer near the electrode surface, even at  $J \sim 100$  mA cm<sup>-2</sup> which is a current regime more relevant to traditional alkaline water electrolysis. Pande et al. 149 used an inverted optical microscope to study the coalescence dynamic of H2 bubbles generated on a bottomfacing electrode, representative of the orientation of a small band gap photocathode in a PEC-integrated system. Direct imaging of these bubbles helps to identify clearance mechanisms and correlation electrochemical performance to the behavior of bubbles for which buoyancy is a functional issue.

Coridan et al. combined optical microscopy, electrochemistry, and synchrotron X-rays to image the high-speed dynamics of bubbles at semiconductor-electrocatalyst interfaces. The intense white-beam X-ray source was used to generate phase contrast from the edges of bubbles evolving from a microscale Pt electrocatalyst layer on Si. The phase contrast formed a visible image on a scintillation crystal, magnified by an optical objective lens onto a high-speed camera. The setup could achieve up to 100k frames per second due to the timing of the electron bunches in the synchrotron. This allowed the researchers to study the electrostatic pinning of  $\rm H_2$  bubbles evolving in 1.0 N  $\rm H_2SO_4$  on the Si surface extending beyond the Pt microelectrode. The pinned bubble

contact blocked reactant access to the Pt electrocatalyst, limiting  $H_2$  evolution as determined visually (gas bubble diameter dynamics) and by electrochemical measurements.

Mandin et al. correlated cell potentials with high-speed imaging used to measure gas diameters and coverages during alkaline water electrolysis in 0.1 M NaOH, in normal gravity and zero gravity produced with a parabolic flight path (acceleration range  $\pm 5\%$  of normal Earth gravity). Cell voltages are increased by > 1 V, even at J < 10 mA cm<sup>-2</sup>, in the absence of buoyancy-driven detachment and flow, which was correlated to larger overall bubble diameters and increased coverage of the electrode surface. <sup>151</sup>

Iwata et al. 152 used optical microscopy to image bubble departure from Ni foams used for thealkaline OER. The foams included a varied amount of polytetrafluoroethylene (PTFE) coatings to tailor the hydrophobicity. In this way, the adhesion at the gas solid interface was increased and bubbles remained on the surface for longer periods of growth, which was correlated with a measured wickability parameter. The PTFE coverage generated several distinct modes of bubble departure, from the release of small, independent bubbles to electrodes filled with a stable gas layer. The retention of a gas layer in the volume of the porous electrode limited the active surface area and increased effective overpotentials on the structured electrodes. This work showed how hydrophobicity must be chosen to appropriately mitigate transport overpotentials by promoting bubble departure without generating gas retention.

Lee et al. 153 used a model microfluidic "PTL on a chip" fabricated by soft lithography in PDMS to image the transport of bubbles as a function of pore structure. The porosity and pore distribution were modeled to resemble the relevant pore structures observed in real PTLs characterized by X-ray  $\mu$ CT. Although in this case the bubbles were generated by direct gas injection rather than by electrolysis, the microfluidic system allowed the researchers to directly monitor the migration of bubbles through the tortuous pore network by optical microscopy. They found that bubbles migrate through pores in two phases: a "pressurization" step, where the bubble gradually expands into a pore, and then a "penetration" step, where capillarity induces the rapid filling of the pore. The migration path is guided by the "least resistant throat," drawing the bubble into the next pressurization advance. This work shows that, in addition to macroscale structural parameters such as porosity, the detailed microstructure of the PTL should be considered in the design of PTL materials for mitigating mass transport limitations in electrolysis.

Microscopy can also be used to study bubble evolution due to photoelectrochemical stimulation. Bubbles forming at an interface induce light scattering, resulting in unanticipated losses caused by a reduction in absorption. Leenheer et al. 154 used a laser to illuminate a focused spot on a SrTiO<sub>3</sub> photoanode in a 1.6 M KOH aqueous solution to image the dynamics and current losses due to the local evolution of an O<sub>2</sub> bubble. They additionally considered the interplay of the scattering and lensing effects that the bubble can have on lightdriven water oxidation. In this specific case of a focused laser as a light source, they observed enhanced photocurrent in some cases where the refractive properties of the bubble redirected light to portions of the photoelectrode that were not blocked by the bubble itself. Dorfi et al. addressed similar questions by combining optical microscopy with a scanning laser that induced local photocurrent near an H2 bubble evolving from a Si photocathode. 155 Integrated external quantum yield for

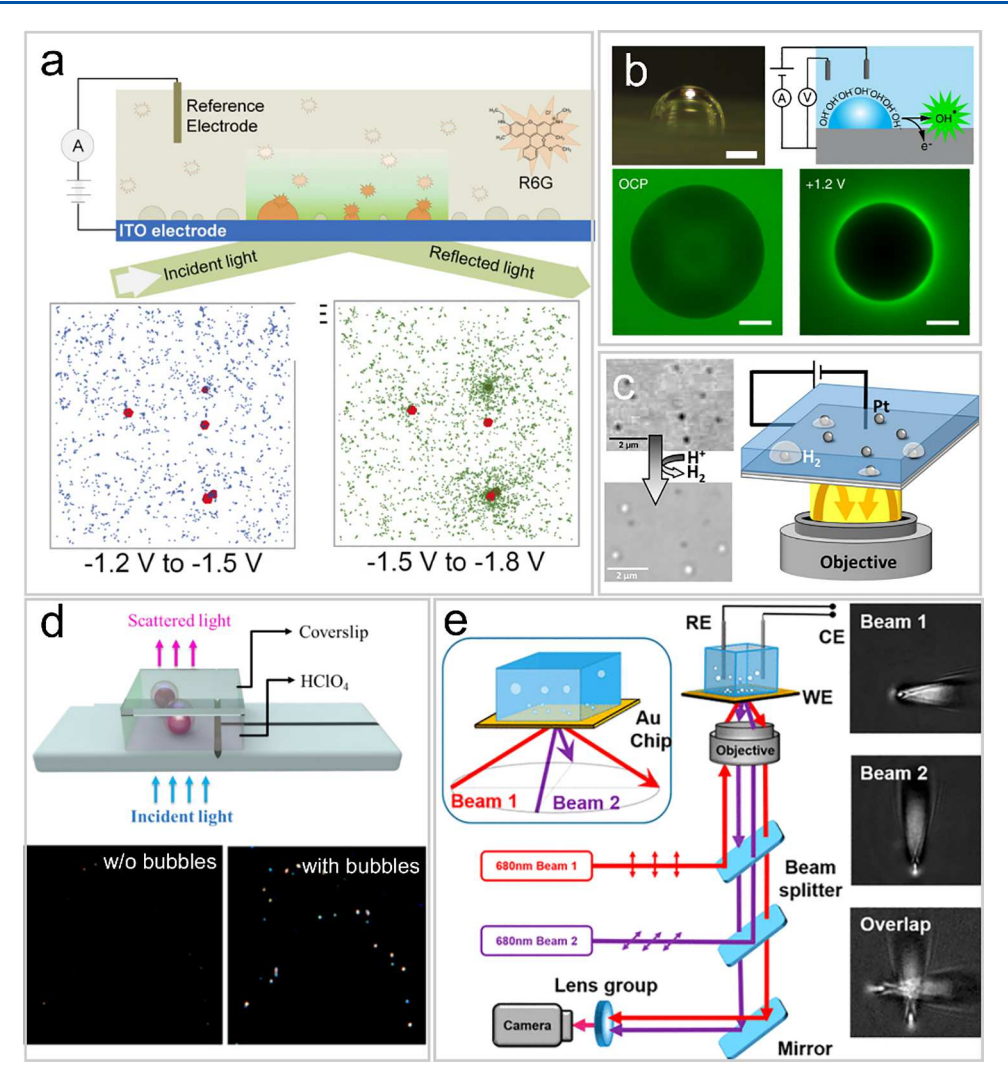


Figure 11. (a) Top: Schematic of a super-resolution single molecule fluorescence microscopy setup to image hydrogen nanobubbles during electrochemical water reduction. H<sub>2</sub> nanobubbles generated on an ITO surface are labeled by single R6G fluorescence molecules. Bottom: Scatter plots showing the accumulated spatial distribution of H<sub>2</sub> nanobubbles in two different potential windows. Each blue/green dot represents one detected nanobubble, and each red dot represents an Au nanoplate. Reproduced from reference. <sup>156</sup> (b) Top: bright-field image of an oxygen bubble on the ITO electrode and schematics of the electrochemical generation and fluorescence detection of OH<sup>•</sup> in the corona of an electrode-adherent bubble. Bottom: Epifluorescence microscopy images for detecting of OH<sup>•</sup> around a bubble in the presence of fluorescein under water oxidation conditions. Reproduced from reference <sup>164</sup> under Creative Commons Attribution International License 4.0 (c) Schematic of an interference reflection microscopy setup used to study HER at single 40 nm Pt nanoparticles deposited on an ITO surface and optical images before and after H<sub>2</sub> nanobubble formation on nanoparticles. Reproduced from reference. <sup>165</sup> (d) Schematic of a dark-field microscopy setup used for imaging H<sub>2</sub> nanobubbles from the electrocatalytic reduction of HClO<sub>4</sub> on catalytic nanoparticles and dark field images of Au@Pt core@shell nanoparticles at 0 V (without bubbles) and -1 V (with bubbles) vs Ag/AgCl. Reproduced from reference. <sup>166</sup> (e) Schematic illustration of a dual-beam configuration of surface plasmon resonance microscopy and typical images of an electrogenerated surface nanobubble under one beam and dual beam illumination. Reproduced from reference. <sup>167</sup>

current from the incident laser could be measured as a function of the bubble diameter, which showed losses of up to 22% (for a 500  $\mu$ m bubble) due to the scattering of incident illumination away from the photocathode. These studies considered the local effects of intense illumination sources in the vicinity of an evolving bubble. The conclusions can be projected to large-scale bubble persistence under areal illumination. In addition, many works using microelectrodes described above in Section 4.1.1 employed optical microscopy to provide complementary information to the electrochemical signal during electrochemical bubble evolution. We will not reiterate their findings in this section.

**4.3.2. Fluorescence and Luminescence Microscopy.** Optical microscopy can also use complex modalities, including

fluorescence, chemiluminescence, or confocal modes, to achieve higher resolution, image 3D structures, or measure *in situ* changes of the chemical environment. For example, the Zhang group demonstrated the use of super-resolution fluorescence microscopy to image the dynamic nucleation and growth of hydrogen nanobubbles at the electrode/solution interface during electrochemical water splitting. This method is based upon a single-molecule labeling process illustrated in Figure 11a, where fluorescence dye molecules (e.g., Rhodamine 6G) adsorb onto the nanobubble's gas/solution interface and become trapped, enabling detection by total-internal reflection fluorescence microscopic imaging. Their results show that nanobubbles may form on an indium tin oxide (ITO) electrode at very early stages during water

electrolysis, i.e., > 500 mV, before reaching the thermodynamic reduction potential of water. Moreover, they reported that H<sub>2</sub> nanobubbles on a gold-nanoplate-modified ITO electrode formed initially on the inert ITO surface rather than at the more catalytic gold nanoparticles (Figure 11a), possibly due to hydrogen spillover from ultrathin gold nanoplates. The same authors later coated ITO with an Au/Pd alloy and imaged the H<sub>2</sub> and O<sub>2</sub> nanobubbles formed by water electrolysis in NaOH using single-molecule fluorescence microscopy. For these electrodes, O2 nanobubbles were reported to be generated early in the oxygen evolution on the Au/Pd-ITO electrode, whereas the generation of H<sub>2</sub> nanobubbles was delayed due to hydrogen storage in the Au/Pd alloy. Later, the same group modified the initial experimental design by replacing the rhodamine dye with a polarity-sensitive, solvatochromic fluorophore Nile red. They found the Nile-red-labeled events appear to be longer in duration than those labeled with rhodamine fluorophores, suggesting that the hydrogen nanobubble/solution interface is hydrophobic in nature. They also tested the effect of surfactants on electrochemically generated surface nanobubbles. 159,160 They found that (i) the presence of anionic and nonionic surfactants increases the rate of nanobubble nucleation at all potentials in a voltage scan, (ii) the surfactants also accumulate at the gas nanobubble-liquid interface affecting the fluorophore intensity and residence lifetime, and (iii) the fluorescence readout duration depends on the electrostatic interaction between fluorophores and surfactants on the bubble surface. However, how the bubble properties, such as size, shape, etc., impact dye adsorption is not fully understood. <sup>161</sup> Apart from Zhang's work, Li and workers also conducted similar total internal reflection fluorescence microscopic experiments. Still, they focused on the potential-dependent vertical motion of electrocatalytic nanoparticles induced by electrogenerated gas nanobubbles. 162 As a gas bubble grows, the fluorescent label on the gas bubble and nanoparticles are lifted outside the evanescent field and thus cannot be detected. The hopping feature of a single particle is closely correlated with the intrinsic activities of electrocatalysts. It can be used as an indicator to evaluate the gas evolution performance of electrocatalysts at the single nanoparticle level.

In addition to fluorescence microscopy, luminescence microscopic methods have also been developed to study electrogenerated gas bubbles. For example, Lin et al. developed an electrochemiluminescence microscopic method to identify hydrogen evolution activities of single nanoparticle catalysts. 163 Specifically, they used the ON and OFF signals of electrochemiluminescence stimulated by the generation, growth, and collapse of H<sub>2</sub> nanobubbles from HER to evaluate the catalytic activities of single hollow carbon nitride nanospheres. They observed power-law distributed durations of ON and OFF states, suggesting multiple catalytic sites with stochastic activities on a single catalytic nanospheres. The power-law coefficients of electrochemiluminescence blinking increase with improved hydrogen evolution activities from modified nanospheres with other active cocatalysts, including AuPd, NiS, and Pt. Ciampi et al. designed a microscopic experiment to study the electrochemical generation and fluorescence detection of OH in the corona of an electrode-adherent bubble under anode operating condition in water (Figure 11b).<sup>164</sup> They found that surface bubbles are not inert but highly reactive redox sites. In the proximity of the electrode surface, unbalanced hydroxide anions around the corona of surface gas bubbles are oxidized to highly reactive hydroxyl radicals at potentials as low as +1.2 V vs SHE.

**4.3.3.** Interference Reflection Microscopy. Interference reflection microscopy, or interference contrast microscopy, relies on reflections from an incident beam of light as it passes through materials of different refractive indices. 168 It has been used to study a wide range of cellular behaviors, including cell adhesion, motility, exocytosis, and endocytosis, with the measured response depending on how reflected beams constructively or destructively interfere. Kanoufi et al. probed an ensemble of individual <30 nm Pt nanoparticles and the surface nanobubbles generated by these nanoparticles under electrochemical activation using an interference reflection microscopy setup. 165 Pt nanoparticles alone produce a dark contrast feature, but under electrolytic conditions, the contrast of optical spots changes and becomes bright due to gas bubble formation (Figure 11c). They evaluated the size and shape of these electrogenerated nanobubbles by modeling the optical response in the interference reflection microscopy configuration. They observed the rapid electrical disconnection of a substantial amount of Pt nanoparticles provoked by the nanobubble growth and the presence of hydrogen crosstalk from less active nanoparticles to the most active ones. In a follow-up work, the same authors studied the distribution of electrochemically active regions of ITO electrodes for HER and reductive decomposition reactions using the same microscopy setup. 169

**4.3.4. Dark Field Microscopy.** Dark-field microscopic imaging relies on the scattered light out of a hollow cone of light that is focused on the sample. This approach has been widely used to study single nanoparticles; <sup>170</sup> more recently, it was adopted to image gas nanobubbles. <sup>166,171,172</sup> Among these studies, Lin et al. investigated the single-nanoparticle electrocatalytic hydrogen generation process and activity (Figure 11d). They found that small nanoparticles, with a characteristic length <30 nm, that were invisible under a dark field microscope became visible due to the strong light reflection of the nanobubbles covering the nanoparticles. The electrocatalytic reaction process could be monitored in realtime by observing the scattering intensity change. In contrast to the above work, Zhang et al. subjected a single nanobubble formed on a nanoelectrode to dark-field imaging using an offaxis dark-field configuration. 113 They found a correlation between the electrochemical response of a nanoelectrode and the optical signal from a dark field microscope.

4.3.5. Surface Plasmon Resonance (SPR) Microscopy. SPR microscopy leverages the local change in the refractive index of a plasmonic metallic surface (e.g., Au) to shift the resonance angle and generate high-contrast images. SPR microscopy can achieve a subnanometer thickness sensitivity, with micrometer-scale lateral resolution. Tao et al. demonstrated the use of SPR to image a single nanoparticle electrocatalytic current from a hydrogen evolution reaction for the first time. 173 The typical SPR images of a single platinum nanoparticle have long tails pointing toward the surface plasmonic wave due to the scattering of the plasmonic waves by nanoparticles (Figure 11e). During the HER, a thin layer (several tens to a hundred nanometers) of hydrogen-rich medium around the platinum nanoparticle is generated, altering the SPR image. The Wang group applied the same imaging principle to study the nucleation of single nanosized vapor bubbles, 174 dynamic stick-slip and migration of single sub-100 nm surface nanobubbles, 175 and photocatalytically

generated hydrogen gas bubbles at single CdS nanoparticles. 176 They further measured the refractive index of single surface nanobubbles prepared by these different methods, including solvent exchange process, local heating of water, and photocatalytic splitting of water. 1777 Most recently, the Wang group developed a stochastic optical reconstruction microscopy approach for super-resolved imaging of bubble nucleation sites in hydrogen evolution reactions. 167 In this approach, they obtained the location information on each nanobubble via superlocalization fitting. By applying thousands of ON/OFF electrode potential cycles to drive the repeated formation of hydrogen bubbles, they reconstructed a map of nucleation sites with a spatial resolution beyond the optical diffraction limit. They further improved the localization accuracy using a dualbeam configuration and achieved a spatial resolution of 30 nm (Figure 11e). In parallel, Sun et al. combined SPR microscopy and AFM to visualize the formation and growth of interfacial nanobubbles during the initial stage of the hydrogen evolution reaction.141

4.3.6. Particle Tracking Measurements. The local fluid flows induced by gas bubble growth, Marangoni convection, and detachment can be mapped using either Particle Tracking Velocimetry (PTV)—which follows the motion of individual particles over time and is more useful for studying unsteady flows—or Particle Image Velocimetry (PIV)—which captures an instantaneous, average flow field. Time-resolved PTV measurements coupled with microscopic high speed imaging have been critical in understanding Marangoni convection at microelectrodes. 53,98 Hossain used coupled shadowgraphy and microscale PTV measurements to prepare a detailed force balance on the oscillatory motion of gas bubbles at microelectrodes and Bashkatov used the same techniques in tandem with schlieren imaging (which is sensitive to changes in refractive index caused by gradients in temperature, pressure, or solute concentration) to explain the observation of motion reversal for gas bubbles undergoing detachment. 52,75

#### 4.4. Transmission Electron Microscopy (TEM)

The recent development of liquid-cell electron microscopy makes direct observation of electrolytic  $H_2$  bubble generation possible. Dillon et al. fabricated an  $in\ situ$  environmental cell from a  $SiN_x$  TEM grid by patterning 25 nm Au electrodes on commercial Si-supported amorphous  $SiN_x$  windows using photolithography (Figure 12a, b). They observed that electrogenerated hydrogen gas dissolves into the solution initially and then nucleates near the Au electrode but not directly on its surface. The bubble eventually wets the surface, as shown in Figure 12c, and the surface roughness significantly impacts its growth kinetics because surface roughness affects the local dihedral angle and capillarity. One complexity in the TEM study of electrogenerated bubbles is the electron beam effect, which can trigger radiolytic heterogeneous nucleation of hydrogen bubbles during TEM imaging at accelerating voltages of a few hundred keV.

#### 4.5. Electrochemical Quartz Crystal Microbalance (EQCM)

Quartz crystal microbalances (QCMs) use the reverse piezoelectric effect to detect mass changes at an interface with high sensitivity by measuring changes in the resonant frequency of the crystal. QCMs are commonly found in thin film deposition systems to measure the deposition extent. However, the crystal can include an integrated working electrode as an *in situ*, electrochemical QCM. The addition of a working electrode allows researchers to monitor mass

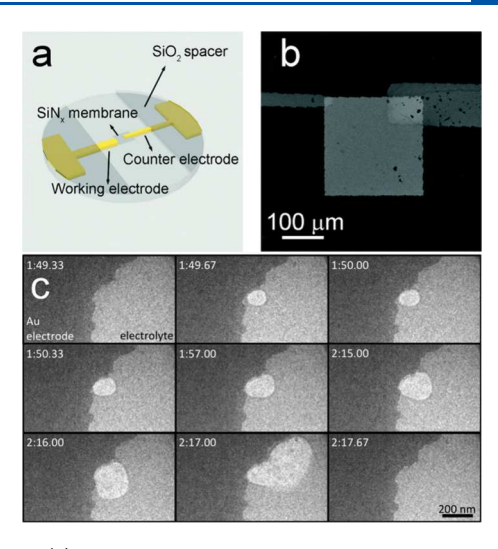


**Figure 12.** (a) Schematic of a  $SiN_x$  grid for *in situ* environmental TEM cell. (b) SEM image of the 50 nm  $SiN_x$  window. (c) Time-lapse TEM images showing nucleation and growth of electrolytic gas at the gold electrode. Reproduced with permission from reference. <sup>178</sup> Copyright 2014 Royal Society of Chemistry.

changes caused by transformations in the active material (e.g., oxidation/reduction or dissolution/deposition). Hillman and collaborators pioneered the use of an electrochemical QCM (EQCM) to monitor electrochemical gas evolution. 181-183 The EQCM detection of bubbles relies on the contrast in resonant QCM frequency,  $\omega$ , due to the density differences in gases and liquids occurring within a modulation layer of the quartz crystal. The thickness of the modulation layer is on the order of a few hundred nanometers and is proportional to  $(\nu/$  $(\omega)^{1/2}$  where  $\nu$  is the kinematic viscosity of the electrolyte. Carr et al. initially showed that the cyclic voltammetry and EQCM measurements could be measured simultaneously on a H<sub>2</sub>evolving Au electrode in an aqueous 0.1 M HClO<sub>4</sub> electrolyte, with bubble formation attributed to positive shifts in the resonant frequency, corresponding to a "mass reduction" at the electrode interface. 181 The EQCM signal is expected to depend on the contact area of the bubble, which could be used to infer details about the bubble-interface structure. Later, Li et al. used similar methods to study the evolution of H<sub>2</sub> and Cl<sub>2</sub> bubbles on a Pt cathode in aqueous chloride solutions (0.9 M NaCl + 0.1 M HCl). Systematic step electrolysis experiments allowed for the observation of both interfacial chemical changes (Pt oxidation/reduction, Pt dissolution, Cl adsorption) and bubble evolution. 182 One significant effect that could be measured for bubble evolution in both anodic and cathodic operation was the onset current density for the formation of bubbles on the surface (roughly 20 mA cm<sup>-2</sup>). The authors also noted that EQCM could potentially be useful for measuring bubble stability or dissolution at the interface, although competing film-formation and corrosion processes obscure direct interpretation. Finally, the same authors observed single bubble evolution and detachment events during potentiostatic Cl<sub>2</sub> evolution in the same aqueous acidic chloride solutions. 183

More recent EQCM studies have used the density contrast to analyze the relationship of surface chemistry and bubble formation. The goal of this work is to be able to assess the formation of nonelectrolytic bubbles that may affect the interpretation of electrolytic bubble evolution in EQCM measurements. Tsionsky et al., used EQCM to assess whether

nanoscale gas layers form at gold electrode surfaces with varying degrees of chemical hydrophobicity. <sup>184</sup> By roughening the surface of the electrode, they could assess the minimum bubble size that could be detected by the EQCM technique. They found no evidence for nonelectrolytic bubbles larger than a few nanometers (the expected limit of detection) present at the electrode interface. However, studies by Zhang <sup>185</sup> showed that nanobubbles could be formed at thiol-coated Au electrodes during solvent exchange and characterized the dynamics of these bubbles at low surface coverage using QCM.

## 5. ELECTRODE- AND DEVICE-LEVEL IMPACTS OF GAS BUBBLES

#### 5.1. Electrode-Level Impacts of Gas Bubbles

The influence of gas bubbles on electrolysis and specifically water electrolysis has been discussed since the earliest days of electrochemistry. The working potential window of aqueous electrolytes is often defined by decomposition of water into H<sub>2</sub> and O<sub>2</sub> gases and the intentional or unintentional generation of gas bubbles has many deleterious effects on the performance of cell components. In the late 19th century, Peddie reported early observations of the increase in electrode resistance caused by gaseous films at platinum electrodes. 188 At the turn of the 20th century, Caspari was the first to report on the influence of gas bubbles on the effective overpotential,  $\eta$ , for gas-evolving half-reactions, while noting that the HER is virtually reversible at Pt electrodes in acid. 20 Glasstone identified dissolved H<sub>2</sub> as a precursor to bubbles of  $H_2$  and noted that the minimum  $\eta$  is connected to the formation of these gaseous products, although he was careful to emphasize that bubble formation is not the *only* process which determines  $\eta$ . Eyring, Glasstone, and Laidler further discussed the influence of gas evolution on  $\eta$  in a paper presented at the 1939 meeting of the Electrochemical Society, where it was noted that for most metals the rate-determining step is related to ion transfer whereas for metals with fast kinetics, such as platinized Pt, the formation of H<sub>2</sub> becomes rate limiting. 190

**5.1.1. Ohmic Contributions.** Tobias made early contributions to the understanding of gas-covered electrode surfaces by studying the effective conductivity,  $K_e$ , of suspensions of insulating silica particles within an electrolyte having a bulk conductivity  $K_e$ , as a proxy for electrolytes containing suspended gas bubbles, and found that  $K_e$  was better described by Bruggerman's approximations for effective mediums (eq 16) than the Maxwell relationship which neglects interactions between neighboring spheres (eq 17).

$$\frac{K_e}{K_c} = (1 - f)^{3/2} \tag{16}$$

$$\frac{K_e}{K_c} = \frac{1 - f}{1 + \frac{f}{2}} \tag{17}$$

where f is the volume fraction of the insulating particles. Both relationships converge to similar predictions in the limit of small volume fractions ( $f \ll 1$ ) where Maxwell's assumptions are satisfied. Sides and Tobias later developed analytical solutions for the current distribution around insulating gas bubbles at an electrode surface; <sup>192</sup> the same authors then supported these models with direct observation of the electrode surface using semitransparent electrodes, <sup>58</sup> and

model systems such as electrodes covered with arrays of insulating glass spheres.  $^{193}$ 

Early experimental studies on the effects of gas bubbles on electrolyzers producing hydrogen were developed by Hine et al.,45 who used Luggin capillaries composed of PTFE to measure the potential difference between an electrode and diaphragm in a representative electrolyzer channels as a function of the flow rate and operational current. These authors introduced models which accounted for the distribution of gas bubbles within the flow channel to explain discrepancies in the measured interelectrode resistance and void fraction, although later measurements using two separate Luggin capillaries mounted within the electrode plates showed good agreement with the Bruggemann equation (eq 16). 194 Janssen and Barendrecht measured the increase in ohmic resistance for gas-evolving Pt, Ni, Au, and glassy carbon electrodes in 7 M KOH and modeled the gas layer as a fixed layer of interfacial bubbles and a diffuse layer of free bubbles, where the effective conductivity was again predicted using (eq 16). 195 Vogt further refined the models proposed by Hine for the case of nonperforated electrodes while considering both the natural convection caused by interactions between rising bubbles as well as forced convection from pumping, calculating that a thin, densely packed "bubble curtain" can have an outsized influence on the measured resistance.44

**5.1.2.** Hyperpolarization and Concentration Overpotentials. Bubbles contribute a negligible amount to the ohmic losses in the cell ( $\sim$ 1%) when the gas coverage is < 30% of the electrode surface and the thickness of the gas layer is < 10% of the interelectrode gap. The theoretical maximum increase in resistance for a close packed layer of spheres has been predicted to be  $\sim$ 8%. Sides and Leistra, contemporaneously with Dukovic and Tobias, advanced a model which deconstructed the total bubble-induced overpotential into contributions from not only increases in ohmic resistance but also hyperpolarization,  $\eta_h$ , caused by coverage (eq 18)

$$\eta_h = b \log \left( \frac{A}{A_h} \right) \tag{18}$$

and concentration overpotentials,  $\eta_c$  (eq 19).

$$\eta_c = -\frac{RT}{zF} \ln S \tag{19}$$

Where  $A_h$  and A are the effective catalytically active area with and without gas bubbles, respectively, and b is the Tafel slope, a measure of the kinetic polarization response. Tafel slopes should ideally be measured in the absence of gas bubbles, but this is difficult to achieve in practice as Tafel slopes should ideally be measured at absolute potential differences >120 mV from  $E_{eq}$  where the expected J for an effective HER catalysts will lead to substantial gas generation. The separation of the total overpotentials into individual contributions from increased resistance, dissolved gas, and catalyst coverage was further developed by Gabrielli who studied the ability of potential transients at upward-facing microelectrodes covered by gas bubbles or insulating spherical particles, showing that the induced overpotential of individual bubbles smaller than the electrode area is proportional to the square of their radius (Section 4.1.1).91 This general approach to enumerating specific contributions to bubble-related overpotentials continues to be favored for understanding the behavior of gas-evolving electrodes. 10,148,152

**5.1.3. Bubble-Induced Microconvection.** Both the growth and detachment of gas bubbles from an electrode surface drive fluid flow in the region adjacent to the gas—liquid interface. The consequence of this bubble induced convection is increased mass transport to the electrode surface (despite the physical obstruction of the surface by gas interfaces) and was first directly quantified by Ibl and Venczel using the partial current passed toward a dilute Fe<sup>3+</sup> or Ce<sup>4+</sup> redox couple reduced at a hydrogen-evolving electrode (Figure 13a,b). <sup>197</sup>

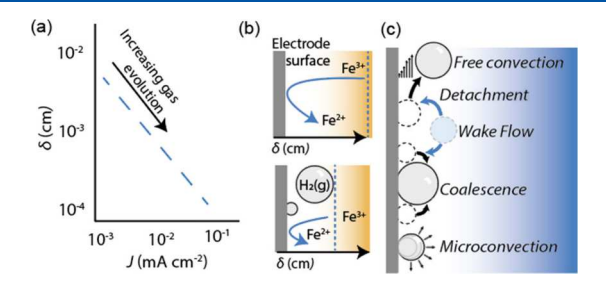


**Figure 13.** (a) The diffusion boundary layer thickness,  $\delta$ , scales with the rate of gas evolution for many different gas evolving reactions, electrolytes, and electrode surfaces. (b) Measurements of effective  $\delta$  using limiting current density for tracer redox couples (e.g., Fe<sup>2+/3+</sup>)<sup>28</sup> (c) Models of bubble driven convection.<sup>33</sup>

When the concentration of the redox couple is forced to zero at the electrode surface, the partial reduction current is limited only by transport to the electrode surface. The effective diffusion layer thickness,  $\delta$ , is a constructed value that assumes one-dimensional diffusion averaged over the electrode surface, with the partial current toward the redox couple,  $j_O$ , expressed as

$$j_{\rm O} = FD_{\rm O}c_{\rm O}^*/\delta \tag{20}$$

where  $D_O$  is the diffusion coefficient of the redox couple and  $c_O^*$ is the fixed concentration of the redox couple, assume to occur at a distance  $\delta$  from the electrode surface. Based on this data, Ibl developed a penetration model to explain increased mass transport, where intermittent replacement of departing gas bubbles with fresh electrolyte drives convection with standard diffusive transport in between departures. 24,198 This experimental method was adapted for oxygen- and chlorine-evolving electrodes by Janssen and Hoogland who found that mass transport driven by microconvection depended sensitively on the properties of the electrode surface and chemical composition of the gas. 59,199 Although the presence of attached gas bubbles across the electrode surface, many of which are greater in diameter than the measured diffusion length, invalidates the premise of a uniform boundary layer, the method is a convenient way to quantify the average masstransfer behavior across a gas-evolving electrode.

Sides and Tobias reported that small gas bubbles on transparent planar electrodes moved radially to coalesce with larger gas bubbles which were then released from the electrode surface; this motion serves as a source of convection within the otherwise stagnant fluid boundary layer (Figure 13c). Notably radial coalescence cannot be described by a one-dimensional model for transport through a gas-evolving electrode and serves to counteract the lack of transport to regions temporarily obstructed by an interfacial bubble. The mechanism for lateral movement of gas bubbles leading to coalescence was first attributed to a thermocapillary effect by

Guelcher and Sides,  $^{54}$  where a temperature gradient is sustained by the increased joule heating in the electrolyte region between gas bubbles, leading to fluid flow away from the electrode surface which causes bubbles to feel mutually attractive forces driving coalescence. Another explanation, advanced by Eckert's group, involves Marangoni convection, caused by supersaturation of dissolved gas in the regions far from gas—liquid interfaces, leading to a gradient in the local surface tension of the electrolyte (Section 4.1.1).  $^{52,53}$  Although the influence of mass transport on reaction kinetics are marginal in concentrated alkaline electrolytes at high temperatures (> 80  $^{\circ}$ C), the concentration of dissolved gas in the region near the diaphragm or separator is important for accurately predicting  $\rm H_2$  crossover behavior which is primarily driven by Fickian diffusion.  $^{200-203}$ 

The fact that smaller bubbles lead to a greater mass transport coefficients can be explained by the more frequent detachment-driven convection resulting from small bubbles, which is consistent with early models for transport at gas-evolving electrodes developed Ibl.<sup>204</sup> Vogt has studied the complex relationship between the applied current density and bubble-driven mass transport in more detail, considering multiple modes of diffusion and convection which act in synchrony.<sup>205,206</sup> These models predict an increase in mass transfer rates with increasing gas coverages when less than 20% of the surface is obscured, but a decrease in mass transfer at very large current densities and gas coverages. The scaling relationship between diffusion-limited currents for a dilute tracer molecule can be used to identify the dominant modes mass transport.<sup>24,148</sup>

#### 5.2. Device-level impacts of gas bubbles

The device-level impacts of bubbles on electrochemical reactors are dependent on the geometry of the electrodes and electrolyte. Two approaches for low-temperature electrolysis account for the majority of installed water-electrolysis capacity to-date and are therefore emphasized within this review: (1) electrolysis in aqueous, alkaline electrolytes and (2) electrolysis across a solid proton-conducting membrane fed with pure water as a reactant to either or both electrodes.<sup>207</sup> Aqueous alkaline water electrolysis (AWE) is the most mature form of electrolysis, dating back to the beginning of the 20th century and is distinguished by the typical use of nickel and stainless-steel electrodes and inexpensive microporous separators, which are today typically operated in concentrated solutions of KOH at ~80 °C. 200 Both O2 and H2 gas bubbles are formed and lead to "gas holdup" within the electrolyzer, which has a significant impact on the overall performance of the cell. On the other hand, proton exchange membranes water electrolysis (PEMWE) most often occurs in cells with deionized water being fed only to the anodic side of the cell, such that O<sub>2</sub> bubbles are the primary concern for gas evolution and the only H2 bubbles exist as dewetted pores within the porous cathode layer.<sup>201</sup>

**5.2.1.** Gas Evolution in Liquid Alkaline Water Electrolysis. In AWE, gas bubbles generated between the electrode and porous diaphragm can lead to substantial increases in measured cell voltage at typical operating currents and also limit the maximum operating current density.  $^{209}$  The departure diameter of  $H_2$  and  $O_2$  bubbles produced in concentrated KOH is strongly dependent on applied current and ionic strength, but is typically not consistent with predictions based on a balance of buoyancy and surface forces

(predicted, 500–1000  $\mu$ m). <sup>210,211</sup> Bubbles between 100–200  $\mu$ m in diameter are observed with photography whereas bubbles < 10  $\mu$ m have been observed at transparent electrode surfaces using optical microscopy. <sup>58,212,213</sup> As these bubbles grow and detach from an electrode surface held at a constant current, a characteristic sawtooth shaped potential transient is produced (Figure 14), where periodic drops in potential are

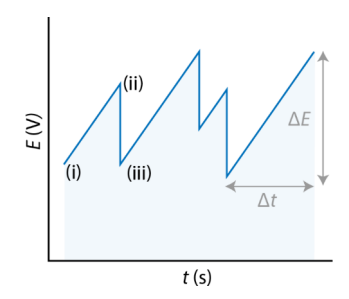


Figure 14. Schematic representation of a potential transient for a gasevolving electrode (i) growth of gas bubbles on the surface leads to a steady increase in potential, followed by (ii) sudden release of a large gas bubble leading to a nearly instantaneous drop in the measured potential (iii).

correlated with the release of large gas bubbles. Both the period  $(\Delta t)$  and magnitude  $(\Delta E)$  of the sawtooth pattern in the potential transient are related to the life cycle of gas bubbles on the electrode surface and have been discussed by many researchers.

In a device environment, gases primarily increase the working potential of the cell by increasing ohmic losses and reducing the effective catalyst surface area. Swiegers estimated that bubble-induced overpotentials in traditional alkaline electrolyzers contribute  $\sim 300$  mV of excess overpotential at current densities > 0.5 A cm<sup>-2</sup>. Nevertheless, gas—liquid interfaces are required to maintain a low partial pressure of dissolved gas in the electrolyte, since accumulation of product  $H_2$  and  $O_2$  leads to a shift in the cell voltage as described by the Nernst equation (eq 2). For example, Deng et al. measured the

voltage of individual electrode lamellae within a zero-gap alkaline electrolyte and found that the total contribution of gas bubbles to the overpotential was 50 mV ( $\sim$ 4% of the total overpotential) at J=0.5 A cm<sup>-2</sup> and that the net effect of "free" gas bubbles is a *reduced* overpotential.<sup>214</sup> Here, we summarize the various effects of gas bubbles in AWE-type cells and the key works which identified these effects.

Most models for gas transport and the consequences of interfacial and free bubbles have been developed for electrodes separated by a narrow electrolyte gap and most often facing a porous diaphragm (Figure 15a). This is consistent with the dominant configuration for alkaline electrolyzers installed throughout the 20th century. Advanced AWE approaches employ a "zero-gap" design where gases are removed outside of the electrode/diaphragm interface and thus contribute minimally to the effective cell resistance (Figure 15b). This configuration was originally demonstrated by Lurgi's design for a pressurized AWE stack.  $^{66,207}$  Early designs for zero-gap electrolysis originally yielded  $J=1~\rm A~cm^{-2}$  at  $V<1.9~\rm V$  when operated in 42 wt % KOH at 110 °C.  $^{66,215}$  This approach has received renewed interested in the literature and new design elements such as ion-solvating membranes could further reduce the cell resistance.  $^{216,217}$ 

In the past decade, researchers have adapted porous electrode morphologies developed for fuel cell and PEMWE applications for AWE cells that directly produce gaseous  $O_2$  and  $H_2$ . In these electrodes, the classifications of "interfacial" and "free" bubbles have less importance (Figure 3a), but rather the porous electrode is in a wetted or dewetted state (Figure 3b). Marini and colleagues investigated alkaline electrolyzers configured with gas diffusion layers similar in design to those used in alkaline fuel cells and membrane electrolyzers, although comparisons of the individual electrode performance to the full cell performance suggested that some gases may still have formed at the electrode/separator interface. Winther-Jensen et al. demonstrated the concept of breathable AWE electrodes by generating  $O_2(g)$  from a hydrophobic Goretex membrane electrode at 10 mA applied current. Turek's group

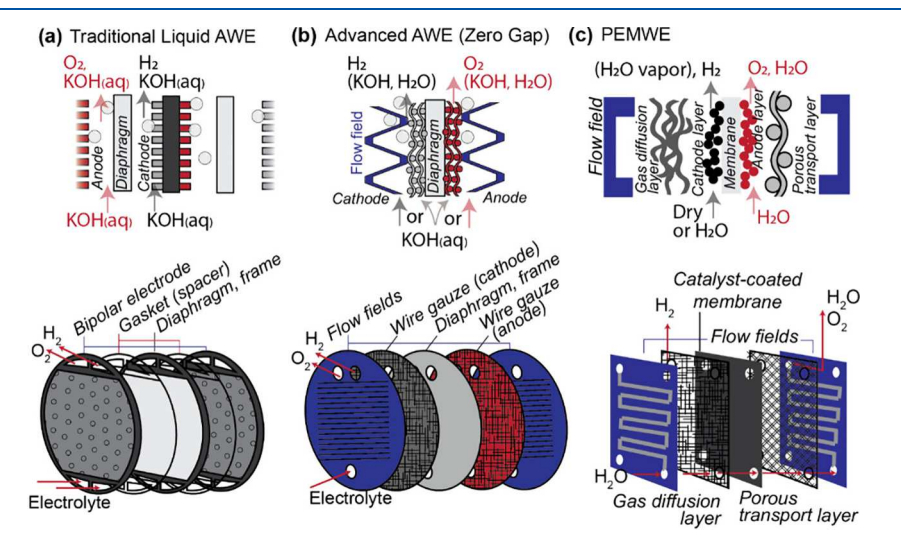


Figure 15. Cross section and exploded view of designs for traditional alkaline water electrolysis (a), advanced "zero-gap" alkaline water electrolysis (b), and proton exchange membrane water electrolysis (c). Zero-gap alkaline water electrolysis cells can be supplied with aqueous KOH to the cathode and/or anode and/or diaphragm, with bubble effects mitigated at electroles free of bulk electrolyte. Proton exchange membrane water electrolysis cells are typically fed with  $H_2O$  to the anode only, with proton conduction occurring in the solid polymer electrolyte, and  $H_2$  leaving as a humidified gas stream.

improved this hybrid approach as part of a zero-gap cell, using an immersed porous cathode coupled with a gas-diffusion electrode at the anode, which is similar in architecture to chloralkali stacks employing an oxygen depolarized cathode. The strategy was functional up to J =400 mA cm $^{-2}$  and controlling the wettability of the gas diffusion electrode through molecular and structural modifications was proposed as a pathway to greater  $J.^{220}$ 

Swiegers and Wallace have led significant improvements on alkaline water electrolysis by controlling the transport of gases and eliminating free gas bubbles. The strategy was first reported by Tiwari et al., wherein a porous polyether sulfone separator is kept in a wetted state by capillary action and both the anode and cathode act as gas diffusion electrodes.<sup>221</sup> Such "bubble free" alkaline water electrolyzers use both structure and surface chemistry to direct liquid and gas flows from the central separator through the porous anode and cathode, eliminating concentration overpotentials and leading to very low onset potentials for water electrolysis (Section 7.2, Figure 2). Hodges et al. improved on this design and reported 1 cm<sup>2</sup>scale cells which stably produced H<sub>2</sub> and O<sub>2</sub> gas at ~100% efficiency (based on the higher heating value,  $\sim 1.47$  V). The cell showed stable performance for 7 h at 80 °C and 300 mA cm<sup>-2</sup> and over 30 days of continuous operation at 400 mA cm<sup>-2</sup> at room temperature.<sup>222</sup> Most recently, Deng et al. reported a membrane-less design for bubble-free electrolysis at  $J = 1 \text{ A cm}^{-2} \text{ with } < 0.02\% \text{ H}_2 \text{ detected in the } O_2 \text{ product}$ stream.<sup>223</sup> We direct interested readers to a recent review from Swiegers et al. that thoroughly discusses cell-level and stacklevel approaches to bubble free electrolysis with an emphasis on academic literature and industry patents on alkaline electrolysis. 15 Molecular and microstructuring strategies for directed gas transport are discussed in Section 7.

In addition to cell-level strategies, many active mitigation strategies, including ultrasonication and applied magnetic fields, have been tested as ways to remove gas bubbles from electrode interfaces. Although these approaches have not found use in industrial systems for electrolytic hydrogen, they could perhaps play a role in electrolyzers used in reduced gravity environments where buoyant forces do not assist in gas removal. 43

5.2.2. Gas Evolution in Proton Exchange Membrane **Electrolysis.** Gas evolution in proton-exchange membrane water electrolyzers (PEMWE) occurs in a substantially different environment from alkaline water electrolysis. First, humidified  $H_2(g)$  is removed directly from the cathode through a gas diffusion layer consisting of a microporous layer of carbon. In this environment, protons are the reactants for the HER which are transported through the solid polymer electrolyte. Thus, the cathode can operate in the absence of liquid water and gas-liquid interfaces are marginal in extent and effect. On the other hand, water is required as a reactant at the anode, which can in principle be fed to the cell as water vapor but in practice is fed as liquid, deionized water. The wetting behavior of the anode catalyst film is complex and still poorly understood. Drying of the anode during operation at high current densities leads to substantial transport-related overpotentials. One advantage of PEMWE for hydrogen production is the capability of membrane electrolyzers to quickly increase (or decrease) power density to respond to the availability (or lack) of surplus electricity. Although water management can be a key performance bottleneck at high current density,  $J > 19 \text{ A cm}^{-2}$  have been demonstrated with

nanostructured catalyst coated membranes developed at 3M, which is  $\sim 10X$  higher than the modern industry standard J of  $2~{\rm A~cm}^{-2}$ . Because gas bubbles formed in PEM electrolyzers have little influence on the ionic resistance of the solid polymer electrolyte, the primary consequence of excess gassing is the prevention of reactant water from reaching the catalyst layer.

A porous transport layer (PTL), typically  $\sim 250 \mu m$  thick and made of Ti, is used to manage the ingress and egress of water and oxygen gas, respectively (Figure 15c). These bubbles do not affect the ionic resistance of the solid polymer electrolyte but still restrict access to catalyst sites (leading to increased observed  $\eta$ ) and constrain mass transport within the porous transport layer (potentially leading to a critical current density). 230 The design of optimized PTLs demands a balance of wettability to maintain efficient delivery of water and removal of gases from the reactive catalyst/ionomer region. The inverse problem is posed by PEM fuel cells which manage gas ingress and removal of product H2O as vapor, and unitized regenerative PEM cells (a combined electrolyzer/fuel cell) pose a yet greater challenge because both liquid and gas transport must be controlled depending on whether the device is currently being charged or discharged.<sup>231,232</sup>

Grigoriev et al. conducted an early systematic study on the effect of Ti porous transport layer structure on the performance of PEM cells. The authors discuss a potential trade-off between the need for a densely packed current collector and wide pores to prevent excess capillary pressures for bubble removal. Porous transport layers were compared in MEAs with 2 mg cm<sup>-2</sup> of Ir coated on the membrane or current collector, and the optimum pore diameter was found to be  $12-13 \mu m$ independent of the method of catalyst coating.<sup>233</sup> Suermann et al. studied the effect of porosity within Ti PTLs prepared from various particle sizes and having modal pore diameters 16-22  $\mu$ m. The onset of mass transport limitations was measured as a function of applied J ( $\leq 4 \text{ A cm}^{-2}$ ), pressure ( $\leq 100 \text{ bar}$ ), and temperature (40-60 °C.<sup>234</sup> Transport-related overpotentials required >150 mV of applied voltage at  $I = 4 \text{ A cm}^{-2}$ , relative to the predicted voltage from extrapolating the cell voltage from lower current densities unhindered by transport. Lopata et al. analyzed the effect of PTL structure on the measured cell impedance for PEM water electrolysis cells with two loadings of Ir at catalyst-coated membranes (0.085 mg Ir cm<sup>-2</sup> and 0.595 mg Ir cm<sup>-2</sup>). With the higher catalyst loading, the cell impedance was insensitive to PTL structure, whereas for the low catalyst loading narrower pore openings minimized inplane ohmic losses. The apparent bubble coverage was calculated from changes in the kinetic overpotential after correcting for high frequency impedance. For the higher catalyst loading was found to depend on both the pore diameter and water flow rate, but while larger apparent bubble coverages were measured for lower catalyst loadings, there was no clear relationship between the calculated coverage and pore diameter.235

Other factors, such as the surface treatment of Ti gas diffusion layers and the pore structure influence transport properties during electrolysis at high J. Bromberger et al. showed that the contact angles at PTLs prepared from Ti felts and a layer of sintered Ti powder is strongly influenced by the interfacial titanium oxide layer that forms during polarization of the anode. <sup>236</sup> Mass transport limitations were not observed for  $J \leq 5$  A cm<sup>-2</sup> for PTLs with a modal pore diameter of 27 or 63  $\mu$ m, whereas the finest porosity PTL prepared from

powders exhibited mass transport limitations at J > 1.5 A cm<sup>-2</sup>. Lickert et al. investigated  $J \le 5$  A cm<sup>-2</sup> and estimated the mass-transport losses resulting from a variety of Ti PTL structures.<sup>237</sup> In addition to the structure of the PTL, the onset of transport limitations was strongly dependent on the flow rate of deionized water as well as the operating pressure.

PTLs with graded porosity and hierarchical structures have been employed to maximize electrical contact or catalyst area at the membrane while mitigating the transport resistance for water and O2 passing through the PTL. Stiber et al. sintered a microporous Ti layer on an expanded Ti mesh, showing that the addition of a microporous layer to the mesh avoided the onset of mass transport limitations at  $J \le 6$  A cm<sup>-2</sup> at 90 °C and significantly reduced the effective charge transfer resistance measured via galvanostatic electrochemical impedance spectroscopy, EIS, at J = 4 A cm<sup>-2.238</sup> Lettenmeier et al. implemented a new technique, vacuum plasma spraying, which produced PTLs with graded pore radii from 2-10  $\mu$ m. <sup>239</sup> Schule et al. prepared hierarchically structured microporous layers to minimize the use of expensive, fine titanium powders, while providing even current distribution to the catalyst-coated membrane and providing large pores for gas removal.240

Bazylak prepared custom porous transport layers (PTLs) for PEM with patterned through pores are used to reach  $J=9~{\rm A}~{\rm cm}^{-2.241}$  Pores were machined into a commercially available PTL and shown to improve performance, with the pores strategically placed under regions for liquid water flow within the bipolar plate. The effect was a reduced mass transport overpotential at high current densities, which correlated with an increased frequency of bubble detachment. The same group has done much work to develop *operando* imaging with X-ray and neutron sources on cells at high current densities, which have correlated gas filling with the onset of a critical current density during PEM electrolysis (Section 6).  $^{230,242}$ 

Recently researchers have focused on controlling the structure of catalyst layers to promote gas release. Kim et al. used solvent-assisted nanotransfer printing to prepare ordered films of Ir nanowires in a "woodpile" geometry, serving as an anode catalyst layer in a PEM water electrolyzer. This catalyst layer yielded a mass activity of 140 A mg<sup>-1</sup> at 1.8 V. Although larger spacings between NW led to greater overall performance, an intermediate spacing led to the greatest mass activity of Ir, and a simpler, parallel stacking of NWs led to reduced activity for electrolysis. 137 Tian et al. used an anodic aluminum oxide template to prepare a structured membrane/iridium oxide catalyst interface. The resulting membrane electrode assembly yielded exceptional mass activity toward the OER at 2.0 V and behaved as a "superaerophobic" surface toward O2 gas bubbles.<sup>243</sup> Zhang et al. prepared microstructured Ir catalyst layers by electroplating Ir onto gas diffusion layers coated with polystyrene spheres, finding that this catalyst layer minimized gas coverage and improved efficiency as compared to dense Ir layers.<sup>217</sup> Lv et al. prepared an anode catalyst layer with a hierarchical distribution of pore sizes across three sub layers, leading to improved performance at high J (3 A cm<sup>-2</sup>). CuO was used as a pore-forming agent, with particles of 40 nm, 50-100 nm, and 150-250 nm incorporated into the catalyst layer precursor and then leached in 10 wt % H2SO4. Mass transport overpotentials were estimated as a residual contribution to the cell voltage, assuming Tafel-like contributions of activation overpotentials and a constant cell resistance; increasing pore sizes from the membrane to the PTL led to the lowest overall cell voltage at 3 A cm $^{-2}$ . $^{2.442.46}$  Yuan et al. studied the influence catalyst structure on gas detachment diameter by imprinting an unsupported iridium oxide catalyst layer with a commercial Ti mesh, leading to a surface texture similar to that expected in a membrane electrode assembly compressed by porous transport layers. $^{247}$  Tao et al. used IrRu nanosheets supported on a layer of Pd nanowires to improve in-plane conductivity and enhance water/gas transport to a porous transport layer. $^{248}$  A PEM cell using a catalyst-coated membrane configuration maintained a stable performance of  $E \sim 1.8 \text{ V}$  at I = 2.0 A cm $^{-2}$  for 200 h (degradation rate 0.025 mV hr $^{-1}$ ) with most of the degradation in the catalyst layer coming from dissolution of the Pd support rather than the Ir or Ru nanosheets.

# 6. OPERANDO CHARACTERIZATION OF WATER ELECTROLYSIS

The experimental study of electrochemically generated bubbles and their effects on water electrolysis can be differentiated by the scale at which the experiments are focused. "In situ" denotes the characterization of the effects of bubble evolution on narrow segments of the water electrolysis reaction. An example is a measurement of the relationship between the distribution of nanoparticle electrocatalysts on an electrode surface and O2 evolution rates from the OER half reaction occurring on that electrode. "Operando" denotes the study of full electrolysis reactions, even if the system is constructed for experimental feasibility rather than real deployment. The distinction is important because materials and interfaces for these reactions can be engineered considering multiscale effects where the focused, in situ experiments are necessary. In this sense, operando is used here to describe experimental characterization of integrated electrolysis systems.

#### 6.1. Optical Operando Characterization

Optical characterization is a convenient technique for characterizing free and interfacial bubbles when the gas coverage is not so high that individual bubbles cannot be resolved. Industrial electrolysis cells do not use transparent components, but researchers have developed transparent flow fields to visualize *operando* gas transport. Transparent electrolyzers with model pore openings have provided insights into gas bubble dynamics and device-relevant J. Zhang's group has developed a transparent cell for visualizing gas evolution at membrane electrolyzers, by replacing thick end plates with a thin current collector with pores >100  $\mu$ m in diameter. <sup>249–251</sup> This design allowed visualization of the three-phase boundary between the catalyst, the membrane, and the porous transport layer responsible for current conduction.

Mo et al., used a transparent cell along with optical microscopy to image bubble evolution on the anode of a PEM electrolysis cell.  $^{249}$  The results showed that  $\rm O_2$  was primarily formed at the edges of the porous anode rather than being uniformly distributed across the catalyst layer. Although it is important to note that the absence of bubbles does not necessarily confirm that the bulk of the catalyst layer is inactive, the results do show that the layered structure of a PEM electrolysis electrode can be designed to mitigate the negative effects of bubble persistence across the bulk catalyst layer. The same group used high speed optical microscopy to confirm the observed bubble dynamics in an *operando* PEM electrolysis cell through an optically transparent window into the anode compartment.  $^{251}$ 

Li et al., used high speed optical microscopy to image the oxygen bubble dynamics in a transparent PEM electrolysis cell under the influence of both current density and fluid flow. The cell included a porous Ti felt gas diffusion layer (GDL), which provided porosity at both the felt-pore scale and the larger channel scale. Increasing J caused bubbles to detach from the porous felt layers more quickly and at larger diameters, but flow through the electrolyzer channels helped to remove bubbles from occupying the pores in the GDL and the channels. The group also studied the structure of the GDL by comparing the Ti felt to a thin foil with a regular pattern of perforation. 252 The resolution of high speed optical microscopy (6000 fps) was sufficient to characterize the structure of gas flow through channels with a thin electrolyte layer in the anode compartment of a PEM electrolyzer. The structure of the GDL influenced the migration and coalescence dynamics of bubbles in the channel. The main problem of interest was the formation of "slug" bubbles that were so large as to clog the electrolyzer flow channels. The researchers found that the porous Ti foil GDL was able to control the frequency and size of O<sub>2</sub> bubbles leaving the layer. This reduced the frequency of slug formation by up to four times compared to the Ti felt GDL. As a result, the time-averaged V and the frequency of abrupt, transient increases (at fixed J) were reduced. More recently, the same group has used the method of visualizing gas evolution within the PTL to understand the effects of electrolyzer conditioning on gas release at Ir-based anodes. They also prepared in-plane channels to connect through holes patterned into a Pt-coated Ti GDL which supported I > 9 A cm<sup>-2</sup> as compared to a  $I \sim 6$  A cm<sup>-2</sup> for GDLs without in-plane

Dedigama et al.<sup>254</sup> developed a PEM water electrolysis cell with multiple identical flow channels, including a central one with an optical window. This setup was devised to image bubble transport at high frame rates (7000 fps) as well as map temperature changes (via thermography) of anin operando water electrolysis cell  $(J = 0.2-1 \text{ A cm}^{-2})$  and varying the fluid flow rate through the channel (stagnant to 10 mL min<sup>-1</sup>). The experiments particularly focused on comparing the transport of electrolytically evolved bubbles to an effective phase diagram of bubble transport in flow as originally defined by Mishima and Hibiki (Figure 16).<sup>255</sup> At the highest current densities (1 A cm<sup>-2</sup>), the researchers observed slug flow of bubbles in the channels at all fluid flow rates. Slug flow was induced at lesser J by reducing the fluid flow rate. Both the fluid and gas velocities were below the predicted threshold for more turbulent bubble flows, such as churn or annular flow, which could potentially be favorable for mass transport. The researchers did observe a correlation between slug flow for bubble transport and improved mass transport overpotentials in the electrochemical operation, possibly due to the clearance of persistent bubbles by frequent contact with slugs.

Optical imaging has also been used to characterize the connection between evolving bubbles and electrolysis in anion exchange membrane water electrolysis cells. Wan et al. used a conical template to structure a dense electrocatalyst layer with microstructure to promote bubble departure. The effective operating principle was to push bubbles away from active surface area, preventing bubble contract from increasing transport overpotentials. The microstructure reduced the internal resistances related to bubble persistence in the electrolysis process which resulted in notably high current

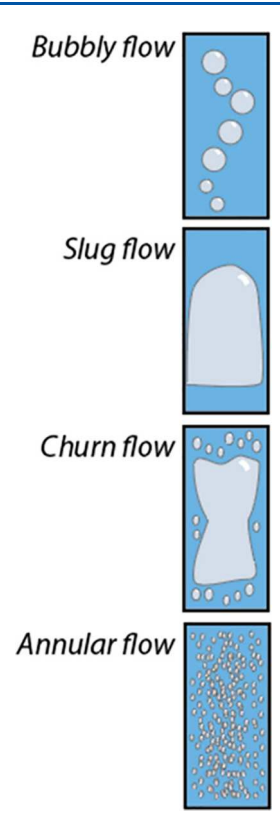


**Figure 16.** Schematic depiction of flow types for bubbles in a cylindrical tube based on findings from Mishima et al.<sup>235</sup>

densities for electrolyzers free of platinum group metal catalysts ( $I = 4 \text{ A cm}^{-2}$  at V = 2.0 V in 1 M KOH).

Eckert's group employed a machine-learning-based approach to filter bubbles which are not in the plane of focus, thus avoiding erroneous measurements of bubble diameter. 257 The diameter of detached H<sub>2</sub> bubbles was strongly affected by the mesh geometry and flow rate for gas evolved at low current densities  $(J = 10 \text{ mA cm}^{-2})$ , with the thicker expanded mesh releasing bubbles as small as 30  $\mu$ m under forced convection and thinner meshes releasing bubbles as large as 90  $\mu$ m in a cell with no forced convection. However, for J relevant to alkaline water electrolyzers (200 mA cm<sup>-2</sup>), the bubble diameter converged to  $80-95~\mu m$  for all meshes and flow rates, indicating that hydrodynamic forces generated by gas evolution are dominant over adhesion and external convection. High bubble coverages (>80% of the mesh area) were observed for all I and flow rates studied. One limitation of imaging with visible light is that only outer bubbles from a bubble plume can be quantified, such distribution of diameters across the full population of gas bubbles.

#### 6.2. Neutron Radiography Operando Characterization

Neutron radiography uses neutrons to image through multilayered materials, like X-ray radiography, and offers substantial differences in material interactions. Whereas X-ray attenuation is proportional to the electron density of materials, which increases monotonically with increasing atomic number, neutrons can transmit through materials such as metal layers which are opaque to X-rays or optical light (Figure 17a). Neutron attenuation occurs through the specific interactions between incident neutrons and nuclei and has a strong dependence on the kinetic energy of the incident neutrons. Neutron absorption effects that are particularly relevant to

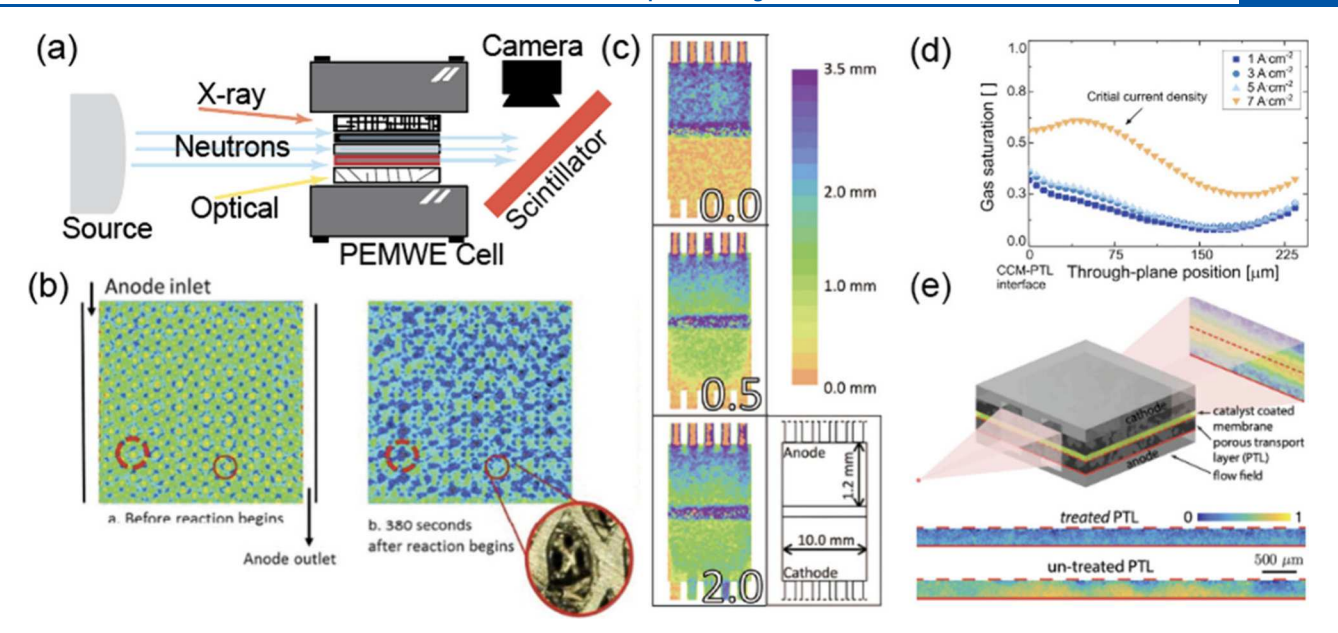


**Figure 17.** (a) Scheme of neutron radiography used for PEM electrolysis. Neutrons penetrate through membranes, PTLs and flowfields whereas X-rays and visible light are attenuated. (b) False colorized transient neutron images of a PEM electrolyzer at 40 °C and J = 100 mA cm<sup>-2</sup>. Reproduced with permission from reference. Copyright 2011 IOP Publishing (c) Neutron radiograms, averaged over 5 min of PEM electrolyzer as a function of J (A cm<sup>-2</sup>), reproduced with permission from reference. Copyright 2016 IOP Publishing. Color scale denotes water thickness. (d) Gas saturation profile of a PEM electrolyzer as a function of position averaged over 75 s and prior to the establishment of steady state as a function of the PTL thickness (through-plane distance), reproduced from reference. Copyright 2021 Elsevier (e) Spatial distribution of average gas saturation in a treated and untreated PTL on the anode side of a PEM electrolyzer operating at current density J = 5 A cm<sup>-2</sup>. The volume fraction of oxygen gas is estimated using the Beer–Lambert law. Reproduced with permission from reference. Copyright Elsevier 2021.

water splitting are the attenuation due to <sup>1</sup>H in water. Most other common materials, such as <sup>12</sup>C, <sup>16</sup>O, and some metal layers are relatively transparent to neutrons. <sup>258</sup> Dissolved gases and gas bubbles are therefore easy to image. Neutron radiography is used to image dissolved gas (via changes to attenuation) and bubbles in the polymer layers of an operational electrolyzer as a measure of local activity. In research-scale devices, it has mostly been used to measure gas flux out of the process as a function of the operating parameters (water flow, gas purging) or materials design choices (polymer layer material, porosity, etc.) in PEM electrolysis.

Selamet et al., first used neutron radiography to measure gas and fluid transport through a model PEMWE (Figure 17b). The radiography was performed in an orientation normal to the layer axis and used to characterize the gas volume generated at fixed J in the range of 100-400 mA cm<sup>-2</sup> as a function of the mesh structure, electrolyte flow, and temperature. Under "dry cathode" conditions, with water provided to the anode only and reaching the cathode via diffusion through the membrane, the thickness of the water layer could be measured in operando and was found to increase at the lower temperatures studied due to the lower evaporation rates. Moreover, water accumulated on the cathode side at higher current densities due to electroosmotic effects. Similarly, de Beer et al., imaged gas bubbles in the intentionally engineered channels of the porous transport layer (PTL) to show that structure could affect flow through the device.2

Seweryn et al., used neutron radiography to investigate gas transport in the plane of the membrane layers, perpendicular to earlier work (Figure 17c). The sintered Ti mech included was transparent to neutrons. Neutron radiography was used to measure water accumulation on the dry,  $H_2$ -purged cathode side as a function of flow rate across the anode. They found

that water accumulation on the cathode was sufficient to maintain  $H_2$  evolution, even for J > 2 A cm<sup>-2</sup>. Lee et al., used neutron radiography to resolve  $O_2$  bubble evolution at the anode and water accumulation in the cathode in a PEMWE fed with water only on the anode side.<sup>263</sup> They found that the performance of the dry cathode was not much different thanin a PEMWE where water is also fed to the cathode. The membrane design drew sufficient water through the membrane to the cathode. The hydration of the membrane and wetting state of the cathode layer was also measured as a function of the gas flow rate of the cathode purge gas  $(N_2, 0.5 \text{ L min}^{-1})$ .

The Bazylak group has used neutron radiography to connect macroscopic cell performance metrics to microscopic gas transport processes at industrially relevant current densities. Lee et al., characterized an observed inflection point in the current-voltage characteristics of a PEM water electrolysis cell.<sup>230</sup> The researchers first observed a flow-dependent inflection in this increase, which was classified as the critical current density, above which the slope of the characteristic J-V curve increased (Figure 17d). To characterize the mechanistic cause of this inflection point, the researchers measured the distribution of gas via operando neutron imaging through the anode PTL as a function of I (up to 9 A cm<sup>-2</sup>) and flow rate (0.5-3.0 L min<sup>-1</sup>) through a conventional PEM electrolysis cell with a catalyst-coated membrane. They found that flow rate was a significant factor in gas removal. The lowest flow rates (0.5 L min<sup>-1</sup>) were insufficient to reduce gas clearance. Higher flow rates could clear the gas saturation near the catalyst layer until the cell reached the critical current density. This was a direct observation of cause and effect in the electrolysis process. The same group used faster operando Xray imaging (again, via Beer-Lambert attenuation analysis) to characterize the diffusive clearance of gas near the catalyst layer in the anode PTL.<sup>242</sup> The imaging showed that the gas

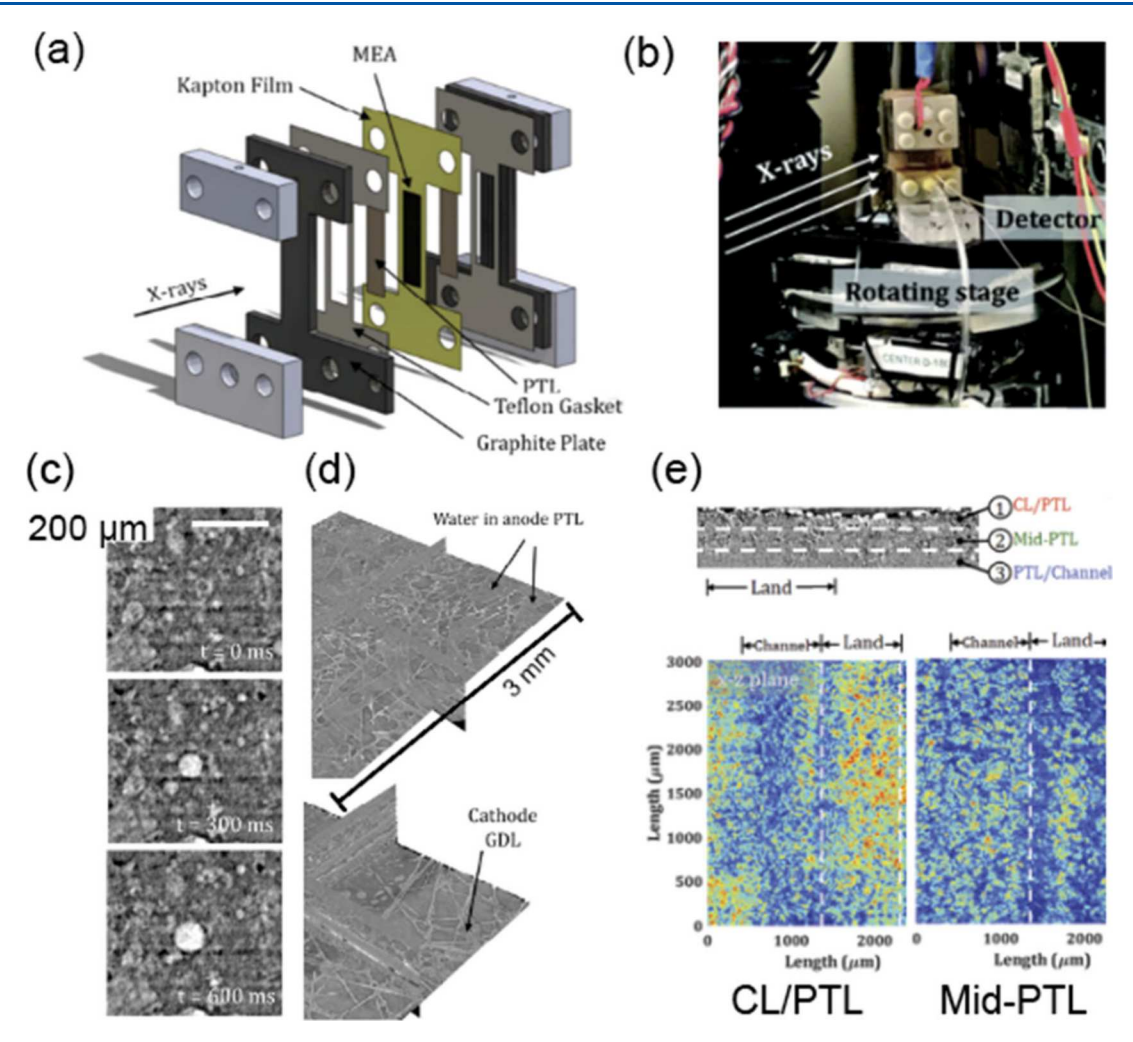


Figure 18. (a) Rendering of a custom PEMWE cell designed for operando X-ray radiography and tomography studies. (b) Photograph of an experimental set up for operando X-ray tomography (c) Time series X-ray radiography of an  $O_2$  bubble generated within a PTL. (d) X-ray tomography of an anode PTL and cathode GDL showing the presence of wetted and dewetted channel. (e) Spatial distribution of oxygen content at the catalyst layer/PTL interface and in the center of the PTL as measured by X-ray tomography, red indicates oxygen saturated and blue indicates oxygen free (a,c,d) Reproduced with permission from reference. Copyright 2018 Elsevier. (b) Reproduced with permission from reference. Copyright 2021 Royal Society of Chemistry. (e) Adapted with permission from reference. Copyright 2020 Elsevier.

accumulation occurred with very little time delay in response to a ramping current. The reverse process was very slow, however. The saturation cleared by diffusion at open circuit (i = 0) with a decaying profile time constant of roughly 500 s. The rapid saturation and slow clearance dynamics shows that gas saturation "hysteresis" should be accounted for in the design of PTL layers. Later, Zhao prepared superhydrophilic PTLs using a chemical surface treatment and then used operando neutron radiography to characterize the effect that the superhydrophilic treatment had on gas saturation in the PTL (Figure 17e), <sup>262</sup> finding that the cell voltage decreased significantly whey using the treated PTL versus the conventional one over virtually the entire tested range of J (0.2–9 A cm<sup>-2</sup>). This supported the hypothesis that reduced gas accumulation was the cause of the observed reduction in overall operating V, as the superhydrophilic PTL had roughly half of the integrated gas content of the untreated PTL at  $J \leq 5$ A cm<sup>-2</sup>. Whereas the untreated PTL was incapable of achieving the highest targeted J (8 A cm<sup>-2</sup>)—resulting in a "runaway voltage" due to total loss of electrolyte within the porous electrode—the superhydrophilic PTL operated at reasonable cell potentials across the full range of *J*.

#### 6.3. X-ray Radiography Operando Characterization

X-ray imaging has also been used to image bubble evolution in operando . The transparency issues mentioned in the prior in situ discussion require special system designs, but there are potential advantages to imaging with X-rays. These include higher frame rates for studying faster dynamics and the potential for higher spatial resolution than either neutron or optical imaging.

Selamet et al. imaged bubble in a reversible, regenerative membrane-electrolyzer assembly (MEA) fuel cell in reverse (electrolysis) mode using soft X-rays (having a wavelength between 20 and 200 Å). The authors measured the dynamics of gas bubbles along a single flow channel at relatively low J (<25 mA cm<sup>-2</sup>), with both sides of the membrane fed with deionized water. Two main effects were observed at low current densities: (i) that bubbles persisted at specific sites in the polymer channel, and were less frequently observed to nucleate and grow directly on the electrocatalyst (ii) that the behavior of bubbles at the anode was different than the behavior of bubbles at the cathode, with  $O_2$  departing quickly as small bubble streams, but  $H_2$  bubbles persisting on

the cathode side to a larger departure diameter. Hoch et al., performed more detailed X-ray radiography studies on the relationship between  $H_2$  evolution and bubble persistence in the PTL of a PEMWE. <sup>265</sup> At low |J| (10 mA cm<sup>-2</sup>), the authors observed a notable spatial regularity and dynamical periodicity to bubble discharge. This suggested that bubbles nucleated at specific sites in the PTL and grew slowly with low gas evolution rates until buoyancy caused them to discharge. At much greater absolute current densities, the regularity was upset. Much smaller  $H_2$  bubbles were observed at the greater J suggesting the growth and clearance mechanisms are different at high current densities, likely due to more frequent coalescence between bubbles.

Lee et al. also studied gas accumulation and bubble detachment dynamics in commercial PTL materials with intentionally fabricated, 400  $\mu m$  diameter through-holes (Figure 17e). The electrochemical effect of these throughholes was a 4-fold reduction in the mass transport induced overpotential at high J ( $\leq 9$  A cm<sup>-2</sup>). The researchers used operando neutron radiography to image along the stack dimension to measure the volume fraction of gas within the PTL, f, as a function of distance from the catalyst layer. Using Beer-Lambert attenuation analysis to measure gas content from radiographs, the researchers could quantify f as a function of depth with roughly 15  $\mu$ m spatial resolution. Imaging of the pore-free PTL showed that the gas fraction within 50  $\mu$ m of the catalyst layer was roughly f = 0.4 - 0.5 at  $J \ge 1$  A cm<sup>-2</sup>. The same PTL material with the through-pores had negligible gas fraction in the same region of the PTL at low I and reached a maximum value of f = 0.25 at 9 A cm<sup>-2</sup>, the highest J tested. They then used operando X-ray radiography to image bubble motion in the plane of the PTL. The pores induced more rapid coalescence and departure of growing bubbles, which in turn led to improved wetting of the catalyst layer. This explained the influence that the through-pores had for the observed reduction in gas saturation and mass transport overpotentials.

Lenhart et al., used synchrotron-based X-ray tomography to image the in-plane propagation of  $H_2$  bubbles in the cathode PTL layer, <sup>267</sup> seeking to understand the relationship between the structure of the PTL and the mass transport issues induced by gas bubbles near the electrode. X-ray imaging showed that the gas bubbles migrate through the PTL layer following the same path at a fixed J of 0.2 A cm<sup>-2</sup>. Increasing J (up to 0.6 A cm<sup>-2</sup>) resulted in bubbles following new branches off of the paths followed at the lower current densities. This work serves as a representative example of how that the pore structure of the PTL can be tailored to drive the removal of bubbles away from the catalyst (Section 7.2)

Kalhani et al., used synchrotron-based X-ray radiography to study the distribution of oxygen bubbles in a PEM-based water electrolyzer,  $^{268}$  with aim of identifying relevant mass transport losses for Ti PTLs composed of a fibrous mesh or sintered particles.  $\mu\text{CT}$  was used to characterize the porosity, which was higher in the fiber-based PTL than for the sintered PTL. Given fixed water flow through the electrolyzer (3 mL min $^{-1}$ ), operando X-ray radiography was used to characterize  $O_2$  gas accumulation in the anode PTL as well as the removal of gas bubbles in the channel. The researchers found that the less porous, sintered PTL saturated with has at the highest catalyst loadings tested (>2.0 mg cm $^{-2}$ , as determined by  $\mu\text{CT}$ ), resulting in a significant increase in the cell potential ascribed to mass transport overpotentials. At the lowest catalyst loadings tested (0.6 mg cm $^{-2}$ ) the fibrous PTL generated

saturation at lesser *J* due to the higher density of bubble nucleation sites generating an increase in the observed frequency of slug-type bubble congestion in the flow channels.

The Zenyuk group has combined operando studies of PTL with advanced tomography of the structure of PTLs and catalyst layers (Figure 18). Leonard et al. combined operando X-ray radiography with pre- and post operando X-ray computed tomography (X-ray CT) as a multimodal approach to characterizing changes in a custom PEMWE designed to minimize attenuation of X-rays (Figure 18a).<sup>269</sup> X-ray radiography allowed for the researchers to image the dynamics of bubble motion and water distribution in the channels of the PTL (Figure 18b), whereas tomography revealed the presence of wetted and dewetted regions within the anode and cathode PTLs (Figure 18c-d). Elemental absorption sensitivity of X-ray CT further enabled the researchers to generate 3D reconstructions of the migration of metals from the IrRuO<sub>x</sub> OER electrocatalyst and Pt HER electrocatalyst after electrolysis. Radiography showed that the residence time of bubbles in the PTL layer decreased with increasing J (50 mA cm<sup>-2</sup> to 200 mA cm<sup>-2</sup>). X-ray CT showed that the IrRuOx OER catalyst thinned, which is explained by the loss of metal in the recirculating water. The Pt HER catalyst was observed to migrate and redeposit throughout the porous PTL layer. Satjaritanun et al. used X-ray-based tomography to image the 3D migration of O<sub>2</sub> bubbles through the anode PTL layer.<sup>270</sup> The  $\mu$ CT experiments (pixel dimension = 1.3  $\mu$ m) used radiography to contrast gas bubbles from liquid and carbon fiber-based PTL by comparison to the same structure held at open circuit-hence, no bubble evolution. Through relatively rapid rotations of the system (each complete sinogram for the CT was measured in 6 min), the researchers could use the CT reconstructions to image the evolution of pore-scale O<sub>2</sub> content within the PTL. This 3D imaging showed that O<sub>2</sub> was significantly higher in concentration near the catalyst side versus near the flow side of the PTL, and that the flow field channels influenced the local activity of the catalyst layer (Figure 18e). The preferential flow of O<sub>2</sub> bubbles through the PTL was hypothesized to occur based on paths of least resistance (either larger pores or more hydrophobic) through the pore network. This result agreed with several observations in more specialized in situ experiments.<sup>239</sup> Leonard et al. then used the same  $\mu$ CT technique to characterize similar behaviors of O2 bubble migration as a function of the catalyst and stack structure.<sup>271</sup> This further suggests that the pore structure of the PTL can be tailored to control wetting, improve bubble drainage, and thus reduce the related mass transport overpotentials.

Kim et al., studied fabricated through-pores in the PTL that were either only coincident on the anode/cathode flow channels or under both the channel and the land. The addition of channels under the land resulted in an increase in gas saturation near the catalyst layer and larger mass transport overpotentials, consistent with findings from Satjaritanun. These authors attributed the finding to reduced contact area between the PTL and catalyst, a barrier to fresh flowing electrolyte, limited in-plane mass transport, and higher compression on the porous catalyst layer which reduced the overall active surface area.

#### 7. MODELING AND SIMULATION

Theoretical descriptions of bubble formation, evolution, and steady-state behavior have contributed to the understanding of

 $H_2$  bubble behavior by complementing and aiding in the interpretation of experimental work. These works use analytical or numerical methods to solve equations describing a subset of the relevant physical processes (Section 3). Notably, these works study a broad range of length scales  $(10^{-10}-10^{-5}\ m)$  and time scales (fs to s) to address different scientific enquiries.

#### 7.1. Molecular Dynamics Simulation of Nanobubbles

The most detailed descriptions of gas bubble formation come from molecular dynamics (MD) simulations. These calculate the forces on each molecule or atom within a defined volume to determine their trajectories over a period of time.<sup>273</sup> The position and velocity of every solvent and gas molecule are accounted for at every time step (Figure 19), which produces a

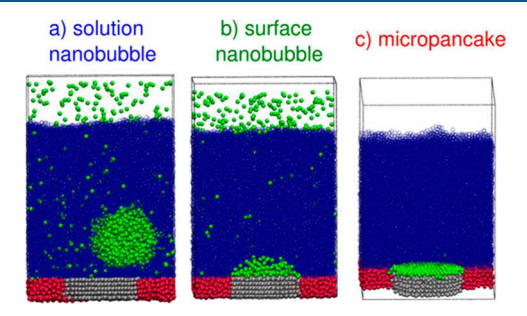


**Figure 19.** Snapshots of MD simulation trajectories in three different regimes of nucleated nanobubble relating to different relative surface energies for the gas/electrolyte interacting with the electrode. From left to right: electrolyte-electrode energy is greater than, approximately equal to, or less than, the gas-electrode surface energy. Reproduced from reference. <sup>69</sup>

highly detailed description of the bubble at the cost of computational expense. To accurately capture the behaviors, the time steps of the simulation must be comparable to those of molecular motions (i.e., on the order of fs). 69,273 Moreover, in MD simulations the number of atoms, and thus degrees of freedom, scale with the volume of the region simulated. <sup>69,273</sup> Thus, MD simulations are presently restricted to considering nanoscopic regions and process time scales on the order of 100 ns. For example, Perez-Sirkin et al. simulated a  $10 \times 10 \times 15$ nm box containing 33,400 water molecules a period of 100 ns to understand the nucleation and stationary state of a single nanobubble on a nanoelectrode.<sup>69</sup> The short durations of MD simulations are well suited to answering questions about individual nanobubbles. For example, they have been used to answer the mechanism of nucleation as well as the stationary states of electrochemically generated bubbles, 69 providing insight into the current invariance (as a function of potential) for single bubbles on a nanoelectrode (Section 4.1.2).<sup>274</sup>

Both methane<sup>69,274</sup> and N<sub>2</sub> have been used as model gases<sup>275</sup> generated at the surface of an electrode, which are assumed to represent an electrochemically generated gas that is not in equilibrium with the bulk solution. With appropriately chosen interactions between the gas and the electrode surface these results may be representative of behavior calculated for H<sub>2</sub> nanobubbles. Molinero, Scherlis and co-workers<sup>69</sup> assessed the impact of systematically varying the water-electrode and gas-electrode binding energies on nanobubble nucleation and stationary states at a nanoelectrode. They determined three regimes where a solution nanobubble forms near to the electrode surface (i.e., when electrolyte-electrode energy exceeds the gas electrode energy), surface nanobubble

nucleation (i.e., when gas-electrode energies are balanced with electrolyte-electrode energy), or a flat *micropancake* geometry with no curvature forms (i.e., when gas-electrode energies exceed electrolyte-electrode energy) (Figure 19). The same groups continued their investigations of the experimentally observed insensitivity of current to potential when a nanobubble is situated on a nanoelectrode (Section 4.1.2).<sup>274</sup> They showed that the bubble geometry changed with potential, from a so-called *leaky regime* at lower driving forces, where the bubble does not cover the entire electrode surface, to a *tight regime* where the bubble extends to the electrode perimeter. They also concluded that these currents should be insensitive to the electrode size, indicating that arrays of nanoscale catalysts are preferable to a continuous catalyst region.

Ma et al.<sup>275</sup> and Xi et al.<sup>276</sup> built on earlier simulations by developing algorithms for the generation of gas at the electrode surface. Ma et al.'s work investigated the dynamic equilibrium of a nanobubble on a nanoelectrode as a function of electrode size, solvent, and nanobubble morphology.<sup>275</sup> Their simulations showed that under appropriate conditions (nonaqueous solvents) experimentally observed oscillations<sup>277</sup> in the bubble pinned to an electrode surface may be observed, as attributed to differences in electrode—electrolyte surface energy and gas solubility. Xi et al.'s simulations demonstrated the maintained validity of classical nucleation theory, which is based on continuum physics (Section 3.3.1) and had previously been applied to experimental data for nanobubble nucleation<sup>30,37</sup> even at the length scale of several nm.

A broader range of MD simulations are available for interfacial bubbles generated by processes other than electrochemical reactions.<sup>278</sup> These simulations have investigated features which are important for practical electrodes, including rough surfaces.<sup>279</sup> When adapted to electrochemical systems where gas is generated at an electrode surface, these simulations may provide insight into the strategies for mitigation/control of bubble nucleation, as discussed in Section 8. Notably, Maheshwari and Harvey employed one of the few nonequilibrium MD simulations of gas generation at a rough surface.<sup>280</sup> While the amount of oversaturation required for nucleation was maximal for planar surfaces, the amount of oversaturation was not exclusively controlled by the roughness parameter and was found to depend on the geometry of the surface features.

#### 7.2. Continuum Models of Individual Bubbles

Continuum models describe physical systems using quantities which vary over space and/or time. For example, while molecular dynamics would describe the location of each molecule of a species, a continuum model would describe the concentration of molecules. As a result, continuum models require less parameters than MD to describe a given volume and can simulate much greater scales of length and time. They may be used to simulate individual interfaces, or components, or even entire electrolyzers.<sup>281</sup>

Within continuum models, the same physical process may be described with differing levels of detail, with more detail coming at a cost of increased computational expenditure. For example, transport of bubbles in solution may be described on the level of individual bubbles with prescribed interfaces, or by using volume averaging, whereby the quantity of H<sub>2</sub> in aqueous and gaseous phases per unit volume are the simulated quantities. For a detailed review of the mathematical

formulations of these and other models for electrochemical gas-evolving systems, we direct the reader to the recent reviews of Alshawabkeh et al.<sup>282,283</sup> The solution of the underpinning analytical expressions are tractable for a few simple systems, but more complex systems require numerical methods for solution. There are a range of numerical solutions to the partial differential equations that describe H<sub>2</sub> bubbles in electrolyzers, such as the finite element method, finite volume method, finite difference method, or lattice Boltzmann simulations. We do not focus on the computational details of these methods, but on the relevance of the results of the calculations on H<sub>2</sub> bubbles in electrolyzers, starting with detailed models of individual bubbles such as those formed at nanoelectrodes<sup>102</sup> or nanoparticles.<sup>129</sup> These models have been used to assess multiple stages among the lifecycle of a bubble (Figure 1).

7.2.1. Nucleation. Luo and White used finite element simulations of the steady-state transport processes immediately before nucleation to determine the concentration at which a single bubble nucleates on a nanoelectrode (Section 4.1.2). 102 The simulations show that the maximal concentration at the surface of the electrode (~0.27 M) greatly exceeds the 0.8 mM saturation concentration at standard state (Figure 7). Through the relationship between this concentration and the internal pressure in the bubble, and using a revised determination of the surface H<sub>2</sub> concentration required to induce nucleation (0.23 M), German et al.<sup>29</sup> calculated that a nucleating bubble would have a radius of curvature of ~3.6 nm, which would equate to 1700 molecules in a spherical bubble (less for spherical cap bubbles). Similarly, Georgescu et al. simulated H<sub>2</sub> transport in the SECCM measurements of H<sub>2</sub> bubble nucleation on single Pt nanoparticles. 129 Using the critical current for nucleation, they determined a similar critical concentration for nucleation as 0.31 M, with a distribution of concentrations seen between particles.

**7.2.2. Steady-State.** Finite element simulations that described  $H_2$  equilibrium at the gas—liquid interface to understand the current response with dynamically stable nanobubble on a nanoelectrode (Section 4.1.2)<sup>102</sup> were later extended by Liu et al., who performed a detailed assessment of the relationship between the steady-state current and geometric properties (radius, contact angle, etc.) for a single bubble on a nanoelectrode.<sup>72</sup> Considering that for a stable bubble the gas entering the bubble must equal to that leaving allowed assessment of steady-state geometries and their relationship to the residual current in both disk-in-plane and recessed-disk nanoelectrodes.

**7.2.3. Dynamics.** Van der Linde et al. simulated the electrolysis driven growth of  $H_2$  bubbles at a micromachined silicon electrode, finding that even at low current densities dissolved  $H_2$  accumulates within the boundary layer near the electrode surface. <sup>63,76</sup> The growth dynamics of  $H_2$  produced at a 30  $\mu$ m tall Si wire were broadly consistent with analytical solutions developed by Epstein and Plesset because the bubble quickly grew to a size that is large compared to the micromachined nucleation site. <sup>284</sup>

#### 7.3. Continuum Models of Electrodes

Continuum models of electrodes occur over larger length scales and must consider interactions between multiple gas—liquid interfaces. Vogt led early efforts to empirically model the mass transfer behavior of electrochemically generated gas bubbles considering the superposition of bulk electrolyte convection as well as convection within the "stagnant"

boundary layer at the electrode surface. 46 Vogt's early models contributed to the understanding how supersaturation varies with the rate of gas evolution near the electrode surface. These refined models in turn led to early models for the average ohmic overpotential at gas-evolving electrodes as well as the concentration overpotential (Sections 5.1.1 and 5.1.2). 44,285 Further work by Vogt focused on empirical models for the effective coverage of various electrode surfaces (and thus the relative inactive area of the electrode) in both vertical and horizontal orientations, across a range of operating current densities, and more recently considering the influence of operating temperature and pressure.

Recent models improved on the estimation of two-phase flows occurring in gas-evolving reactors. There are two main approaches to modeling two-phase flows in chemical reactor, which are distinguished by their representation of the gas phase. So-called Euler-Lagrange (E-L) models treat the electrolyte as a system of gaseous particles within a continuum liquid phase whereas Euler-Euler (E-E) models assume the electrolyte behaves as a volume-averaged two-phase fluid, thus avoiding explicit, computationally expensive interactions between gas bubbles (Eulerian representations of flows track velocities across the continuum whereas Lagrangian representations follow the motion of discrete fluid elements or particles).<sup>288</sup> Sokolichin et al. showed that the resulting flow patterns from these distinct approaches can be in quantitative agreement over long periods of simulation time, but both can fail for void fractions in excess of 10% as interactions between bubbles become important.<sup>289</sup>

Mandin et al. developed an early example of an E-L model for gas flow, considering bubbles 100  $\mu$ m and 1 mm in diameter produced at a generic vertical gas-evolving electrode. The authors assumed a homogeneous liquid electrolyte but considered the coupling between hydrodynamics and the current distribution at a vertical electrode. Gas bubbles were injected using Faraday's law and an arbitrary unknown force for dispersion of bubbles perpendicular to gravity was included to produce flow profiles that were more consistent with previous experiments. Despite 100  $\mu$ m bubbles being more consistent with experimentally observed diameters, the authors focused primarily on bubbles 1 mm in diameter because smaller bubbles led to unphysical void fractions. When external fluid flow was included within the simulation, the current distribution was independent of bubble size. Hreiz simulated the motion caused by discrete gas phases using an E-L model which considered both drag and buoyancy.<sup>291</sup> This approach captured key features from measured particle image velocimetry data. Velocity fields were used to study the convection caused by hydrogen bubbles throughout the entire volume of a narrow, vertical cell in a "no net flow configuration". The model focused on a monodisperse population of gas bubbles which detach from the electrode surface at a critical diameter, but did not consider mass transfer to or around surface-attached gas bubbles

As the void fraction increases >10%, E-E models are more suitable and dispersed flow is more commonly observed in vertical electrolyzers with a fluid gap. Higuera et al. studied the growth of hydrogen bubbles at a thin, porous catalyst layer in contact with a dilute solution of strong acid.<sup>292</sup> The model considered the relationship between nucleation density and applied current but did not consider the coalescence of neighboring bubbles. El Askary et al. applied an E-E model for two phase fluid flow to understand the bubbly flow in an AWE,

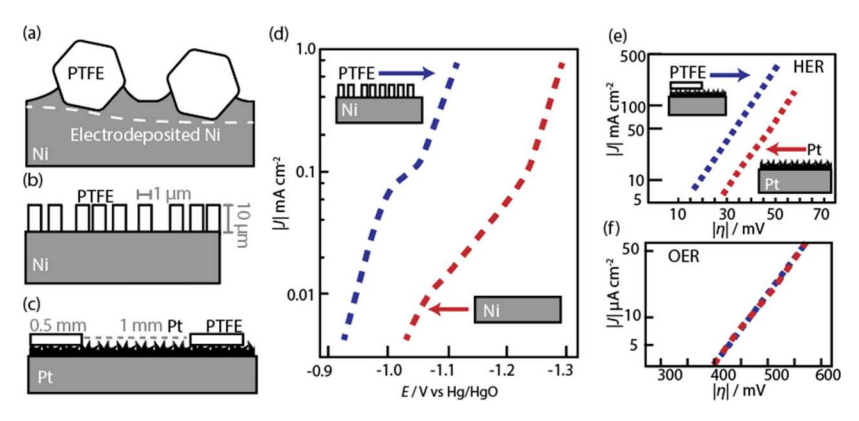


Figure 20. (a–c) Schemes of modified electrode surfaces. <sup>308,309</sup> (a) PTFE particles codeposited with electroplated Ni (b) Microstructured PTFE on a Ni surface (c) Patterned PTFE islands on a platinized Pt surface. (d) *J-E* behavior of nickel cathodes with (blue) and without (red) micostructured PTFE. <sup>309</sup> (e) *J-E* behavior toward the HER of platinized Pt cathodes with (blue) and without (red) PTFE islands. <sup>308</sup> (f) *J-E* behavior toward the OER for the same electrodes shown in (e). <sup>308</sup>

while considering interfacial transfer of both mass and momentum, and compared the numerical results to experimental measurements as a function of interelectrode spacing, applied *J*, and electrolyte flow.<sup>293</sup>

Colli and Bisang developed an E-E model to predict the current distribution in gas evolving electrochemical reactors which considers a range of bubble sizes and considers both coalescence and breakup of bubbles.<sup>294</sup> Whereas most models consider a constant bubble diameter, this model considers a distribution of bubble sizes which leads to more accurate predictions of hydrodynamic behaviors. The model predicts a previously observed phenomena: that gas fraction approaches a limiting value with increasing *J* where a transition from bubbly flow to slug flow occurs. The same authors revisited earlier calculations of the gas fraction by applying a more rigorous hydrodynamic model to explain the presence of a limiting gas fraction during electrolysis. 295 Chen and Lewis compared the resistance, concentration overpotential, and hyperpolarization of planar and microstructured electrodes, with varied diameter and spacing, evolving H<sub>2</sub> at J = 100-300 mA cm<sup>-2</sup>. These authors found that compared to a planar electrode, microstructured electrodes reduce the impact of gas bubbles on the ohmic drop but may increase the effect of concentration overpotentials. Recently Lee et al. used a E-E model to study the supersaturation and gas blockage occurring in a zero-gap AWE cell operating at  $J \le 2$  A cm<sup>-2</sup>. <sup>297</sup> The model predicted substantial concentration gradients across the electrode surface, with dissolved gas concentrations exceeding 1 M for low electrolyte flow rates, based on assumption that gas nuclei would not form until a critical concentration of dissolved gas was reached. Lower dissolved concentrations of gas may thus be expected to be observed at electrodes with pre-existing gas nuclei.7

Beyond the studies described above, a significant body of work has been performed modeling on the shapes and dynamics of confined bubbles, in the absence of an electrochemical driving force. These are frequently of interest in microfluidic systems, <sup>298</sup> but many of the physical processes are related to fluid flow in porous electrodes. We do not review these works here, but direct the reader to the review of this topic by Ajaev and Homsy as an introduction to the topic. <sup>299</sup> Despite the fact that gas bubbles in modern zero-gap AWE (Section 5.2.1) and PEMWE cells (Section 5.2.2) will primarily exert an influence on the voltage efficiency during

their motion through the three-phase solid/liquid/gas porous transport layer or catalyst layer, nearly all continuum models mentioned above have focused on two-phase flows within an interelectrode gap. Future work may incorporate gas generation and concentration gradients into models for confined bubble flow to more accurately predict current distributions across catalyst layers.

## 8. FUNCTIONAL MATERIALS FOR GAS TRANSPORT IN ELECTROLYZERS

#### 8.1. Controlling Electrode/Gas Interactions

Surface forces control the dynamic behavior of gas bubbles within electrolyzers. The equilibrium energy required to remove a gas bubble from a solid surface is described by  $W_a$ and thus one of the primary ways of controlling gas transport at a solid surface is by tuning the strength of interactions with the gas or liquid phase (eq 11). A wide variety of functional materials which either promote or inhibit the collection of gas bubbles at electrodes for H2 and O2 generation have been reported. Many of these materials have been inspired by designs that incorporate structural motifs observed in natural systems. 223,300-304 Generally, these designs can be separated into two categories: (1) electrodes which have been modified with hydrophobic or hydrophilic coatings to promote gas adhesion or facilitate gas release, or (2) electrodes with specific surface morphologies which control gas transport by reducing the departure diameter or allowing capillary transport of gases or liquids.

8.1.1. Modified Electrode Surfaces. Both metal and metal-oxide surfaces are generally hydrophilic when appropriately cleaned, 305,306 such that most efforts to change the modify the surface chemistry of electrodes lead to more hydrophobic surfaces. Active electrocatalysts must be in contact with reactant electrolyte and should not be directly covered with hydrophobic or hydrophilic materials unless they are permeable to ions and dissolved gas, but composite surfaces, prepared by modifying metal electrocatalysts with hydrophobic components, such as (poly)tetrafluoroethylene, have been used to draw bubbles away from active catalyst regions and control the departure diameter of gas bubbles. Teschke and Galembeck were perhaps the first to report that PTFE coatings could be used to control the collection of gases on perforated Ni sheets, because the hydrophobic surface led to the coalesce of larger gas bubbles on regions that were not

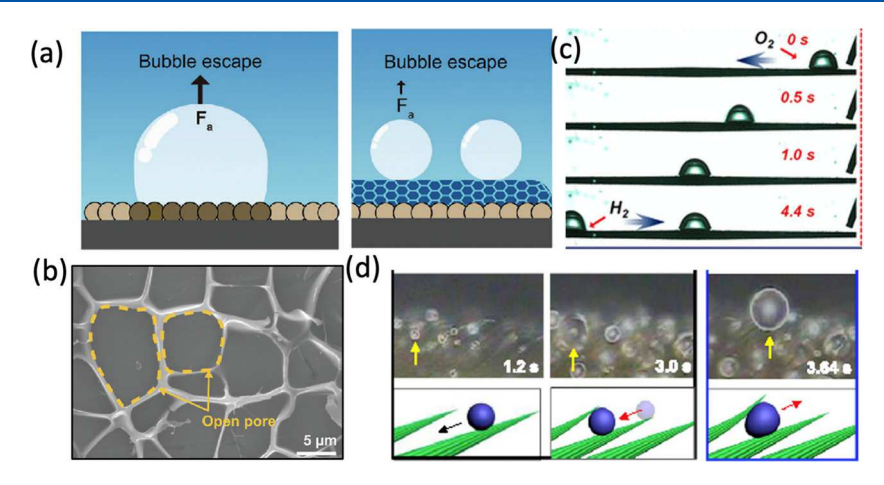


**Figure 21.** (a) Mechanism for gas removal via a "gel-like aerophobic surface system". Reproduced with permission from reference. <sup>315</sup> Copyright 2024 Elsevier. (b) Scanning electron microscope image of a hydrogel overlayer on a Pt cathode used for H<sub>2</sub> evolution. Reproduced with permission from reference. <sup>315</sup> Copyright 2024 Elsevier. (c) Optical images of directional gas transport of H<sub>2</sub> and O<sub>2</sub> bubbles on a micro/nanostructured cone of Cu. <sup>303</sup> (d) Optical images of bidirectional transport of water droplets on microfibers present on the legs of a water strider insect. <sup>317</sup>

responsible for ionic conduction. The same authors later reported that composite Ni/PTFE electrodes could be prepared by spray coating Ni electrodes with PTFE particles,  $10-100~\mu m$  in diameter, with a secondary coating of electrodeposited Ni providing mechanical integrity to the attached particles (Figure 20a). Despite the lower effective Ni surface area available for catalysis, electrodes modified with PTFE particles yielded lower overpotentials for the  $H_2$  compared to polished Ni surfaces and electrodes with the lowest coverage of PTFE yielded the largest reductions to the overpotential. Notably, the voltage was measured using the current-interrupt method, which avoids the influence of IR losses through the attached gas bubble film at the electrode surface.

A related work from Kleinke and Teschke used patterned reactive ion etching to prepare Ni electrodes decorated with high-aspect ratio PTFE columns which yielded even greater improvements to the onset overpotential for the HER in 30 wt % KOH compared to polished Ni surfaces (Figure 20b, d). 309

Heidrich and Müller performed a more extensive study of the influence of hydrophobic domains on gas-evolving electrodes using a highly active and wettable platinized Pt (Pt/Pt) electrode modified with hydrophobic PTFE islands, 0.5 mm in diameter (Figure 20c). The electrodes were tested in 0.5 M H<sub>2</sub>SO<sub>4</sub> for the HER and OER as well as the chlorine evolution reaction, CER, from 3 M KCl (at pH = 3), where patterned PTFE islands were shown to lead to lower electrode overpotentials for the two-electron HER and CER but led to marginal effects on the overpotential for the fourelectron OER (Figure 20e,f). Ho and Hwang observed lower OER overpotentials for PbO<sub>2</sub> anodes in 1 M H<sub>2</sub>SO<sub>4</sub> when codeposited with PTFE, but the polymer was found to also modify the morphology and electrochemically active surface area of the electrode. 311 Galvanostatic measurements by Heidrich supported claims that a reduced dissolved concentration of product gases at the electrocatalyst surface was responsible for the greater effective current toward H<sub>2</sub> and Cl<sub>2</sub> for PTFE-modified Pt/Pt surfaces. The observation that more substantial effects on overpotential were observed at increased temperature is consistent with an increased supersaturation of dissolved gases in heated electrolytes and/or an increase in the reversibility of the reaction kinetics.

Brussieux and Rakib used PTFE-modified Ni to control the size and coverage of gas bubbles on an electrode surface, finding that hydrophobic sites mostly serve as regions for coalescence of smaller nearby gas bubbles, with larger gas bubbles being able to persist for a greater period prior to release.312 Iwata and Wang studied the dynamics of gas bubbles within the internal volume of a porous PTFE-modified nickel foam evolving O<sub>2</sub> from 1 M KOH.<sup>211</sup> In contrast to results obtained for the HER in concentrated KOH, all quantities of PTFE coverage led to increased overpotentials for the OER, which was primarily attributed to increases in resistance both outside and within the internal volume of the porous nickel foam. This result is consistent with earlier observations by Muller that PTFE-modified electrodes are mostly effective at reducing concentration overpotentials for reversible gas-evolving reactions. 310

Gas-evolving electrodes modified with hydrophilic polymersare reported less frequently, as clean metal surfaces are already wetting surfaces. However, porous polymer layers with large opening have been found to lower the ohmic and concentration overpotentials at H2-evolving electrodes in acid and base. 313-315 Zhao et al., characterized the effect of increasing the hydrophilicity of a commercial, sintered Ti sheet PTL. 262 To do this, the researchers boiled the PTL in a mixture of ammonium hydroxide, hydrogen peroxide, and water for 10 min, which is similar to baths developed by the microelectronics industry for removing organic contamination, 316 but could also oxidize the metal surface. This converted the relatively hydrophilic "as received" PTL into a "superhydrophilic" layer which exhibited improved wickability. Ryu et al. first reported the use of a hydrogel overlayer on Pt electrodes effecting the HER in 0.50 M H<sub>2</sub>SO<sub>4</sub>, finding that the hydrogel coating led to increased bubble coverage but lower overpotentials (-0.18 V vs RHE at  $-10 \text{ mA cm}^{-2}$ ) compared to an uncoated Pt film  $(-0.20 \text{ V vs RHE at } -10 \text{ mA cm}^{-2})$ . 313 Later studies measured the effect of the hydrogel on Ni foams in 1.0 M KOH and on large area (100 cm<sup>2</sup>) modified Pt electrodes. 314,315 The hypothesized mechanism for improvement relative to bare catalyst surfaces is that the textured hydrophilic overlayer facilitates gas removal from active catalyst sites while maintaining a gas phase in the proximity of the catalyst surface. This simultaneously prevents the

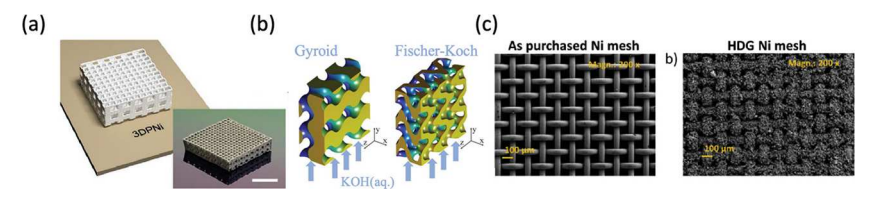


Figure 22. (a) Ni lattice structure prepared by additive manufacturing designed to facilitate ordered gas release. Reproduced with permission from reference. 146 Copyright 2019 John Wiley and Sons. (b) Triply periodic minimal surfaces which were prepared out of Ni using selective laser melting and used as electrodes for AWE. Reproduced with permission from reference. Copyright 2022 John Wiley and Sons. (c) Scanning electron micrograph images of a Ni mesh treated using hot dip galvanization and etching to produce a high surface area for improved catalysis and gas release. Reproduced with permission from reference. Copyright 2018 Elsevier.

accumulation of dissolved gases at the electrode interface without preventing diffusion of reactants and products to or from the electrode surface (Figure 21a,b).

**8.1.2.** Control of Catalyst Structure. Electrodes with nanostructured, wetting surfaces will provide increased area for electrocatalysis relative to a flat surface, while reducing the area for gas bubble adhesion, thus facilitating rapid gas release. Both effects are useful for increasing the operating current density of a water electrolyzer at a given voltage and this has been a commonly adopted strategy for controlling gas evolution behavior.

Many studies have explored the relationship between complex metal architectures and H<sub>2</sub> gas evolution behavior. Song used template-assisted printing to prepare superlattices of Pt nanoparticles which facilitated hydrogen gas release in 1.0 M NaOH and reduced gas adhesion in water compared to films of nanoparticles prepared via drop-casting. 318 Lake et al. characterized the gas-release behavior of microstructured platinum electrodes at  $J = 100-400 \text{ mA cm}^{-2} \text{ toward H}_2 \text{ in}$ 0.5 M H<sub>2</sub>SO<sub>4</sub>, finding that a reduction in the height of micropillars led to an increase in the activity normalized to electrochemically-active surface area. 319 The Jiang group has pioneered research on "superaerophobic" surfaces, with many structures inspired by features observed in nature. 300,301,317 A general design motif is hierarchical structure, with repeating features at both the microscale and nanoscale, which has been observed to lead to directional droplet transport on the legs of water striders (Figure 21d),317 hydrophobicity in lotus leaves,<sup>320</sup> rose petals,<sup>42</sup> and underwater ferns.<sup>41</sup> Lu and Jiang first reported superaerophobic properties of MoS2 electrocatalyst films for the HER in 0.50 M H<sub>2</sub>SO<sub>4</sub>, showing that vertically oriented nanosheets released bubbles at smaller diameters and also yielded lower overpotentials compared to flat films.<sup>321</sup> Li and Jiang extended this strategy to noble metals, showing that "pine-shaped" Pt surfaces led to smaller gas bubbles and a lower ohmic overvoltage at absolute current densities > 30 mA cm<sup>-2</sup> compared to flat films and Pt nanospheres.<sup>322</sup> Additional studies on aerophobic electrocatalyst coatings have yielded similar results on structured carbon supports, 323 alloys, 324 chalcogenides, 325 and phosphides,<sup>326</sup> driving the HER in acidic and alkaline electrolytes.

Oxygen evolution catalysts typically restructure into high surface area metal oxyhydroxides during operation and are thus highly wettable surfaces, absent further modifications to the surface roughness. Control of catalyst structure is nevertheless important for facilitating gas release and transport at high J (>1 A cm<sup>-2</sup>) and the structure of metal supports in anode catalyst layers for the OER in AWE and PEM electrolysis has been studied and the effects on mass-transport-related over-

potentials characterized in device environments (Section 5.2).  $^{137,146,220}$ 

#### 8.2. Directed Gas Transport

In an electrolyzer stack, directed flow of gas bubbles away from current-carrying pathways and toward flow channels is a practical barrier for maximizing the operating J. Thus, strategies for directional gas transport have been adopted in porous electrodes suitable for use in electrolysis cells. Gradients in the surface composition or structure may lead to a net driving force that directs the movement of bubbles.

Hine noted the importance of controlling the structure of perforated electrodes in advanced alkaline water electrolysis designs to prevent gas formation in current-conducting pathways. 47 These strategies have been demonstrated in practical systems, with many studies focused on the structure Ni and NiFe-based electrodes used for AWE. Wendt observed decreased overpotentials for roughened H2 electrodes but marginal improvements on roughened O2 electrodes, when tested for alkaline electrolysis in room temperature 50 wt % KOH(aq).<sup>327</sup> Hall et al. applied Ni and Ni-Fe alloy coatings with a high specific surface area to AWE electrodes, noting that H<sub>2</sub> and O<sub>2</sub> electrodes exhibited different trends in overpotential as a function of sintering; while this affect was attributed to differences in gas evolution it was not examined in detail.<sup>328</sup> Ahn and Jang studied the influence of morphology on gas release at Ni electrodes effecting the OER in 6.0 M KOH, finding that a needle-like morphology maximized wettability and also minimized the kinetic overpotential for oxygen evolution.329

Kou and Li used additive manufacturing techniques for electrode structuring, showing that 3D printed nickel electrodes with periodic structures suppress gas bubble coalescence, jamming, and trapping and, hence, result in rapid bubble release (Figure 22a). Lasers have been used to prepare porous electrodes for advanced alkaline electrolysis systems. Rocha and Proost conducted a systematic study on triply periodic minimal surfaces of Ni that were prepared via selective laser melting and used as electrodes for AWE (Figure 22b). 330 This study found that after controlling for porosity, geometries that channel the flow provide lower friction factors during electrolysis with forced convection. In a separate approach, Koj and Turek used subtractive laser ablation to prepare high surface area NiFe anodes that facilitated gas release and reduced the OER overvoltage in room-temperature 32.5 wt % KOH by 43 mV at 10 mA cm<sup>-2</sup>.331 Mayrhofer et al. used a subtractive method to prepare highly porous Ni alloys, by performing hot dip galvanization of a porous Ni electrode and then etching the NiZn alloy; these electrodes facilitated gas release at current densities up to 2 A cm<sup>-2</sup> (Figure 22c).<sup>332</sup> Liu and Wang prepared mesoporous carbon supports using

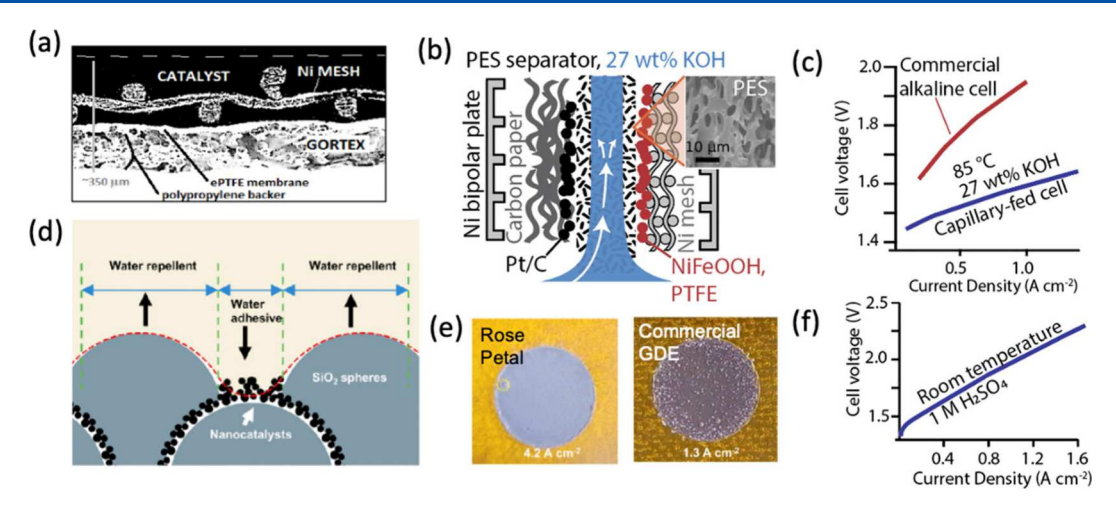


Figure 23. (a) Design for a bubble-free electrolyzer, using a Goretex PTFE membrane-supported electrode. Reproduced with permission from reference. Copyright 2019 Elsevier. (b) Scheme for a capillary-fed bubble-free electrolyzer, using a PES separator shown in the inset scanning electron micrograph (adapted from Hodges et al. under Creative Commons Attribution International License 4.0)<sup>222</sup> (c) Performance of a capillary fed electrolyzer compared to a conventional AWE. (d) Rose-petal electrode design with alternating hydrophobic and hydrophilic domains controlling gas release. Reproduced with permission from reference. Copyright 2023 Elsevier. (e) Optical image comparison of the gas evolution behavior of a conventional gas diffusion electrode ( $J = 1.3 \text{ A cm}^{-2}$ ) to a rose-petal electrode ( $J = 4.2 \text{ A cm}^{-2}$ ) showing reduced bubble generation. Reproduced with permission from reference. Copyright 2023 Elsevier. (f) Cell performance of a membrane-free electrolyzer with a narrow channel filled with room temperature 1 M H<sub>2</sub>SO<sub>4</sub>, showing stable, bubble-free operation at  $J > 1 \text{ A cm}^{-2}$ .

surfactant-templated assembly of block copolymers followed by carbonization and functionalization with Pt and Ru catalysts; improved performance was measured for <5 nm pores but discrimination between dissolved  $\rm H_2$  and nanosized  $\rm H_2$  bubbles was not reported. 333

The Jiang group has developed new functional surfaces that drive directional transport of attached gas bubbles, showing that Cu and polyethylene surfaces can assist bubbles in overcoming buoyant forces (Figure 22c).302,334 Three electrode measurements of individual H2 and O2 electrodes have demonstrated basic strategies for directing gas transport: Zhang and Yu demonstrated directional transport of gas bubbles along a metallic copper cone,<sup>335</sup> Winther-Jensen first reported the use of PTFE membranes functionalized with maleic anhydride and sputtered sequentially with Au and Pt layers to create a breathable electrode structure.<sup>336</sup> Later, Li and Cui reported a similar electrocatalyst fabrication by sputtering polyethene membranes with Au and coating with NiFeO<sub>x</sub> via electrodeposition.<sup>337</sup> This method produced electrodes with very low overpotentials toward the OER and a similar electrode coated with an Ag/Pt catalyst layer was used to catalyze the oxygen reduction reaction. Tiwari developed PTFE-membrane based electrolyzers with thicker hydrophilic catalyst layers than originally reported by Winther-Jensen, 221 inspired by a 1987 patent for chlor-alkali electrodes which produced gas bubbles away from current-carrying pathways.<sup>338</sup> The previous design reported an electrode coated with a nonconductive refractory oxide which would suppress the nucleation and growth of bubbles, and this was adapted to AWE cells by compressing a mixture of PTFE and catalyst particles between a PTFE membrane and a fine nickel mesh. Cells assembled on either side of a liquid electrolyte layer yielded bubble free electrolysis at *I* up to 300 mA cm<sup>-2</sup> (Figure 23a).

Hodges et al. recently reported an improved designthat obviated the need for an interelectrode flow channel and could be fed passively by capillary action. These capillary-fed cells could eliminate the need for expensive gas—liquid separators

and pumps for recirculating electrolyte, and potentially reduce shunt currents which reduce the system efficiency. Microporous polyether sulfone membranes were selected and sandwiched between a fine Ni mesh coated in NiFeOOH catalyst and a carbon paper GDE coated with Pt/C (Figure 23b). Significantly lower cell voltages were observed in the absence of bubbles and these voltages were further improved by incorporating PTFE into the anode layer, thus preventing the porous anode catalyst layer from filling with electrolyte.  $J \leq 1 \text{ A cm}^{-2}$  were sustained with less than 0.15%vol H<sub>2</sub> detected in the O<sub>2</sub> stream produced by the anode (Figure 23c), although the measured trend in crossover rates deviated from typical models used to predict crossover in traditional AWE designs, possibly a result of undesired bubble formation.

Deng et al. used an electrode morphology inspired by hydrophobic rose petal surfaces in a membraneless electrolyzer operating at  $J=4~\rm A~cm^{-2}$  in 1 M  $\rm H_2SO_4$  and  $J=1.5~\rm A~cm^{-2}$  in 1 M NaOH (Figure 23f). <sup>223</sup> SiO<sub>2</sub> microspheres were modified with siloxane to present a hydrophobic surface, and selective coating with catalyst particles in the interstitial voids produced a surface with alternating hydrophobic and hydrophilic regions (Figure 23d,e). The wetting properties of the electrode were stable for 6 h of continuous electrolysis but bubble formation began to occur in the following 4 h indicating that a more robust implementation of this strategy is needed for practical use. The next challenge for bubble-free electrolysis is to demonstrate these approaches on large-area electrodes and/or in a stack configuration relevant to industrial production of electrolytic  $\rm H_2$ .

#### 9. OUTLOOK

Research on gas evolution extends to the earliest days of water electrolysis and modern electroanalytical methods have yielded a detailed understanding of the physical processes controlling gas evolution and the impacts of gas bubbles on the efficiency of water electrolyzers. The development of nanoelectrodes have allowed researchers to measure the influence of individual gas bubbles from nucleation to detachment while *in situ* and

operando characterization techniques using optical and X-ray imaging have resolved complex multiphase flows within porous electrodes at industrially relevant current densities. Much is now understood about bulk two-phase flows in porous electrodes, which can be analyzed with nonperturbative methods (Table 1). However, the perturbative nature and specialized cell-designs for electron-microscopy means that the earliest stages of gas evolution (nucleation and growth at nanometer scale) remain poorly characterized in device environments. Studying the distribution and growth rate of gas nuclei formed within catalyst layers could provide much needed insights into the hypothesized role of bubbles in delamination-related failure of catalyst coatings.

Efforts to control and direct gas evolution within water electrolyzers have led to devices which produce H<sub>2</sub> at increased throughput relative to early electrolyzer designs. Zero-gap architectures mitigate the influence of gas bubbles on cell resistance, but gas accumulation within porous transport layers leads to critical current densities which limit the ultimate throughput of electrolysis.<sup>230</sup> Recently developed functional materials and composite electrodes facilitate directional gas transport; these materials have electrolyzers operating in liquid electrolyte with increased efficiency and throughput while using diaphragm separators instead of polymer membranes (which could potentially lower the cost of future electrolyzers). 222,223 To date, gas bubbles have not been a major source of voltage inefficiency for membrane electrolyzers, but gas management may become more important for electrolyzers using reduced loadings of Ir catalyst (leading to increased local current densities).<sup>23</sup>

Despite well over a century of investigations into the behavior of gas-evolving electrodes, there are many questions which invite further investigation by future researchers: (1) we still do not know the true shape and contact angle of individual gas bubbles throughout their lifetime on polarized electrode surfaces, which has important implications for catalyst coverage and detachment diameters; (2) for gas films at surfaces, within porous electrodes, and rising near electrode surfaces, we lack a detailed understanding of the molecular factors controlling coalescence; (3) many studies have characterized nucleation and growth phenomena for electrochemically generated H<sub>2</sub> and O2, but only a few studies of individual gas bubbles have been carried out at elevated temperatures and in the concentrated alkaline electrolytes used in commercial AWE cells; 212,213 (4) although Marangoni convection has long been understood to be crucial for mass transfer and force balances at a gas-covered electrode, 60 the relative influence of various temperature and concentration gradients is debated; 40,51,54,98 (5) most experimental studies on Marangoni convection have focused on micron-scale electrode sites which operate at higher current densities than typical electrolyzers operating in liquid electrolyte ( $I \le 2 \text{ A cm}^{-2}$ ); the ways in which neighboring Marangoni flows interact and the relationship to coalescence is a nascent area of study. 101 Moreover, these sources of microconvection have rarely been included in continuum level models for gas evolution.

Measurements of the above phenomena related to electrochemical gas evolution will lead to improved models for water electrolysis and potentially lead to more scalable pathways for producing hydrogen. Today's models for small electrodes still incorporate a subset of the relevant forces needed to understand growth and detachment models for large area electrodes have only recently begun to include effects related to distributions of gas bubble diameters. The influence of realistic surface features, such as roughness and pre-existing gas nuclei, on the gas coverage at a large area electrode has important implications for device design but is challenging to model at either the molecular level or continuum level. Once again, we note that continuum-level models of multiphase flows in porous electrodes are needed to more accurately predict current distributions across catalyst layers and these results could have important implications for predicting device efficiency and degradation rates in both AWE and PEMWE cells.

#### **AUTHOR INFORMATION**

#### **Corresponding Author**

Paul A. Kempler – Department of Chemistry and Biochemistry, University of Oregon, Eugene, Oregon 97403, United States; Oregon Center for Electrochemistry, University of Oregon, Eugene, Oregon 97403, United States; orcid.org/0000-0003-3909-1790; Email: pkempler@uoregon.edu

#### **Authors**

Robert H. Coridan — Department of Chemistry and
Biochemistry, University of Arkansas, Fayetteville, Arkansas
72701, United States; orcid.org/0000-0003-1916-4446
Long Luo — Department of Chemistry, Wayne State
University, Detroit, Michigan 48202, United States;
Department of Chemistry, University of Utah, Salt Lake,
Utah 84112, United States; orcid.org/0000-0001-5771-6892

Complete contact information is available at: https://pubs.acs.org/10.1021/acs.chemrev.4c00211

#### **Author Contributions**

CRediT: Paul Andrew Kempler conceptualization, writing - original draft, writing - review & editing; Robert H. Coridan conceptualization, writing - original draft, writing - review & editing; Long Luo conceptualization, writing - original draft, writing - review & editing.

#### **Notes**

The authors declare the following competing financial interest(s): PAK has received funding from and is an adviser to Hgen, a company developing alkaline water electrolyzers.

#### **Biographies**

Paul Kempler majored in Chemistry and Chemical Engineering at Vanderbilt University, where he received his B.E. in 2015. He received a Ph.D. in Chemical Engineering from the California Institute of Technology in 2020, where he studied microstructured semiconductors and electrocatalysts for photoelectrochemical devices under the supervision of Prof. Nathan S. Lewis. He joined the University of Oregon faculty in 2020 as a Research Assistant Professor and the Associate Director for the Oregon Center for Electrochemistry. At Oregon he has developed an integrated set of laboratory courses for an industry-focused master's program in electrochemistry and managed a network of industry partners in the energy storage and electrolysis sectors. In 2024, he joined the tenure-track faculty in the Department of Chemistry and Biochemistry as an Assistant Professor. The Kempler Group investigates chemical processes for electrified manufacturing, including hydrogen production, iron electrowinning, and long-duration energy storage.

Rob Coridan completed his Ph.D. in Physics under the supervision of Prof. Gerard C.L. Wong at the University of Illinois, Urbana-Champaign in 2009. There he studied x-ray and soft condensed matter physics related to biological self-assembly and the ultrafast dynamics of hydration. He had a brief appointment as a postdoctoral researcher with Prof. Wong's group after it moved to the University of California, Los Angeles in 2009. He then moved to the California Institute of Technology to work as a postdoctoral scholar in Prof. Nathan S. Lewis's group at from 2010-2015. In 2015, he started his independent career as an Assistant Professor of Chemistry and Biochemistry at the University of Arkansas in Fayetteville, AR. He is currently a Professor of Chemistry and Biochemistry at the University of Arkansas and a faculty member of the Materials Science and Engineering Program. The Coridan research group works at the interface of photoelectrochemistry, electrocatalysis, and soft matter with the aim to develop multifunctional composite materials for solarto-fuels and photonic applications.

Long Luo received his B.S. (2009) in applied chemistry from the Beijing University of Aeronautics and Astronautics and his Ph.D. (2014) in chemistry from the University of Utah under the guidance of Prof. Henry S. White. Then, he worked as a postdoctoral fellow in the laboratory of Prof. Richard M. Crooks at the University of Texas at Austin. He started his independent career at Wayne State University in 2017 and spent seven years there before joining the University of Utah in 2024. He received the Alfred P. Sloan Research Fellowship, National Science Foundation CAREER Award, NIH Maximizing Investigators' Research Award (MIRA), the Royce W. Murray Young Investigator Award from the Society for Electroanalytical Chemistry, and Wayne State University Academy of Scholars Junior Faculty Award. He was selected as a Scialog Fellow, Chem Comm Emerging investigators, Anal. Bioanal. Chem. Young Investigators, Nanoscale Emerging Investigators, and a Langmuir inaugural Early Career Advisory Board Member. He also joined the Editorial Advisory Board of ACS Electrochemistry and the Journal of Electrochemistry. The research goal of his laboratory is to address the grand challenges of our times in environment, energy, and health by designing, discovering, synthesizing, and utilizing new functional materials and molecules and by developing novel analytical methods, tools, and devices.

#### **ACKNOWLEDGMENTS**

We gratefully acknowledge Martin Edwards and Hamed Mehrabi for their support in the preparation of this manuscript. We also thank our reviewers for their constructive feedback and suggestions during the review process. PAK acknowledges support from the Oregon Center for Electrochemistry. LL acknowledges the support from the National Science Foundation under award CHE-1943737. RHC acknowledges that this material is based upon work supported by the U.S. Department of Energy, Office of Science, Office of Basic Energy Sciences under Award Number DE-SC-0020301.

#### **GLOSSARY OF SYMBOLS AND ABBREVIATIONS**

A Maximum	available	catalyst	surface area	
-----------	-----------	----------	--------------	--

 $A_h$  Effective catalyst area after considering gas coverage

AFM Atomic force microscopy AWE Alkaline water electrolysis  $\alpha$  Transfer coefficient

b Tafel slope
 c Concentration
 c\* Bulk concentration
 CE Counter electrode

CT	Computed tomography
D	Diffusion coefficient

 $\delta$  diffusion boundary layer thickness

 $egin{array}{ll} E & & \mbox{Potential} \ F_{
m b} & \mbox{Buoyant force} \ F & \mbox{Faraday's constant} \ \end{array}$ 

f Volume fraction of particles in a medium

 $\Delta G$  Change in Gibbs free energy

GDL Gas diffusion layer γ Activity coefficient

γ Surface energy/surface tension HER Hydrogen evolution reaction

h Solution depth η Overpotential

 $\eta_c$  Concentration overpotential  $\eta_h$  Hyperpolarization overpotential

i CurrentJ Molar flux

J Total applied current density

 $K_e$  Effective conductivity  $K_c$  Bulk electrolyte conductivity

MD Molecular dynamics

 $\mu$ CT Micro computed tomography  $\nu$  Stochiometric coefficient  $\hat{\underline{n}}$  Unit normal vector

P Pressure

PEM Proton exchange membrane electrolysis

PTL Porous transport layer R Universal gas constant

r Radius

RE Reference electrode ρ Density of solution S Supersaturation factor

SECM Scanning electrochemical microscopy SECCM Scanning electrochemical cell microscopy

T Temperaturet Time

TEM Transmission electron microscopy

 $\theta$  Contact angle V Cell potential

 $V_{\rm b}$  Volume of gas bubble

 $egin{array}{ll} {f v} & {f Fluid velocity} \ W_a & {f Work of adhesion} \ {f WE} & {f Working electrode} \ \end{array}$ 

Number of electrons involved in a charge transfer

reaction

#### REFERENCES

- (1) Lim, J.; Fernández, C. A.; Lee, S. W.; Hatzell, M. C. Ammonia and Nitric Acid Demands for Fertilizer Use in 2050. ACS Energy Lett. 2021, 6, 3676–3685.
- (2) Suzuki, T.; Iiyama, A.; Kubo, N.; Saito, N.; Shinohara, K.; Shimotori, S.; Sugawara, Y.; Yamada, K. Toward the Future Fuel Cell-Challenge for 2040. *ECS Trans.* **2019**, *92*, 3.
- (3) Ruggles, T. H.; Dowling, J. A.; Lewis, N. S.; Caldeira, K. Opportunities for Flexible Electricity Loads Such as Hydrogen Production from Curtailed Generation. *Adv. Appl. Energy* **2021**, *3*, 100051.
- (4) Dowling, J. A.; Rinaldi, K. Z.; Ruggles, T. H.; Davis, S. J.; Yuan, M.; Tong, F.; Lewis, N. S.; Caldeira, K. Role of Long-Duration Energy Storage in Variable Renewable Electricity Systems. *Joule* **2020**, *4*, 1907–1928.

- (5) Ricks, W.; Xu, Q.; Jenkins, J. D. Minimizing Emissions from Grid-Based Hydrogen Production in the United States. *Environ. Res. Lett.* **2023**, *18*, 014025.
- (6) Badgett, A.; Ruth, M.; James, B.; Pivovar, B. Methods Identifying Cost Reduction Potential for Water Electrolysis Systems. *Curr. Op. Chem. Eng.* **2021**, 33, 100714.
- (7) IRENA. Green Hydrogen Cost Reduction; IRENA, 2020. https://www.irena.org/Publications/2020/Dec/Green-hydrogen-cost-reduction (accessed 2023-05-24).
- (8) Todoroki, N.; Nagasawa, K.; Enjoji, H.; Mitsushima, S. Suppression of Catalyst Layer Detachment by Interfacial Microstructural Modulation of the NiCo<sub>2</sub>O<sub>4</sub>/Ni Oxygen Evolution Electrode for Renewable Energy-Powered Alkaline Water Electrolysis. *ACS Appl. Mater. Interfaces* **2023**, *15*, 24399–24407.
- (9) Leistra, J. A.; Sides, P. J. Voltage Components at Gas Evolving Electrodes. J. Electrochem. Soc. 1987, 134, 2442.
- (10) Angulo, A.; van der Linde, P.; Gardeniers, H.; Modestino, M.; Fernandez Rivas, D. Influence of Bubbles on the Energy Conversion Efficiency of Electrochemical Reactors. *Joule* **2020**, *4*, 555–579.
- (11) Sides, P. J. Phenomena and Effects of Electrolytic Gas Evolution. In *Modern Aspects of Electrochemistry*; White, R. E., Bockris, J. O., Conway, B. E., Eds.; Modern Aspects of Electrochemistry; Springer US: Boston, MA, 1986; Vol. 18, pp 303–354.
- (12) Lubetkin, S. D. The Fundamentals of Bubble Evolution. *Chem. Soc. Rev.* **1995**, 24, 243–250.
- (13) Zhao, X.; Ren, H.; Luo, L. Gas Bubbles in Electrochemical Gas Evolution Reactions. *Langmuir* **2019**, *35*, 5392–5408.
- (14) Lohse, D.; Zhang, X. Surface Nanobubbles and Nanodroplets. *Rev. Mod. Phys.* **2015**, *87*, 981–1035.
- (15) Swiegers, G. F.; Terrett, R. N. L.; Tsekouras, G.; Tsuzuki, T.; Pace, R. J.; Stranger, R. The Prospects of Developing a Highly Energy-Efficient Water Electrolyser by Eliminating or Mitigating Bubble Effects. Sustainable Energy Fuels 2021, 5, 1280–1310.
- (16) Li, M.; Xie, P.; Yu, L.; Luo, L.; Sun, X. Bubble Engineering on Micro-/Nanostructured Electrodes for Water Splitting. *ACS Nano* **2023**, *17*, 23299–23316.
- (17) Shih, A. J.; Monteiro, M. C.; Dattila, F.; Pavesi, D.; Philips, M.; da Silva, A. H.; Vos, R. E.; Ojha, K.; Park, S.; van der Heijden, O.; et al. Water Electrolysis. *Nat. Rev. Methods Primers* **2022**, *2*, 84.
- (18) Carmo, M.; Fritz, D. L.; Mergel, J.; Stolten, D. A Comprehensive Review on PEM Water Electrolysis. *Int. J. Hydrogen Energy* **2013**, 38, 4901–4934.
- (19) Buttler, A.; Spliethoff, H. Current Status of Water Electrolysis for Energy Storage, Grid Balancing and Sector Coupling via Power-to-Gas and Power-to-Liquids: A Review. *Renew. Sustainable Energy Rev.* **2018**, 82, 2440–2454.
- (20) Caspari, W. A. Über Elektrolytische Gasentwickelung. Z. Phys. Chem. 1899, 30, 89–97.
- (21) He, W.; Nguyen, T. V. Edge Effects on Reference Electrode Measurements in PEM Fuel Cells. J. Electrochem. Soc. 2004, 151, A185.
- (22) Xu, Q.; Oener, S. Z.; Lindquist, G.; Jiang, H.; Li, C.; Boettcher, S. W. Integrated Reference Electrodes in Anion-Exchange-Membrane Electrolyzers: Impact of Stainless-Steel Gas-Diffusion Layers and Internal Mechanical Pressure. ACS Energy Lett. 2021, 6, 305–312.
- (23) Gileadi, E. Electrode Kinetics for Chemists, Chemical Engineers, and Materials Scientists; VCH Publishers Inc., 1993.
- (24) Vogt, H. Gas-Evolving Electrodes. In Comprehensive Treatise of Electrochemistry: Electrodics: Transport; Yeager, E., Bockris, J. O., Conway, B. E., Sarangapani, S., Eds.; Comprehensive Treatise of Electrochemistry; Springer US: Boston, MA, 1983; pp 445–489.
- (25) Vogt, H. The Rate of Gas Evolution of Electrodes—I. An Estimate of the Efficiency of Gas Evolution from the Supersaturation of Electrolyte Adjacent to a Gas-Evolving Electrode. *Electrochim. Acta* **1984**, 29, 167–173.
- (26) McCrory, C. C. L.; Jung, S.; Ferrer, I. M.; Chatman, S. M.; Peters, J. C.; Jaramillo, T. F. Benchmarking Hydrogen Evolving Reaction and Oxygen Evolving Reaction Electrocatalysts for Solar Water Splitting Devices. *J. Am. Chem. Soc.* **2015**, *137*, 4347–4357.

- (27) Justi, E. W. Seventy Years Fuel Cell Research. Br. J. Appl. Phys. 1963, 14, 840.
- (28) Lohse, D. Bubble Puzzles: From Fundamentals to Applications. *Phys. Rev. Fluids* **2018**, *3*, 110504.
- (29) German, S. R.; Edwards, M. A.; Chen, Q.; Liu, Y.; Luo, L.; White, H. S. Electrochemistry of Single Nanobubbles. Estimating the Critical Size of Bubble-Forming Nuclei for Gas-Evolving Electrode Reactions. *Faraday Discuss.* **2016**, *193*, 223–240.
- (30) Edwards, M. A.; White, H. S.; Ren, H. Voltammetric Determination of the Stochastic Formation Rate and Geometry of Individual H<sub>2</sub>, N<sub>2</sub>, and O<sub>2</sub> Bubble Nuclei. ACS Nano **2019**, 13, 6330.
- (31) Williamson, F. R. Compilation and Evaluation of Available Data on Phase Equilibria of Natural and Synthetic Gas Mixtures; NBSIR; National Institute of Standards and Technology (NIST), Commerce Department, 1983.
- (32) Wiebe, R.; Gaddy, V. L.; Heinss, H. J. Solubility of Hydrogen in Water at 25 Degrees C from 25 to 1000 atm. *Ind. Eng. Chem.* 1932, 24. 823–825.
- (33) Shoor, S. K.; Walker, R. D.; Gubbins, K. E. Salting out of Nonpolar Gases in Aqueous Potassium Hydroxide Solutions. *J. Phys. Chem.* **1969**, 73, 312–317.
- (34) Schumpe, A. The Estimation of Gas Solubilities in Salt Solutions. *Chem. Eng. Sci.* **1993**, *48*, 153–158.
- (35) Dill, K.; Bromberg, S. Molecular Driving Forces: Statistical Thermodynamics in Biology, Chemistry, Physics, and Nanoscience, 2nd ed.; Garland Science: New York, 2010.
- (36) Atkins, P.; De Paula, J.; Keeler, J. Atkins' Physical Chemistry; Oxford University Press, 2023.
- (37) German, S. R.; Edwards, M. A.; Ren, H.; White, H. S. Critical Nuclei Size, Rate, and Activation Energy of H<sub>2</sub> Gas Nucleation. *J. Am. Chem. Soc.* **2018**, *140*, 4047–4053.
- (38) Pease, D. C. The Significance of the Contact Angle in Relation to the Solid Surface. *J. Phys. Chem.* **1945**, *49*, 107–110.
- (39) Gao, L.; McCarthy, T. J. How Wenzel and Cassie Were Wrong. Langmuir 2007, 23, 3762–3765.
- (40) Zhang, H.; Ma, Y.; Huang, M.; Mutschke, G.; Zhang, X. Solutal Marangoni Force Controls Lateral Motion of Electrolytic Gas Bubbles. *Soft Matter* **2024**, *20*, 3097–3106.
- (41) Barthlott, W.; Schimmel, T.; Wiersch, S.; Koch, K.; Brede, M.; Barczewski, M.; Walheim, S.; Weis, A.; Kaltenmaier, A.; Leder, A.; Bohn, H. F. The Salvinia Paradox: Superhydrophobic Surfaces with Hydrophilic Pins for Air Retention Under Water. *Adv. Mater.* **2010**, 22, 2325–2328.
- (42) Wang, J.; Yang, Q.; Wang, M.; Wang, C.; Jiang, L. Rose Petals with a Novel and Steady Air Bubble Pinning Effect in Aqueous Media. *Soft Matter* **2012**, *8*, 2261–2266.
- (43) Akay, Ö.; Bashkatov, A.; Coy, E.; Eckert, K.; Einarsrud, K. E.; Friedrich, A.; Kimmel, B.; Loos, S.; Mutschke, G.; Röntzsch, L.; Symes, M. D.; Yang, X.; Brinkert, K. Electrolysis in Reduced Gravitational Environments: Current Research Perspectives and Future Applications. *npj Microgravity* 2022, 8, 1–11.
- (44) Vogt, H. A Hydrodynamic Model for the Ohmic Interelectrode Resistance of Cells with Vertical Gas Evolving Electrodes. *Electrochim. Acta* **1981**, *26*, 1311–1317.
- (45) Hine, F.; Yasuda, M.; Nakamura, R.; Noda, T. Hydrodynamic Studies of Bubble Effects on the IR-Drops in a Vertical Rectangular Cell. *J. Electrochem. Soc.* **1975**, 122, 1185.
- (46) Vogt, H. Mass Transfer at Gas Evolving Electrodes with Superposition of Hydrodynamic Flow. *Electrochim. Acta* **1978**, 23, 203–205.
- (47) Hine, F.; Yasuda, M.; Ogata, Y.; Hara, K. Hydrodynamic Studies on a Vertical Electrolyzer with Gas Evolution under Forced Circulation. *J. Electrochem. Soc.* **1984**, *131*, 83.
- (48) Baczyzmalski, D.; Karnbach, F.; Yang, X.; Mutschke, G.; Uhlemann, M.; Eckert, K.; Cierpka, C. On the Electrolyte Convection around a Hydrogen Bubble Evolving at a Microelectrode under the Influence of a Magnetic Field. *J. Electrochem. Soc.* **2016**, *163*, No. E248.

- (49) Liu, H.; Pan, L.; Huang, H.; Qin, Q.; Li, P.; Wen, J. Hydrogen Bubble Growth at Micro-Electrode under Magnetic Field. *J. Electroanal. Chem.* **2015**, 754, 22–29.
- (50) Li, S.-D.; Wang, C.-C.; Chen, C.-Y. Water Electrolysis in the Presence of an Ultrasonic Field. *Electrochim. Acta* **2009**, *54*, 3877–3883.
- (51) Park, S.; Liu, L.; Demirkir, Ç.; van der Heijden, O.; Lohse, D.; Krug, D.; Koper, M. T. M. Solutal Marangoni Effect Determines Bubble Dynamics during Electrocatalytic Hydrogen Evolution. *Nat. Chem.* **2023**, *15*, 1532–1540.
- (52) Hossain, S. S.; Bashkatov, A.; Yang, X.; Mutschke, G.; Eckert, K. Force Balance of Hydrogen Bubbles Growing and Oscillating on a Microelectrode. *Phys. Rev. E* **2022**, *106*, 035105.
- (53) Yang, X.; Baczyzmalski, D.; Cierpka, C.; Mutschke, G.; Eckert, K. Marangoni Convection at Electrogenerated Hydrogen Bubbles. *Phys. Chem. Phys.* **2018**, 20, 11542–11548.
- (54) Guelcher, S. A.; Solomentsev, Y. E.; Sides, P. J.; Anderson, J. L. Thermocapillary Phenomena and Bubble Coalescence during Electrolytic Gas Evolution. *J. Electrochem. Soc.* **1998**, *145*, 1848.
- (55) Block, M. J. Surface Tension as the Cause of Bénard Cells and Surface Deformation in a Liquid Film. *Nature* **1956**, *178*, 650–651.
- (56) Pearson, J. R. A. On Convection Cells Induced by Surface Tension. J. Fluid Mech. 1958, 4, 489–500.
- (57) Westerheide, D. E.; Westwater, J. Isothermal Growth of Hydrogen Bubbles during Electrolysis. *AIChE J.* **1961**, *7*, 357–362.
- (58) Sides, P. J.; Tobias, C. W. A Close View of Gas Evolution from the Back Side of a Transparent Electrode. *J. Electrochem. Soc.* **1985**, 132, 583.
- (59) Janssen, L. J. J.; Hoogland, J. G. The Effect of Electrolytically Evolved Gas Bubbles on the Thickness of the Diffusion Layer. *Electrochim. Acta* 1970, 15, 1013–1023.
- (60) Lubetkin, S. The Motion of Electrolytic Gas Bubbles Near Electrodes. *Electrochim. Acta* **2002**, *48*, 357–375.
- (61) Brandon, N. P.; Kelsall, G. H.; Levine, S.; Smith, A. L. Interfacial Electrical Properties of Electrogenerated Bubbles. *J. Appl. Electrochem.* **1985**, *15*, 485–493.
- (62) Fernández, D.; Maurer, P.; Martine, M.; Coey, J. M. D.; Möbius, M. E. Bubble Formation at a Gas-Evolving Microelectrode. *Langmuir* **2014**, *30*, 13065–13074.
- (63) Van Der Linde, P.; Moreno Soto, Á.; Peñas-López, P.; Rodríguez-Rodríguez, J.; Lohse, D.; Gardeniers, H.; Van Der Meer, D.; Fernández Rivas, D. Electrolysis-Driven and Pressure-Controlled Diffusive Growth of Successive Bubbles on Microstructured Surfaces. *Langmuir* 2017, 33, 12873–12886.
- (64) Ford, I. J. Nucleation Theorems, the Statistical Mechanics of Molecular Clusters, and a Revision of Classical Nucleation Theory. *Phys. Rev. E* **1997**, *56*, 5615–5629.
- (65) Kalikmanov, V. I. Nucleation Theory; Lecture Notes in Physics; Springer Netherlands: Dordrecht, 2013; Vol. 860.
- (66) Wendt, H.; Imarisio, G. Nine Years of Research and Development on Advanced Water Electrolysis. A Review of the Research Programme of the Commission of the European Communities. J. Appl. Electrochem. 1988, 18, 1–14.
- (67) Chatzichristodoulou, C.; Allebrod, F.; Mogensen, M. B. High Temperature Alkaline Electrolysis Cells with Metal Foam Based Gas Diffusion Electrodes. *J. Electrochem. Soc.* **2016**, *163*, F3036.
- (68) Bernt, M.; Schröter, J.; Möckl, M.; Gasteiger, H. A. Analysis of Gas Permeation Phenomena in a PEM Water Electrolyzer Operated at High Pressure and High Current Density. *J. Electrochem. Soc.* **2020**, *167*, 124502.
- (69) Perez Sirkin, Y. A.; Gadea, E. D.; Scherlis, D. A.; Molinero, V. Mechanisms of Nucleation and Stationary States of Electrochemically Generated Nanobubbles. *J. Am. Chem. Soc.* **2019**, *141*, 10801–10811.
- (70) Gadea, E. D.; Molinero, V.; Scherlis, D. A. Nanobubble Stability and Formation on Solid-Liquid Interfaces in Open Environments. *Nano Lett.* **2023**, *23*, 7206–7212.
- (71) Jones, S. F.; Evans, G. M.; Galvin, K. P. Bubble Nucleation from Gas Cavities a Review. *Adv. Colloid Interface Sci.* **1999**, *80*, 27–50.

- (72) Liu, Y.; Edwards, M. A.; German, S. R.; Chen, Q.; White, H. S. The Dynamic Steady State of an Electrochemically Generated Nanobubble. *Langmuir* **2017**, *33*, 1845–1853.
- (73) Faber, M. S.; Dziedzic, R.; Lukowski, M. A.; Kaiser, N. S.; Ding, Q.; Jin, S. High-Performance Electrocatalysis Using Metallic Cobalt Pyrite (CoS<sub>2</sub>) Micro- and Nanostructures. *J. Am. Chem. Soc.* **2014**, 136, 10053–10061.
- (74) Han, B.; Stoerzinger, K. A.; Tileli, V.; Gamalski, A. D.; Stach, E. A.; Shao-Horn, Y. Nanoscale Structural Oscillations in Perovskite Oxides Induced by Oxygen Evolution. *Nat. Mater.* **2017**, *16*, 121–126.
- (75) Bashkatov, A.; Babich, A.; Hossain, S. S.; Yang, X.; Mutschke, G.; Eckert, K. H<sub>2</sub> Bubble Motion Reversals during Water Electrolysis. *J. Fluid Mech.* **2023**, 958, A43.
- (76) van der Linde, P.; Penas-Lopez, P.; Moreno Soto, A.; van der Meer, D.; Lohse, D.; Gardeniers, H.; Fernandez Rivas, D. Gas Bubble Evolution on Microstructured Silicon Substrates. *Energy Environ. Sci.* **2018**, *11*, 3452–3462.
- (77) Iwata, R.; Zhang, L.; Lu, Z.; Gong, S.; Du, J.; Wang, E. N. How Coalescing Bubbles Depart from a Wall. *Langmuir* **2022**, *38*, 4371–4377
- (78) Zhao, P.; Hu, Z.; Cheng, P.; Huang, R.; Gong, S. Coalescence-Induced Bubble Departure: Effects of Dynamic Contact Angles. *Langmuir* **2022**, *38*, 10558–10567.
- (79) Stover, R. L.; Tobias, C. W.; Denn, M. M. Bubble Coalescence Dynamics. *AIChE J.* **1997**, *43*, 2385–2392.
- (80) Bournival, G.; Ata, S.; Karakashev, S. I.; Jameson, G. J. An Investigation of Bubble Coalescence and Post-Rupture Oscillation in Non-Ionic Surfactant Solutions Using High-Speed Cinematography. *J. Colloid Interface Sci.* **2014**, *414*, 50–58.
- (81) Moreno Soto, A.; Maddalena, T.; Fraters, A.; van der Meer, D.; Lohse, D. Coalescence of Diffusively Growing Gas Bubbles. *J. Fluid Mech.* **2018**, *846*, 143–165.
- (82) Lessard, R. R.; Zieminski, S. A. Bubble Coalescence and Gas Transfer in Aqueous Electrolytic Solutions. *Ind. Eng. Chem. Fundam.* 1971, 10, 260–269.
- (83) Craig, V. S. J.; Ninham, B. W.; Pashley, R. M. Effect of Electrolytes on Bubble Coalescence. *Nature* **1993**, *364*, 317–319.
- (84) Botello-Álvarez, J. E.; Baz-Rodríguez, S. A.; González-García, R.; Estrada-Baltazar, A.; Padilla-Medina, J. A.; González-Alatorre, G.; Navarrete-Bolaños, J. L. Effect of Electrolytes in Aqueous Solution on Bubble Size in Gas-Liquid Bubble Columns. *Ind. Eng. Chem. Res.* **2011**, *50*, 12203–12207.
- (85) Dong, X.; Liu, Z.; Liu, F.; Li, Z.; Wei, W.; Wang, X.; Xu, X. Effect of Liquid Phase Rheology and Gas-Liquid Interface Property on Mass Transfer Characteristics in Bubble Columns. *Chem. Eng. Res. Des.* **2019**, *142*, 25–33.
- (86) Pang, M.; Jia, M.; Fei, Y. Experimental Study on Effect of Surfactant and Solution Property on Bubble Rising Motion. *J. Mol. Liq.* **2023**, *375*, 121390.
- (87) Besagni, G.; Inzoli, F. The Effect of Liquid Phase Properties on Bubble Column Fluid Dynamics: Gas Holdup, Flow Regime Transition, Bubble Size Distributions and Shapes, Interfacial Areas and Foaming Phenomena. *Chem. Eng. Sci.* **2017**, *170*, 270–296.
- (88) Takahashi, M. ζ Potential of Microbubbles in Aqueous Solutions: Electrical Properties of the Gas-Water Interface. *J. Phys. Chem. B* **2005**, *109*, 21858–21864.
- (89) Glas, J. P.; Westwater, J. W. Measurements of the Growth of Electrolytic Bubbles. *Int. J. Heat Mass Transfer* **1964**, *7*, 1427–1443.
- (90) Brandon, N. P.; Kelsall, G. H. Growth Kinetics of Bubbles Electrogenerated at Microelectrodes. *J. Appl. Electrochem.* **1985**, *15*, 475–484.
- (91) Gabrielli, C.; Huet, F.; Keddam, M.; Macias, A.; Sahar, A. Potential Drops Due to an Attached Bubble on a Gas-Evolving Electrode. *J. Appl. Electrochem.* **1989**, *19*, 617–629.
- (92) Karnbach, F.; Yang, X.; Mutschke, G.; Fröhlich, J.; Eckert, J.; Gebert, A.; Tschulik, K.; Eckert, K.; Uhlemann, M. Interplay of the Open Circuit Potential-Relaxation and the Dissolution Behavior of a

- Single H<sub>2</sub> Bubble Generated at a Pt Microelectrode. *J. Phys. Chem. C* **2016**, 120, 15137–15146.
- (93) Yang, X.; Karnbach, F.; Uhlemann, M.; Odenbach, S.; Eckert, K. Dynamics of Single Hydrogen Bubbles at a Platinum Microelectrode. *Langmuir* **2015**, *31*, 8184–8193.
- (94) Bashkatov, A.; Hossain, S. S.; Yang, X.; Mutschke, G.; Eckert, K. Oscillating Hydrogen Bubbles at Pt Microelectrodes. *Phys. Rev. Lett.* **2019**, *123*, 214503.
- (95) Bashkatov, A.; Hossain, S. S.; Mutschke, G.; Yang, X.; Rox, H.; Weidinger, I. M.; Eckert, K. On the Growth Regimes of Hydrogen Bubbles at Microelectrodes. *Phys. Chem. Chem. Phys.* **2022**, 24, 26738–26752.
- (96) Fernández, D.; Martine, M.; Meagher, A.; Möbius, M. E.; Coey, J. M. D. Stabilizing Effect of a Magnetic Field on a Gas Bubble Produced at a Microelectrode. *Electrochem. Commun.* **2012**, *18*, 28–32.
- (97) Liu, Y.; Pan, L.; Liu, H. The Dynamic Effect of Micro-MHD Convection on Bubble Grown at a Horizontal Microelectrode. *Int. J. Hydrogen Energy* **2021**, *46*, 13923–13935.
- (98) Massing, J.; Mutschke, G.; Baczyzmalski, D.; Hossain, S. S.; Yang, X.; Eckert, K.; Cierpka, C. Thermocapillary Convection during Hydrogen Evolution at Microelectrodes. *Electrochim. Acta* **2019**, 297, 929–940.
- (99) Bashkatov, A.; Yang, X.; Mutschke, G.; Fritzsche, B.; Hossain, S. S.; Eckert, K. Dynamics of Single Hydrogen Bubbles at Pt Microelectrodes in Microgravity. *Phys. Chem. Chem. Phys.* **2021**, 23, 11818–11830.
- (100) Kristof, P.; Pritzker, M. Effect of Electrolyte Composition on the Dynamics of Hydrogen Gas Bubble Evolution at Copper Microelectrodes. *J. Appl. Electrochem.* 1997, 27, 255–265.
- (101) Bashkatov, A.; Park, S.; Demirkir, Ç.; Wood, J. A.; Koper, M. T. M.; Lohse, D.; Krug, D. Performance Enhancement of Electrocatalytic Hydrogen Evolution through Coalescence-Induced Bubble Dynamics. *J. Am. Chem. Soc.* **2024**, *146*, 10177–10186.
- (102) Luo, L.; White, H. S. Electrogeneration of Single Nanobubbles at Sub-50-nm-Radius Platinum Nanodisk Electrodes. *Langmuir* **2013**, 29, 11169–11175.
- (103) Chen, Q.; Luo, L.; Faraji, H.; Feldberg, S. W.; White, H. S. Electrochemical Measurements of Single H<sub>2</sub> Nanobubble Nucleation and Stability at Pt Nanoelectrodes. *J. Phys. Chem. Lett.* **2014**, *5*, 3539–3544
- (104) Majumdar, P.; Qiu, Y.; White, H. S. Effect of Non-Specific Ion Adsorption and Parallel Faradaic Reactions on the Nucleation of  $\rm H_2$  Nanobubbles. *J. Electrochem. Soc.* **2022**, *169*, 106515.
- (105) Qiu, Y.; Ren, H.; Edwards, M. A.; Gao, R.; Barman, K.; White, H. S. Electrochemical Generation of Individual Nanobubbles Comprising H<sub>2</sub>, D<sub>2</sub>, and HD. *Langmuir* **2020**, *36*, 6073–6078.
- (106) Chen, Q.; Wiedenroth, H. S.; German, S. R.; White, H. S. Electrochemical Nucleation of Stable N<sub>2</sub> Nanobubbles at Pt Nanoelectrodes. *J. Am. Chem. Soc.* **2015**, *137*, 12064–12069.
- (107) Chen, Q.; Liu, Y.; Edwards, M. A.; Liu, Y.; White, H. S. Nitrogen Bubbles at Pt Nanoelectrodes in a Nonaqueous Medium: Oscillating Behavior and Geometry of Critical Nuclei. *Anal. Chem.* **2020**, *92*, 6408–6414.
- (108) Ren, H.; German, S. R.; Edwards, M. A.; Chen, Q.; White, H. S. Electrochemical Generation of Individual O<sub>2</sub> Nanobubbles via H<sub>2</sub>O<sub>2</sub> Oxidation. *J. Phys. Chem. Lett.* **2017**, *8*, 2450–2454.
- (109) Chen, Q.; Luo, L. Correlation between Gas Bubble Formation and Hydrogen Evolution Reaction Kinetics at Nanoelectrodes. *Langmuir* **2018**, *34*, 4554–4559.
- (110) Chen, Q.; Ranaweera, R.; Luo, L. Hydrogen Bubble Formation at Hydrogen-Insertion Electrodes. *J. Phys. Chem. C* **2018**, *122*, 15421–15426.
- (111) Wei, H.; Wang, H.; Tang, H.; Li, Y. Voltammetric Analysis of Single Nanobubble Formation on Ag and Ag@MoS<sub>2</sub> Nanoelectrodes. *J. Phys. Chem. C* **2021**, *125*, 3073–3080.
- (112) German, S. R.; Edwards, M. A.; Chen, Q.; White, H. S. Laplace Pressure of Individual H<sub>2</sub> Nanobubbles from Pressure-Addition Electrochemistry. *Nano Lett.* **2016**, *16*, 6691–6694.

- (113) Suvira, M.; Ahuja, A.; Lovre, P.; Singh, M.; Draher, G. W.; Zhang, B. Imaging Single H<sub>2</sub> Nanobubbles Using Off-Axis Dark-Field Microscopy. *Anal. Chem.* **2023**, *95*, 15893–15899.
- (114) Soto, Á. M.; German, S. R.; Ren, H.; Van Der Meer, D.; Lohse, D.; Edwards, M. A.; White, H. S. The Nucleation Rate of Single O<sub>2</sub> Nanobubbles at Pt Nanoelectrodes. *Langmuir* **2018**, *34*, 7309–7318.
- (115) Luo, L.; German, S. R.; Lan, W.-J.; Holden, D. A.; Mega, T. L.; White, H. S. Resistive-Pulse Analysis of Nanoparticles. *Annu. Rev. Anal. Chem.* **2014**, *7*, 513–535.
- (116) Coulter, W. H. Means for Counting Particles Suspended in a Fluid. US2656508A, October 20, 1953. https://patents.google.com/patent/US2656508A/.
- (117) Hu, Y.-X.; Ying, Y.-L.; Gao, R.; Yu, R.-J.; Long, Y.-T. Characterization of the Dynamic Growth of the Nanobubble within the Confined Glass Nanopore. *Anal. Chem.* **2018**, *90*, 12352–12355.
- (118) Li, Q.; Ying, Y.-L.; Liu, S.-C.; Hu, Y.-X.; Long, Y.-T. Measuring Temperature Effects on Nanobubble Nucleation via a Solid-State Nanopore. *Analyst* **2020**, *145*, 2510–2514.
- (119) Li, Q.; Ying, Y.; Hu, Y.; Liu, S.; Long, Y. Monitoring Nanobubble Nucleation at Early-Stage within a Sub-9 nm Solid-State Nanopore. *Electrophoresis* **2020**, *41*, 959–965.
- (120) Lu, S.-M.; Li, Y.-J.; Zhang, J.-F.; Wang, Y.; Ying, Y.-L.; Long, Y.-T. Monitoring Hydrogen Evolution Reaction Catalyzed by MoS<sub>2</sub> Quantum Dots on a Single Nanoparticle Electrode. *Anal. Chem.* **2019**, *91*, 10361–10365.
- (121) Bai, S.; You, Y.; Chen, X.; Liu, C.; Wang, L. Monitoring Bipolar Electrochemistry and Hydrogen Evolution Reaction of a Single Gold Microparticle under Sub-Micropipette Confinement. *Anal. Chem.* **2023**, *95*, 2054–2061.
- (122) Zhang, R.; Liu, X.; Zeng, Q.; Shen, H.; Wang, L. Studies on the Morphology Effect on Catalytic Ability of a Single MnO<sub>2</sub> Catalyst Particle with a Solid Nanopipette. ACS Sens. 2022, 7, 338–344.
- (123) Wang, Y.; Gordon, E.; Ren, H. Mapping the Nucleation of H<sub>2</sub> Bubbles on Polycrystalline Pt via Scanning Electrochemical Cell Microscopy. *J. Phys. Chem. Lett.* **2019**, *10*, 3887–3892.
- (124) Perera, R. T.; Arcadia, C. E.; Rosenstein, J. K. Probing the Nucleation, Growth, and Evolution of Hydrogen Nanobubbles at Single Catalytic Sites. *Electrochim. Acta* **2018**, 283, 1773–1778.
- (125) Jin, C.; Liu, Y.-L.; Shan, Y.; Chen, Q.-J. Scanning Electrochemical Cell Microscope Study of Individual H<sub>2</sub> Gas Bubble Nucleation on Platinum: Effect of Surfactants. *Chin. J. Anal. Chem.* **2021**, 49, e21055–e21064.
- (126) Liu, Y.; Jin, C.; Liu, Y.; Ruiz, K. H.; Ren, H.; Fan, Y.; White, H. S.; Chen, Q. Visualization and Quantification of Electrochemical H<sub>2</sub> Bubble Nucleation at Pt, Au, and MoS<sub>2</sub> Substrates. *ACS Sens.* **2021**, *6*, 355–363.
- (127) Liu, Y.; Lu, X.; Peng, Y.; Chen, Q. Electrochemical Visualization of Gas Bubbles on Superaerophobic Electrodes Using Scanning Electrochemical Cell Microscopy. *Anal. Chem.* **2021**, *93*, 12337–12345.
- (128) Deng, X.; Shan, Y.; Meng, X.; Yu, Z.; Lu, X.; Ma, Y.; Zhao, J.; Qiu, D.; Zhang, X.; Liu, Y.; Chen, Q. Direct Measuring of Single-Heterogeneous Bubble Nucleation Mediated by Surface Topology. *Proc. Natl. Acad. Sci. U.S.A.* **2022**, *119*, No. e2205827119.
- (129) Georgescu, N. S.; Robinson, D. A.; White, H. S. Effect of Nonuniform Mass Transport on Nanobubble Nucleation at Individual Pt Nanoparticles. *J. Phys. Chem. C* **2021**, *125*, 19724–19732.
- (130) Gao, R.; Edwards, M. A.; Qiu, Y.; Barman, K.; White, H. S. Visualization of Hydrogen Evolution at Individual Platinum Nanoparticles at a Buried Interface. *J. Am. Chem. Soc.* **2020**, *142*, 8890.
- (131) Ma, W.; Hu, K.; Chen, Q.; Zhou, M.; Mirkin, M. V.; Bard, A. J. Electrochemical Size Measurement and Characterization of Electrodeposited Platinum Nanoparticles at Nanometer Resolution with Scanning Electrochemical Microscopy. *Nano Lett.* **2017**, *17*, 4354–4358.
- (132) Amemiya, S.; Bard, A. J.; Fan, F.-R. F.; Mirkin, M. V.; Unwin, P. R. Scanning Electrochemical Microscopy. *Annu. Rev. Anal. Chem.* **2008**, *1*, 95–131.

- (133) Botz, A. J.; Nebel, M.; Rincón, R. A.; Ventosa, E.; Schuhmann, W. Onset Potential Determination at Gas-Evolving Catalysts by Means of Constant-Distance Mode Positioning of Nanoelectrodes. *Electrochim. Acta* **2015**, *179*, 38–44.
- (134) Chen, X.; Maljusch, A.; Rincon, R. A.; Battistel, A.; Bandarenka, A. S.; Schuhmann, W. Local Visualization of Catalytic Activity at Gas Evolving Electrodes Using Frequency-Dependent Scanning Electrochemical Microscopy. *Chem. Commun.* **2014**, *50*, 13250–13253.
- (135) Zeradjanin, A. R.; Ventosa, E.; Bondarenko, A. S.; Schuhmann, W. Evaluation of the Catalytic Performance of Gas-Evolving Electrodes Using Local Electrochemical Noise Measurements. *ChemSusChem* **2012**, *5*, 1905–1911.
- (136) Battistel, A.; Dennison, C. R.; Lesch, A.; Girault, H. H. Local Study on Hydrogen and Hydrogen Gas Bubble Formation on a Platinum Electrode. *J. Phys. Chem. C* **2019**, *123*, 10849–10856.
- (137) Kim, Y. J.; Lim, A.; Kim, J. M.; Lim, D.; Chae, K. H.; Cho, E. N.; Han, H. J.; Jeon, K. U.; Kim, M.; Lee, G. H.; et al. Highly Efficient Oxygen Evolution Reaction via Facile Bubble Transport Realized by Three-Dimensionally Stack-Printed Catalysts. *Nat. Commun.* **2020**, *11*, 4921.
- (138) Zhang, L.; Zhang, Y.; Zhang, X.; Li, Z.; Shen, G.; Ye, M.; Fan, C.; Fang, H.; Hu, J. Electrochemically Controlled Formation and Growth of Hydrogen Nanobubbles. *Langmuir* **2006**, 22, 8109–8113.
- (139) Zhang, L.; Zhang, X.; Zhang, Y.; Hu, J.; Fang, H. The Length Scales for Stable Gas Nanobubbles at Liquid/Solid Surfaces. *Soft Matter* **2010**, *6*, 4515–4519.
- (140) Yang, S.; Tsai, P.; Kooij, E. S.; Prosperetti, A.; Zandvliet, H. J. W.; Lohse, D. Electrolytically Generated Nanobubbles on Highly Orientated Pyrolytic Graphite Surfaces. *Langmuir* **2009**, *25*, 1466–1474.
- (141) Yu, J.; Hu, K.; Zhang, Z.; Luo, L.; Liu, Y.; Zhou, D.; Wang, F.; Kuang, Y.; Xu, H.; Li, H.; Duan, H.; Sun, X. Interfacial Nanobubbles' Growth at the Initial Stage of Electrocatalytic Hydrogen Evolution. *Energy Environ. Sci.* **2023**, *16*, 2068–2079.
- (142) Mita, M.; Matsushima, H.; Ueda, M.; Ito, H. In-Situ High-Speed Atomic Force Microscopy Observation of Dynamic Nanobubbles during Water Electrolysis. *J. Colloid Interface Sci.* **2022**, *614*, 389–395.
- (143) An, H.; Tan, B. H.; Moo, J. G. S.; Liu, S.; Pumera, M.; Ohl, C.-D. Graphene Nanobubbles Produced by Water Splitting. *Nano Lett.* **2017**, *17*, 2833–2838.
- (144) Dollekamp, E.; Bampoulis, P.; Poelsema, B.; Zandvliet, H. J. W.; Kooij, E. S. Electrochemically Induced Nanobubbles between Graphene and Mica. *Langmuir* **2016**, 32, 6582–6590.
- (145) Donose, B. C.; Harnisch, F.; Taran, E. Electrochemically Produced Hydrogen Bubble Probes for Gas Evolution Kinetics and Force Spectroscopy. *Electrochem. Commun.* **2012**, *24*, 21–24.
- (146) Kou, T.; Wang, S.; Shi, R.; Zhang, T.; Chiovoloni, S.; Lu, J. Q.; Chen, W.; Worsley, M. A.; Wood, B. C.; Baker, S. E.; Duoss, E. B.; Wu, R.; Zhu, C.; Li, Y. Periodic Porous 3D Electrodes Mitigate Gas Bubble Traffic during Alkaline Water Electrolysis at High Current Densities. *Adv. Energy Mater.* **2020**, *10*, 2002955.
- (147) Li, F.; Ma, K.; Liu, L.; Xi, J.; Qiu, X. Characterizing the Onset Potential Distribution of Pt/C Catalyst Deposition by a Total Internal Reflection Imaging Method. *Small* **2021**, *17*, 2102407.
- (148) Kempler, P. A.; Coridan, R. H.; Lewis, N. S. Effects of Bubbles on the Electrochemical Behavior of Hydrogen-Evolving Si Microwire Arrays Oriented against Gravity. *Energy Environ. Sci.* **2020**, *13*, 1808–1817.
- (149) Pande, N.; Mul, G.; Lohse, D.; Mei, B. Correlating the Short-Time Current Response of a Hydrogen Evolving Nickel Electrode to Bubble Growth. *J. Electrochem. Soc.* **2019**, *166*, No. E280.
- (150) Coridan, R. H.; Schichtl, Z. G.; Sun, T.; Fezzaa, K. Inhibition of Tafel Kinetics for Electrolytic Hydrogen Evolution on Isolated Micron Scale Electrocatalysts on Semiconductor Interfaces. *ACS Appl. Mater. Interfaces* **2016**, *8*, 24162.

- (151) Mandin, P.; Derhoumi, Z.; Roustan, H.; Rolf, W. Bubble Over-Potential During Two-Phase Alkaline Water Electrolysis. *Electrochim. Acta* **2014**, *128*, 248–258.
- (152) Iwata, R.; Zhang, L.; Wilke, K. L.; Gong, S.; He, M.; Gallant, B. M.; Wang, E. N. Bubble Growth and Departure Modes on Wettable/Non-Wettable Porous Foams in Alkaline Water Splitting. *Joule* **2021**, *5*, 887–900.
- (153) Lee, C.; Hinebaugh, J.; Banerjee, R.; Chevalier, S.; Abouatallah, R.; Wang, R.; Bazylak, A. Influence of Limiting Throat and Flow Regime on Oxygen Bubble Saturation of Polymer Electrolyte Membrane Electrolyzer Porous Transport Layers. *Int. J. Hydrogen Energy* **2017**, 42, 2724–2735.
- (154) Leenheer, A. J.; Atwater, H. A. Water-Splitting Photoelectrolysis Reaction Rate via Microscopic Imaging of Evolved Oxygen Bubbles. *J. Electrochem. Soc.* **2010**, *157*, B1290—B1294.
- (155) Dorfi, A. E.; West, A. C.; Esposito, D. V. Quantifying Losses in Photoelectrode Performance Due to Single Hydrogen Bubbles. *J. Phys. Chem. C* **2017**, *121*, 26587–26597.
- (156) Hao, R.; Fan, Y.; Howard, M. D.; Vaughan, J. C.; Zhang, B. Imaging Nanobubble Nucleation and Hydrogen Spillover during Electrocatalytic Water Splitting. *Proc. Natl. Acad. Sci. U.S.A.* **2018**, 115, 5878–5883.
- (157) Hao, R.; Fan, Y.; Anderson, T. J.; Zhang, B. Imaging Single Nanobubbles of  $H_2$  and  $O_2$  During the Overall Water Electrolysis with Single-Molecule Fluorescence Microscopy. *Anal. Chem.* **2020**, 92, 3682–3688.
- (158) Peng, Z.; Zhang, B. Nanobubble Labeling and Imaging with a Solvatochromic Fluorophore Nile Red. *Anal. Chem.* **2021**, 93, 15315—15322.
- (159) Suvira, M.; Zhang, B. Effect of Surfactant on Electrochemically Generated Surface Nanobubbles. *Anal. Chem.* **2021**, 93, 5170–5176. (160) Suvira, M.; Zhang, B. Single-Molecule Interactions at a
- Surfactant-Modified H<sub>2</sub> Surface Nanobubble. *Langmuir* **2021**, 37, 13816–13823.
- (161) Leininger, W. R.; Peng, Z.; Zhang, B. Transient Adsorption Behavior of Single Fluorophores on an Electrode-Supported Nanobubble. *Chem. Biomed. Imaging* **2023**, *1*, 380–386.
- (162) Wang, J.-G.; Zhang, L.; Xie, J.; Weizmann, Y.; Li, D.; Li, J. Single Particle Hopping as an Indicator for Evaluating Electrocatalysts. *Nano Lett.* **2022**, 22, 5495–5502.
- (163) Ma, C.; Wei, H.-F.; Wang, M.-X.; Wu, S.; Chang, Y.-C.; Zhang, J.; Jiang, L.-P.; Zhu, W.; Chen, Z.; Lin, Y. Hydrogen Evolution Reaction Monitored by Electrochemiluminescence Blinking at Single-Nanoparticle Level. *Nano Lett.* **2020**, *20*, 5008–5016.
- (164) Vogel, Y. B.; Evans, C. W.; Belotti, M.; Xu, L.; Russell, I. C.; Yu, L.-J.; Fung, A. K. K.; Hill, N. S.; Darwish, N.; Gonçales, V. R.; Coote, M. L.; Swaminathan Iyer, K.; Ciampi, S. The Corona of a Surface Bubble Promotes Electrochemical Reactions. *Nat. Commun.* **2020**, *11*, 6323.
- (165) Lemineur, J.-F.; Ciocci, P.; Noël, J.-M.; Ge, H.; Combellas, C.; Kanoufi, F. Imaging and Quantifying the Formation of Single Nanobubbles at Single Platinum Nanoparticles during the Hydrogen Evolution Reaction. *ACS Nano* **2021**, *15*, 2643–2653.
- (166) Xu, S.; Yu, X.; Chen, Z.; Zeng, Y.; Guo, L.; Li, L.; Luo, F.; Wang, J.; Qiu, B.; Lin, Z. Real-Time Visualization of the Single-Nanoparticle Electrocatalytic Hydrogen Generation Process and Activity under Dark Field Microscopy. *Anal. Chem.* **2020**, *92*, 9016–9023.
- (167) Wang, Y.; Yuan, T.; Su, H.; Zhou, K.; Yin, L.; Wang, W. A Bubble-STORM Approach for Super-Resolved Imaging of Nucleation Sites in Hydrogen Evolution Reactions. *ACS Sens.* **2021**, *6*, 380–386. (168) Barr, V. A.; Bunnell, S. C. Interference Reflection Microscopy. *Curr. Protoc. Cell Biol.* **2009**, *45*, 4–23.
- (169) Ciocci, P.; Lemineur, J.-F.; Noël, J.-M.; Combellas, C.; Kanoufi, F. Differentiating Electrochemically Active Regions of Indium Tin Oxide Electrodes for Hydrogen Evolution and Reductive Decomposition Reactions. An In Situ Optical Microscopy Approach. *Electrochim. Acta* 2021, 386, 138498.

- (170) Hu, M.; Novo, C.; Funston, A.; Wang, H.; Staleva, H.; Zou, S.; Mulvaney, P.; Xia, Y.; Hartland, G. V. Dark-Field Microscopy Studies of Single Metal Nanoparticles: Understanding the Factors that Influence the Linewidth of the Localized Surface Plasmon Resonance. *J. Mater. Chem.* **2008**, *18*, 1949–1960.
- (171) Bhandari, P.; Wang, X.; Irudayaraj, J. Oxygen Nanobubble Tracking by Light Scattering in Single Cells and Tissues. *ACS Nano* **2017**, *11*, 2682–2688.
- (172) Li, S.; Du, Y.; He, T.; Shen, Y.; Bai, C.; Ning, F.; Hu, X.; Wang, W.; Xi, S.; Zhou, X. Nanobubbles: An Effective Way to Study Gas-Generating Catalysis on a Single Nanoparticle. *J. Am. Chem. Soc.* **2017**, 139, 14277–14284.
- (173) Shan, X.; Díez-Pérez, I.; Wang, L.; Wiktor, P.; Gu, Y.; Zhang, L.; Wang, W.; Lu, J.; Wang, S.; Gong, Q.; Li, J.; Tao, N. Imaging the Electrocatalytic Activity of Single Nanoparticles. *Nat. Nanotechnol.* **2012**, *7*, 668–672.
- (174) Chen, J.; Zhou, K.; Wang, Y.; Gao, J.; Yuan, T.; Pang, J.; Tang, S.; Chen, H.-Y.; Wang, W. Measuring the Activation Energy Barrier for the Nucleation of Single Nanosized Vapor Bubbles. *Proc. Natl. Acad. Sci. U.S.A.* **2019**, *116*, 12678–12683.
- (175) Wang, Y.; Chen, J.; Jiang, Y.; Wang, X.; Wang, W. Label-Free Optical Imaging of the Dynamic Stick-Slip and Migration of Single Sub-100-nm Surface Nanobubbles: A Superlocalization Approach. *Anal. Chem.* **2019**, *91*, 4665–4671.
- (176) Fang, Y.; Li, Z.; Jiang, Y.; Wang, X.; Chen, H.-Y.; Tao, N.; Wang, W. Intermittent Photocatalytic Activity of Single CdS Nanoparticles. *Proc. Natl. Acad. Sci. U.S.A.* **2017**, *114*, 10566–10571.
- (177) Zhou, K.; Chang, A.; Wang, X.; Jiang, Y.; Wang, Y.; Lu, X.; Wang, W. Refractive Index of Single Surface Nanobubbles. *Chem. Biomed. Imaging* **2023**, *1*, 387–394.
- (178) Liu, Y.; Dillon, S. J. In Situ Observation of Electrolytic H<sub>2</sub> Evolution Adjacent to Gold Cathodes. *Chem. Commun.* **2014**, 50, 1761–1763.
- (179) Ross, F. M. Opportunities and Challenges in Liquid Cell Electron Microscopy. *Science* **2015**, *350*, aaa9886.
- (180) Ji, Y.; Yin, Z.-W.; Yang, Z.; Deng, Y.-P.; Chen, H.; Lin, C.; Yang, L.; Yang, K.; Zhang, M.; Xiao, Q.; Li, J.-T.; Chen, Z.; Sun, S.-G.; Pan, F. From Bulk to Interface: Electrochemical Phenomena and Mechanism Studies in Batteries via Electrochemical Quartz Crystal Microbalance. *Chem. Soc. Rev.* 2021, *50*, 10743–10763.
- (181) Carr, M. W.; Hillman, A. R.; Lubetkin, S. D.; Swann, M. J. Detection of Electrolytically Generated Bubbles Using an Electrochemical Quartz Crystal Microbalance. *J. Electroanal. Chem. Interfacial Electrochem.* 1989, 267, 313–320.
- (182) Li, F.-B.; Robert Hillman, A.; Lubetkin, S. D.; Roberts, D. J. Electrochemical Quartz Crystal Microbalance Studies of Potentiodynamic Electrolysis of Aqueous Chloride Solution: Surface Processes and Evolution of H<sub>2</sub> and Cl<sub>2</sub> Gas Bubbles. *J. Electroanal. Chem.* **1992**, 335, 345–362.
- (183) Li, F.-B.; Lubetkin, S. D.; Roberts, D. J.; Hillman, A. R. Electrogravimetric and Chronoamperometric Monitoring of Individual Events of Growth and Detachment of Electrolytic Chlorine Gas Bubbles. J. Chem. Soc., Chem. Commun. 1994, 2, 159–160.
- (184) Tsionsky, V.; Kaverin, A.; Daikhin, L.; Katz, G.; Gileadi, E. An Experimental Verification of the Possible Influence of Gas Nano-Bubbles on the Response of an Electrochemical Quartz Crystal Microbalance. *Phys. Chem. Chem. Phys.* **2005**, *7*, 1830–1835.
- (185) Zhang, X. H. Quartz Crystal Microbalance Study of the Interfacial Nanobubbles. *Phys. Chem. Chem. Phys.* **2008**, *10*, 6842–6848.
- (186) Zhang, X.-X.; Wang, Z.; Yue, X.; Ma, Y.; Kiesewetter, D. O.; Chen, X. pH-Sensitive Fluorescent Dyes: Are They Really pH-Sensitive in Cells? *Mol. Pharmaceutics* **2013**, *10*, 1910–1917.
- (187) Chandra, A.; Prasad, S.; Iuele, H.; Colella, F.; Rizzo, R.; D'Amone, E.; Gigli, G.; del Mercato, L. L. Highly Sensitive Fluorescent pH Microsensors Based on the Ratiometric Dye Pyranine Immobilized on Silica Microparticles. *Chem. Euro. J.* **2021**, 27, 13318–13324.

- (188) Peddie, W. 4. On Transition Resistance at the Surface of Platinum Electrodes, and the Action of Condensed Gaseous Films. *Proc. R. Soc. Edinburgh* **1888**, *14*, 221–229.
- (189) Glasstone, S. The Measurement and Cause of Overvoltage. *Trans. Faraday Soc.* **1924**, *19*, 808–816.
- (190) Eyring, H.; Glasstone, S.; Laidler, K. J. A New Theory of Overvoltage. *Trans. Electrochem. Soc.* **1939**, 76, 145.
- (191) Rue, R. E. D. L.; Tobias, C. W. On the Conductivity of Dispersions. J. Electrochem. Soc. 1959, 106, 827.
- (192) Sides, P. J.; Tobias, C. W. Primary Potential and Current Distribution Around a Bubble on an Electrode. *J. Electrochem. Soc.* **1980**, 127, 288.
- (193) Sides, P. J.; Tobias, C. W. Resistance of a Planar Array of Spheres: Gas Bubbles on an Electrode. *J. Electrochem. Soc.* **1982**, 129, 2715.
- (194) Hine, F.; Murakami, K. Bubble Effects on the Solution IR Drop in a Vertical Electrolyzer Under Free and Forced Convection. *J. Electrochem. Soc.* **1980**, *127*, 292.
- (195) Janssen, L. J. J.; Barendrecht, E. Electrolytic Resistance of Solution Layers at Hydrogen and Oxygen Evolving Electrodes in Alkaline Solution. *Electrochim. Acta* 1983, 28, 341–346.
- (196) Dukovic, J.; Tobias, C. W. The Influence of Attached Bubbles on Potential Drop and Current Distribution at Gas-Evolving Electrodes. J. Electrochem. Soc. 1987, 134, 331.
- (197) Venczel, J. Ueber Den Stofftransport an Gasentwickelnden Elektroden. PhD Thesis, ETH Zurich, 1961.
- (198) Adam, E.; Venczel, J.; Schalch, E. Stofftransport Bei Der Elektrolyse Mit Gasrührung. *Chemie Ingenieur Technik* 1971, 43, 202–215.
- (199) Janssen, L. J. J.; Hoogland, J. G. The Effect of Electrolytically Evolved Gas Bubbles on the Thickness of the Diffusion Layer—II. *Electrochim. Acta* 1973, 18, 543–550.
- (200) Brauns, J.; Turek, T. Alkaline Water Electrolysis Powered by Renewable Energy: A Review. *Processes* **2020**, *8*, 248.
- (201) Brauns, J.; Turek, T. Experimental Evaluation of Dynamic Operating Concepts for Alkaline Water Electrolyzers Powered by Renewable Energy. *Electrochim. Acta* **2022**, 404, 139715.
- (202) Brauns, J.; Schönebeck, J.; Kraglund, M. R.; Aili, D.; Hnát, J.; Žitka, J.; Mues, W.; Jensen, J. O.; Bouzek, K.; Turek, T. Evaluation of Diaphragms and Membranes as Separators for Alkaline Water Electrolysis. *J. Electrochem. Soc.* **2021**, *168*, 014510.
- (203) Lira Garcia Barros, R.; Kraakman, J.; de Groot, T. T.; van der Schaaf, J. Gas Crossover and Supersaturation in Advanced Alkaline Water Electrolysis. In *Electrochemical Society Meeting Abstracts* 243; The Electrochemical Society, Inc., 2023; pp 1967.
- (204) Ibl, N. Probleme des Stofftransportes in der Angewandten Elektrochemie. Chem. Ing. Technol. 1963, 35, 353–361.
- (205) Vogt, H. The Quantities Affecting the Bubble Coverage of Gas-Evolving Electrodes. *Electrochim. Acta* **2017**, 235, 495–499.
- (206) Vogt, H.; Stephan, K. Local Microprocesses at Gas-Evolving Electrodes and Their Influence on Mass Transfer. *Electrochim. Acta* **2015**, *155*, 348–356.
- (207) Tilak, B. V.; Lu, P. W. T.; Colman, J. E.; Srinivasan, S. Electrolytic Production of Hydrogen. In *Comprehensive Treatise of Electrochemistry: Electrochemical Processing*; Bockris, J. O., Conway, B. E., Yeager, E., White, R. E., Eds.; Comprehensive Treatise of Electrochemistry; Springer US: Boston, MA, 1981; pp 1–104.
- (208) Ayers, K.; Danilovic, N.; Harrison, K.; Xu, H. PEM Electrolysis, a Forerunner for Clean Hydrogen. *Electrochem. Soc. Interface* **2021**, *30*, *67*.
- (209) Fuller, T. F.; Harb, J. N. Electrochemical Engineering; John Wiley & Sons, 2018.
- (210) Zhang, D.; Zeng, K. Evaluating the Behavior of Electrolytic Gas Bubbles and Their Effect on the Cell Voltage in Alkaline Water Electrolysis. *Ind. Eng. Chem. Res.* **2012**, *51*, 13825–13832.
- (211) Iwata, R.; Zhang, L.; Wilke, K. L.; Gong, S.; He, M.; Gallant, B. M.; Wang, E. N. Bubble Growth and Departure Modes on Wettable/Non-Wettable Porous Foams in Alkaline Water Splitting. *Joule* **2021**, *5*, 887–900.

- (212) Janssen, L. J. J.; van Stralen, S. J. D. Bubble Behaviour on and Mass Transfer to an Oxygen-Evolving Transparent Nickel Electrode in Alkaline Solution. *Electrochim. Acta* 1981, 26, 1011–1022.
- (213) Janssen, L. J. J.; Sillen, C. W. M. P.; Barendrecht, E.; van Stralen, S. J. D. Bubble Behaviour during Oxygen and Hydrogen Evolution at Transparent Electrodes in KOH Solution. *Electrochim. Acta* 1984, 29, 633–642.
- (214) Deng, X.; Yang, F.; Li, Y.; Dang, J.; Ouyang, M. Quantitative Study on Gas Evolution Effects under Large Current Density in Zero-Gap Alkaline Water Electrolyzers. *J. Power Sources* **2023**, 555, 232378.
- (215) Fischer, J.; Hofmann, H.; Luft, G.; Wendt, H. Fundamental Investigations and Electrochemical Engineering Aspects Concerning an Advanced Concept for Alkaline Water Electrolysis. *AIChE J.* **1980**, 26, 794–802.
- (216) Kraglund, M. R.; Carmo, M.; Schiller, G.; Ansar, S. A.; Aili, D.; Christensen, E.; Jensen, J. O. Ion-Solvating Membranes as a New Approach towards High Rate Alkaline Electrolyzers. *Energy Environ. Sci.* **2019**, *12*, 3313–3318.
- (217) Kraglund, M. R.; Aili, D.; Jankova, K.; Christensen, E.; Li, Q.; Jensen, J. O. Zero-Gap Alkaline Water Electrolysis Using Ion-Solvating Polymer Electrolyte Membranes at Reduced KOH Concentrations. *J. Electrochem. Soc.* **2016**, *163*, F3125.
- (218) Marini, S.; Salvi, P.; Nelli, P.; Pesenti, R.; Villa, M.; Berrettoni, M.; Zangari, G.; Kiros, Y. Advanced Alkaline Water Electrolysis. *Electrochim. Acta* **2012**, *82*, 384–391.
- (219) Marini, S.; Salvi, P.; Nelli, P.; Pesenti, R.; Villa, M.; Kiros, Y. Stable and Inexpensive Electrodes for the Hydrogen Evolution Reaction. *Int. J. Hydrogen Energy* **2013**, *38*, 11484–11495.
- (220) Koj, M.; Qian, J.; Turek, T. Novel Alkaline Water Electrolysis with Nickel-Iron Gas Diffusion Electrode for Oxygen Evolution. *Int. J. Hydrogen Energy* **2019**, *44*, 29862–29875.
- (221) Tiwari, P.; Tsekouras, G.; Wagner, K.; Swiegers, G. F.; Wallace, G. G. A New Class of Bubble-Free Water Electrolyzer That Is Intrinsically Highly Efficient. *Int. J. Hydrogen Energy* **2019**, 44, 23568–23579.
- (222) Hodges, A.; Hoang, A. L.; Tsekouras, G.; Wagner, K.; Lee, C.-Y.; Swiegers, G. F.; Wallace, G. G. A High-Performance Capillary-Fed Electrolysis Cell Promises More Cost-Competitive Renewable Hydrogen. *Nat. Commun.* **2022**, *13*, 1304.
- (223) Deng, K.; Feng, H.; Zhang, Y.; Liu, D.; Li, Q. Ampere-Level Membrane-Less Water Electrolysis Enabled by Rose-Petal-Effect-Mimetic Interface. *Joule* **2023**, *7*, 1852–1866.
- (224) Koza, J. A.; Mühlenhoff, S.; Żabiński, P.; Nikrityuk, P. A.; Eckert, K.; Uhlemann, M.; Gebert, A.; Weier, T.; Schultz, L.; Odenbach, S. Hydrogen Evolution under the Influence of a Magnetic Field. *Electrochim. Acta* **2011**, *56*, 2665–2675.
- (225) He, Y.; Cui, Y.; Zhao, Z.; Chen, Y.; Shang, W.; Tan, P. Strategies for Bubble Removal in Electrochemical Systems. *Energy Rev.* 2023, *2*, 100015.
- (226) Fornaciari, J. C.; Gerhardt, M. R.; Zhou, J.; Regmi, Y. N.; Danilovic, N.; Bell, A. T.; Weber, A. Z. The Role of Water in Vapor-Fed Proton-Exchange-Membrane Electrolysis. *J. Electrochem. Soc.* **2020**, *167*, 104508.
- (227) Spurgeon, J. M.; Lewis, N. S. Proton Exchange Membrane Electrolysis Sustained by Water Vapor. *Energy Environ. Sci.* **2011**, *4*, 2993–2998.
- (228) Lewinski, K. A.; van der Vliet, D.; Luopa, S. M. NSTF Advances for PEM Electrolysis the Effect of Alloying on Activity of NSTF Electrolyzer Catalysts and Performance of NSTF Based PEM Electrolyzers. *ECS Trans.* **2015**, *69*, 893.
- (229) Ayers, K.; Danilovic, N.; Ouimet, R.; Carmo, M.; Pivovar, B.; Bornstein, M. Perspectives on Low-Temperature Electrolysis and Potential for Renewable Hydrogen at Scale. *Annu. Rev. Chem. Biomol. Eng.* **2019**, *10*, 219–239.
- (230) Lee, J. K.; Lee, C.; Fahy, K. F.; Zhao, B.; LaManna, J. M.; Baltic, E.; Jacobson, D. L.; Hussey, D. S.; Bazylak, A. Critical Current Density as a Performance Indicator for Gas-Evolving Electrochemical Devices. *Cell Rep. Phys. Sci.* **2021**, *2*, 100440.

- (231) Regmi, Y. N.; Peng, X.; Fornaciari, J. C.; Wei, M.; Myers, D. J.; Weber, A. Z.; Danilovic, N. A Low Temperature Unitized Regenerative Fuel Cell Realizing 60% Round Trip Efficiency and 10000 Cycles of Durability for Energy Storage Applications. *Energy Environ. Sci.* 2020, 13, 2096–2105.
- (232) Peng, X.; Taie, Z.; Liu, J.; Zhang, Y.; Peng, X.; Regmi, Y. N.; Fornaciari, J. C.; Capuano, C.; Binny, D.; Kariuki, N. N.; et al. Hierarchical Electrode Design of Highly Efficient and Stable Unitized Regenerative Fuel Cells (URFCs) for Long-Term Energy Storage. *Energy Environ. Sci.* **2020**, *13*, 4872–4881.
- (233) Grigoriev, S. A.; Millet, P.; Volobuev, S. A.; Fateev, V. N. Optimization of Porous Current Collectors for PEM Water Electrolysers. *Int. J. Hydrogen Energy* **2009**, *34*, 4968–4973.
- (234) Suermann, M.; Takanohashi, K.; Lamibrac, A.; Schmidt, T. J.; Büchi, F. N. Influence of Operating Conditions and Material Properties on the Mass Transport Losses of Polymer Electrolyte Water Electrolysis. *J. Electrochem. Soc.* **2017**, *164*, F973.
- (235) Lopata, J.; Kang, Z.; Young, J.; Bender, G.; Weidner, J. W.; Shimpalee, S. Effects of the Transport/Catalyst Layer Interface and Catalyst Loading on Mass and Charge Transport Phenomena in Polymer Electrolyte Membrane Water Electrolysis Devices. *J. Electrochem. Soc.* **2020**, *167*, 064507.
- (236) Bromberger, K.; Ghinaiya, J.; Lickert, T.; Fallisch, A.; Smolinka, T. Hydraulic Ex Situ Through-Plane Characterization of Porous Transport Layers in PEM Water Electrolysis Cells. *Int. J. Hydrogen Energy* **2018**, 43, 2556–2569.
- (237) Lickert, T.; Kiermaier, M. L.; Bromberger, K.; Ghinaiya, J.; Metz, S.; Fallisch, A.; Smolinka, T. On the Influence of the Anodic Porous Transport Layer on PEM Electrolysis Performance at High Current Densities. *Int. J. Hydrogen Energy* **2020**, *45*, 6047–6058.
- (238) Stiber, S.; Balzer, H.; Wierhake, A.; Wirkert, F. J.; Roth, J.; Rost, U.; Brodmann, M.; Lee, J. K.; Bazylak, A.; Waiblinger, W.; Gago, A. S.; Friedrich, K. A. Porous Transport Layers for Proton Exchange Membrane Electrolysis Under Extreme Conditions of Current Density, Temperature, and Pressure. *Adv. Energy Mater.* **2021**, *11*, 2100630.
- (239) Lettenmeier, P.; Kolb, S.; Sata, N.; Fallisch, A.; Zielke, L.; Thiele, S.; Gago, A.-S.; Friedrich, K. A. Comprehensive Investigation of Novel Pore-Graded Gas Diffusion Layers for High-Performance and Cost-Effective Proton Exchange Membrane Electrolyzers. *Energy Environ. Sci.* **2017**, *10*, 2521–2533.
- (240) Schuler, T.; Ciccone, J. M.; Krentscher, B.; Marone, F.; Peter, C.; Schmidt, T. J.; Büchi, F. N. Hierarchically Structured Porous Transport Layers for Polymer Electrolyte Water Electrolysis. *Adv. Energy Mater.* **2020**, *10*, 1903216.
- (241) Lee, J. K.; Lee, C.; Fahy, K. F.; Kim, P. J.; Krause, K.; LaManna, J. M.; Baltic, E.; Jacobson, D. L.; Hussey, D. S.; Bazylak, A. Accelerating Bubble Detachment in Porous Transport Layers with Patterned Through-Pores. ACS Appl. Energy Mater. 2020, 3, 9676–9684
- (242) Lee, C.; Lee, J.; Zhao, B.; Fahy, K.; Bazylak, A. Transient Gas Distribution in Porous Transport Layers of Polymer Electrolyte Membrane Electrolyzers. *J. Electrochem. Soc.* **2020**, *167*, 024508.
- (243) Tian, B.; Li, Y.; Liu, Y.; Ning, F.; Dan, X.; Wen, Q.; He, L.; He, C.; Shen, M.; Zhou, X. Ordered Membrane Electrode Assembly with Drastically Enhanced Proton and Mass Transport for Proton Exchange Membrane Water Electrolysis. *Nano Lett.* **2023**, 23, 6474–6481.
- (244) Wang, W.; Li, K.; Ding, L.; Yu, S.; Xie, Z.; Cullen, D. A.; Yu, H.; Bender, G.; Kang, Z.; Wrubel, J. A.; Ma, Z.; Capuano, C. B.; Keane, A.; Ayers, K.; Zhang, F.-Y. Exploring the Impacts of Conditioning on Proton Exchange Membrane Electrolyzers by In Situ Visualization and Electrochemistry Characterization. ACS Appl. Mater. Interfaces 2022, 14, 9002–9012.
- (245) Ding, L.; Wang, W.; Xie, Z.; Li, K.; Yu, S.; Capuano, C. B.; Keane, A.; Ayers, K.; Zhang, F.-Y. Highly Porous Iridium Thin Electrodes with Low Loading and Improved Reaction Kinetics for Hydrogen Generation in PEM Electrolyzer Cells. ACS Appl. Mater. Interfaces 2023, 15, 24284–24295.

- (246) Lv, H.; Wang, S.; Sun, Y.; Chen, J.; Zhou, W.; Zhang, C. Anode Catalyst Layer with Hierarchical Pore Size Distribution for Highly Efficient Proton Exchange Membrane Water Electrolysis. *J. Power Sources* **2023**, *564*, 232878.
- (247) Yuan, S.; Zhao, C.; Mei, X.; Shen, S.; Wang, Q.; Yan, X.; Zhang, J. Bubble Management in PEM Water Electrolysis via Imprinting Patterned Grooves on Catalyst Layer. *Int. J. Heat Mass Transfer* **2023**, 212, 124249.
- (248) Tao, L.; Lv, F.; Wang, D.; Luo, H.; Lin, F.; Gong, H.; Mi, H.; Wang, S.; Zhang, Q.; Gu, L.; Luo, M.; Guo, S. Mass-Efficient Catalyst Layer of Hierarchical Sub-Nanosheets on Nanowire for Practical Proton Exchange Membrane Electrolyzer. *Joule* **2024**, *8*, 450–460.
- (249) Mo, J.; Kang, Z.; Retterer, S. T.; Cullen, D. A.; Toops, T. J.; Green, J. B.; Mench, M. M.; Zhang, F.-Y. Discovery of True Electrochemical Reactions for Ultrahigh Catalyst Mass Activity in Water Splitting. *Science Adv.* **2016**, *2*, No. e1600690.
- (250) Kang, Z.; Mo, J.; Yang, G.; Retterer, S. T.; Cullen, D. A.; Toops, T. J.; Green, J. B., Jr; Mench, M. M.; Zhang, F.-Y. Investigation of Thin/Well-Tunable Liquid/Gas Diffusion Layers Exhibiting Superior Multifunctional Performance in Low-Temperature Electrolytic Water Splitting. *Energy Environ. Sci.* 2017, 10, 166–175.
- (251) Mo, J.; Kang, Z.; Yang, G.; Li, Y.; Retterer, S. T.; Cullen, D. A.; Toops, T. J.; Bender, G.; Pivovar, B. S.; Green Jr, J. B.; Zhang, F.-Y. In Situ Investigation on Ultrafast Oxygen Evolution Reactions of Water Splitting in Proton Exchange Membrane Electrolyzer Cells. *J. Mater. Chem. A* **2017**, *5*, 18469–18475.
- (252) Wang, W.; Yu, S.; Li, K.; Ding, L.; Xie, Z.; Li, Y.; Yang, G.; Cullen, D. A.; Yu, H.; Kang, Z.; Wrubel, J. A.; Ma, Z.; Bender, G.; Capuano, C. B.; Keane, A.; Zhang, F.-Y. Insights into the Rapid Two-Phase Transport Dynamics in Different Structured Porous Transport Layers of Water Electrolyzers through High-Speed Visualization. *J. Power Sources* **2021**, *516*, 230641.
- (253) Wang, W.; Ding, L.; Xie, Z.; Yu, S.; Capuano, C. B.; Keane, A.; Ayers, K.; Zhang, F.-Y. 3D Structured Liquid/Gas Diffusion Layers with Flow Enhanced Microchannels for Proton Exchange Membrane Electrolyzers. *Energy Convers. Manage.* **2023**, 296, 117665.
- (254) Dedigama, I.; Angeli, P.; Ayers, K.; Robinson, J. B.; Shearing, P. R.; Tsaoulidis, D.; Brett, D. J. L. In Situ Diagnostic Techniques for Characterisation of Polymer Electrolyte Membrane Water Electrolysers Flow Visualisation and Electrochemical Impedance Spectroscopy. *Int. J. Hydrogen Energy* **2014**, *39*, 4468–4482.
- (255) Mishima, K.; Hibiki, T. Some Characteristics of Air-Water Two-Phase Flow in Small Diameter Vertical Tubes. *Int. J. Multiphase Flow* **1996**, 22, 703–712.
- (256) Wan, L.; Xu, Z.; Xu, Q.; Wang, P.; Wang, B. Overall Design of Novel 3D-Ordered MEA with Drastically Enhanced Mass Transport for Alkaline Electrolyzers. *Energy Environ. Sci.* **2022**, *15*, 1882–1892.
- (257) Rox, H.; Bashkatov, A.; Yang, X.; Loos, S.; Mutschke, G.; Gerbeth, G.; Eckert, K. Bubble Size Distribution and Electrode Coverage at Porous Nickel Electrodes in a Novel 3-Electrode Flowthrough Cell. *Int. J. Hydrogen Energy* **2023**, *48*, 2892–2905.
- (258) von der Hardt, P.; Röttger, H. Neutron Radiography Handbook: Nuclear Science and Technology; Springer Science & Business Media, 2012.
- (259) Selamet, O. F.; Pasaogullari, U.; Spernjak, D.; Hussey, D. S.; Jacobson, D. L.; Mat, M. In Situ Two-Phase Flow Investigation of Proton Exchange Membrane (PEM) Electrolyzer by Simultaneous Optical and Neutron Imaging. ECS Trans. 2011, 41, 349.
- (260) de Beer, F.; van der Merwe, J.-H.; Bessarabov, D. PEM Water Electrolysis: Preliminary Investigations Using Neutron Radiography. *Physics Procedia* **2017**, *88*, 19–26.
- (261) Seweryn, J.; Biesdorf, J.; Schmidt, T. J.; Boillat, P. Communication—Neutron Radiography of the Water/Gas Distribution in the Porous Layers of an Operating Electrolyser. *J. Electrochem. Soc.* **2016**, *163*, F3009.
- (262) Zhao, B.; Lee, C.; Lee, J. K.; Fahy, K. F.; LaManna, J. M.; Baltic, E.; Jacobson, D. L.; Hussey, D. S.; Bazylak, A. Superhydrophilic

- Porous Transport Layer Enhances Efficiency of Polymer Electrolyte Membrane Electrolyzers. Cell Rep. Phys. Sci. 2021, 2, 100580.
- (263) Lee, C.; Banerjee, R.; Ge, N.; Lee, J. K.; Zhao, B.; Baltic, E.; LaManna, J. M.; Hussey, D. S.; Jacobson, D. L.; Abouatallah, R.; Wang, R.; Bazylak, A. The Effect of Cathode Nitrogen Purging on Cell Performance and in Operando Neutron Imaging of a Polymer Electrolyte Membrane Electrolyzer. *Electrochim. Acta* **2018**, 279, 91–98.
- (264) Selamet, O. F.; Deevanhxay, P.; Tsushima, S.; Hirai, S. Visualization of Gas Bubble Behavior of a Regenerative Fuel Cell in Electrolysis Mode by Soft X-Ray Radiography. *ECS Trans.* **2013**, *58*, 353
- (265) Hoeh, M. A.; Arlt, T.; Manke, I.; Banhart, J.; Fritz, D. L.; Maier, W.; Lehnert, W. In Operando Synchrotron X-Ray Radiography Studies of Polymer Electrolyte Membrane Water Electrolyzers. *Electrochem. Commun.* **2015**, *55*, *55*–*59*.
- (266) Lee, J. K.; Lee, C.; Fahy, K. F.; Kim, P. J.; Krause, K.; LaManna, J. M.; Baltic, E.; Jacobson, D. L.; Hussey, D. S.; Bazylak, A. Accelerating Bubble Detachment in Porous Transport Layers with Patterned Through-Pores. ACS Appl. Energy Mater. 2020, 3, 9676—9684.
- (267) Panchenko, U.; Arlt, T.; Manke, I.; Müller, M.; Stolten, D.; Lehnert, W. Synchrotron Radiography for a Proton Exchange Membrane (PEM) Electrolyzer. *Fuel Cells* **2020**, *20*, 300–306.
- (268) Kulkarni, D.; Huynh, A.; Satjaritanun, P.; O'Brien, M.; Shimpalee, S.; Parkinson, D.; Shevchenko, P.; DeCarlo, F.; Danilovic, N.; Ayers, K. E.; Capuano, C.; Zenyuk, I. V. Elucidating Effects of Catalyst Loadings and Porous Transport Layer Morphologies on Operation of Proton Exchange Membrane Water Electrolyzers. *Appl. Catal.*, B 2022, 308, 121213.
- (269) Leonard, E.; Shum, A. D.; Normile, S.; Sabarirajan, D. C.; Yared, D. G.; Xiao, X.; Zenyuk, I. V. Operando X-Ray Tomography and Sub-Second Radiography for Characterizing Transport in Polymer Electrolyte Membrane Electrolyzer. *Electrochim. Acta* **2018**, 276, 424–433.
- (270) Satjaritanun, P.; O'Brien, M.; Kulkarni, D.; Shimpalee, S.; Capuano, C.; Ayers, K. E.; Danilovic, N.; Parkinson, D. Y.; Zenyuk, I. V. Observation of Preferential Pathways for Oxygen Removal through Porous Transport Layers of Polymer Electrolyte Water Electrolyzers. *iScience* 2020, 23, 101783.
- (271) Leonard, E.; Shum, A. D.; Danilovic, N.; Capuano, C.; Ayers, K. E.; Pant, L. M.; Weber, A. Z.; Xiao, X.; Parkinson, D. Y.; Zenyuk, I. V. Interfacial Analysis of a PEM Electrolyzer Using X-Ray Computed Tomography. Sustainable Energy Fuels 2020, 4, 921–931.
- (272) Kim, P. J.; Lee, C.; Lee, J. K.; Fahy, K. F.; Bazylak, A. In-Plane Transport in Water Electrolyzer Porous Transport Layers with Through Pores. *J. Electrochem. Soc.* **2020**, *167*, 124522.
- (273) Frenkel, D.; Smit, B. Understanding Molecular Simulation: From Algorithms to Applications, 3rd ed.; Academic Press: San Diego, 2023
- (274) Gadea, E. D.; Perez Sirkin, Y. A.; Molinero, V.; Scherlis, D. A. Electrochemically Generated Nanobubbles: Invariance of the Current with Respect to Electrode Size and Potential. *J. Phys. Chem. Lett.* **2020**, *11*, 6573–6579.
- (275) Ma, Y.; Guo, Z.; Chen, Q.; Zhang, X. Dynamic Equilibrium Model for Surface Nanobubbles in Electrochemistry. *Langmuir* **2021**, 37, 2771–2779.
- (276) Xi, W.; Feng, H.; Liu, D.; Chen, L.; Zhang, Y.; Li, Q. Electrocatalytic Generation and Tuning of Ultra-Stable and Ultra-Dense Nanometre Bubbles: An In Situ Molecular Dynamics Study. *Nanoscale* **2021**, *13*, 11242–11249.
- (277) Chen, Q.; Liu, Y.; Edwards, M. A.; Liu, Y.; White, H. S. Nitrogen Bubbles at Pt Nanoelectrodes in a Nonaqueous Medium: Oscillating Behavior and Geometry of Critical Nuclei. *Anal. Chem.* **2020**, *92*, 6408.
- (278) Liu, Y.; Zhang, X. A Review of Recent Theoretical and Computational Studies on Pinned Surface Nanobubbles. *Chin. Phys. B* **2018**, 27, 014401.

- (279) Liu, Y.; Zhang, X. A Unified Mechanism for the Stability of Surface Nanobubbles: Contact Line Pinning and Supersaturation. *J. Chem. Phys.* **2014**, *141*, 134702.
- (280) Maheshwari, S.; Van Kruijsdijk, C.; Sanyal, S.; Harvey, A. D. Nucleation and Growth of a Nanobubble on Rough Surfaces. *Langmuir* **2020**, *36*, 4108–4115.
- (281) Hu, S.; Guo, B.; Ding, S.; Yang, F.; Dang, J.; Liu, B.; Gu, J.; Ma, J.; Ouyang, M. A Comprehensive Review of Alkaline Water Electrolysis Mathematical Modeling. *Appl. Energy* **2022**, *327*, 120099.
- (282) Taqieddin, A.; Allshouse, M. R.; Alshawabkeh, A. N. Review—Mathematical Formulations of Electrochemically Gas-Evolving Systems. *J. Electrochem. Soc.* **2018**, *165*, No. E694.
- (283) Taqieddin, A.; Nazari, R.; Rajic, L.; Alshawabkeh, A. Review—Physicochemical Hydrodynamics of Gas Bubbles in Two Phase Electrochemical Systems. *J. Electrochem. Soc.* **2017**, *164*, No. E448.
- (284) Epstein, P. S.; Plesset, M. S. On the Stability of Gas Bubbles in Liquid-Gas Solutions. *J. Chem. Phys.* **1950**, *18*, 1505–1509.
- (285) Vogt, H. The Concentration Overpotential of Gas Evolving Electrodes as a Multiple Problem of Mass Transfer. *J. Electrochem. Soc.* **1990**, *137*, 1179.
- (286) Vogt, H.; Balzer, R. J. The Bubble Coverage of Gas-Evolving Electrodes in Stagnant Electrolytes. *Electrochim. Acta* **2005**, *50*, 2073–2079.
- (287) Vogt, H. The Actual Current Density of Gas-Evolving Electrodes—Notes on the Bubble Coverage. *Electrochim. Acta* **2012**, 78, 183–187.
- (288) Landau, L. D.; Lifshitz, E. M. Fluid Mechanics: Landau and Lifshitz: Course of Theoretical Physics, Vol. 6; Elsevier Science & Technology: San Diego, United Kingdom, 1987.
- (289) Sokolichin, A.; Eigenberger, G.; Lapin, A.; Lübert, A. Dynamic Numerical Simulation of Gas-Liquid Two-Phase Flows Euler/Euler versus Euler/Lagrange. *Chem. Eng. Sci.* 1997, 52, 611–626.
- (290) Mandin, P.; Hamburger, J.; Bessou, S.; Picard, G. Modelling and Calculation of the Current Density Distribution Evolution at Vertical Gas-Evolving Electrodes. *Electrochim. Acta* **2005**, *51*, 1140–1156
- (291) Hreiz, R.; Abdelouahed, L.; Fuenfschilling, D.; Lapicque, F. Electrogenerated Bubbles Induced Convection in Narrow Vertical Cells: PIV Measurements and Euler-Lagrange CFD Simulation. *Chem. Eng. Sci.* **2015**, *134*, 138–152.
- (292) Higuera, F. J. Evolution of Hydrogen Bubbles at the Surface of a Porous Horizontal Cathode. *Phys. Rev. Fluids* **2022**, *7*, 113602.
- (293) El-Askary, W. A.; Sakr, I. M.; Ibrahim, K. A.; Balabel, A. Hydrodynamics Characteristics of Hydrogen Evolution Process through Electrolysis: Numerical and Experimental Studies. *Energy* **2015**, *90*, 722–737.
- (294) Colli, A. N.; Bisang, J. M. Current and Potential Distribution in Two-Phase (Gas Evolving) Electrochemical Reactors by the Finite Volume Method. *J. Electrochem. Soc.* **2022**, *169*, 034524.
- (295) Colli, A. N.; Bisang, J. M. Considerations about the Gas Fraction in Two-Phase Electrochemical Reactors by Using a Rigorous Hydrodynamic Model. *Chem. Eng. Sci.* **2023**, *276*, 118699.
- (296) Chen, Y.; Lewis, N. S. Numerical Simulation and Modeling of Hydrogen Gas Evolution on Planar and Microwire Array Electrodes. *J. Electrochem. Soc.* **2022**, *169*, 066510.
- (297) Lee, J.; Alam, A.; Park, C.; Yoon, S.; Ju, H. Modeling of Gas Evolution Processes in Porous Electrodes of Zero-Gap Alkaline Water Electrolysis Cells. *Fuel* **2022**, *315*, 123273.
- (298) Thorsen, T.; Maerkl, S. J.; Quake, S. R. Microfluidic Large-Scale Integration. *Science* **2002**, 298, 580–584.
- (299) Ajaev, V. S.; Homsy, G. M. Modelling Shapes and Dynamics of Confined Bubbles. *Annu. Rev. Fluid Mech.* **2006**, *38*, 277–307.
- (300) Xu, W.; Lu, Z.; Sun, X.; Jiang, L.; Duan, X. Superwetting Electrodes for Gas-Involving Electrocatalysis. *Acc. Chem. Res.* **2018**, *51*, 1590–1598.
- (301) Liu, M.; Wang, S.; Jiang, L. Nature-Inspired Superwettability Systems. *Nat. Rev. Mater.* **2017**, *2*, 1–17.

- (302) Ma, R.; Wang, J.; Yang, Z.; Liu, M.; Zhang, J.; Jiang, L. Bioinspired Gas Bubble Spontaneous and Directional Transportation Effects in an Aqueous Medium. *Adv. Mater.* **2015**, *27*, 2384–2389.
- (303) Xiao, X.; Zhang, C.; Ma, H.; Zhang, Y.; Liu, G.; Cao, M.; Yu, C.; Jiang, L. Bioinspired Slippery Cone for Controllable Manipulation of Gas Bubbles in Low-Surface-Tension Environment. *ACS Nano* **2019**, *13*, 4083–4090.
- (304) Chatenet, M.; Pollet, B. G.; Dekel, D. R.; Dionigi, F.; Deseure, J.; Millet, P.; Braatz, R. D.; Bazant, M. Z.; Eikerling, M.; Staffell, I.; Balcombe, P.; Shao-Horn, Y.; Schafer, H. Water Electrolysis: From Textbook Knowledge to the Latest Scientific Strategies and Industrial Developments. *Chem. Soc. Rev.* **2022**, *51*, 4583–4762.
- (305) Bewig, K. W.; Zisman, W. A. The Wetting of Gold and Platinum by Water. *J. Phys. Chem.* **1965**, *69*, 4238–4242.
- (306) Schrader, M. E. Wettability of Clean Metal Surfaces. J. Colloid Interface Sci. 1984, 100, 372–380.
- (307) Teschke, O.; Galembeck, F. A New Type of Separator for High Temperature Water Electrolyzers. *J. Electrochem. Soc.* **1983**, *130*, **33**.
- (308) Teschke, O.; Galembeck, F. Effect of PTFE Coverage on the Performance of Gas Evolving Electrodes. *J. Electrochem. Soc.* **1984**, 131, 1095.
- (309) Kleinke, M. U.; de Moraes, M. A. B.; Teschke, O. A New Type of PTFE-Covered Gas Evolving Electrode. *J. Electrochem. Soc.* **1986**, 133, 1815.
- (310) Heidrich, H.-J.; Müller, L. The Effect of Hydrophobic Centres on the Electrode Surface on Overvoltage in Electrochemical Gas Evolution. *Electrochim. Acta* **1990**, *35*, 1089–1093.
- (311) Ho, C. N.; Hwang, B. J. Effect of Hydrophobicity on the Hydrophobic-Modified Polytetrafluoroethylene/PbO<sub>2</sub> Electrode towards Oxygen Evolution. *J. Electroanal. Chem.* **1994**, 377, 177–190.
- (312) Brussieux, C.; Viers, Ph.; Roustan, H.; Rakib, M. Controlled Electrochemical Gas Bubble Release from Electrodes Entirely and Partially Covered with Hydrophobic Materials. *Electrochim. Acta* **2011**, *56*, 7194–7201.
- (313) Jeon, D.; Park, J.; Shin, C.; Kim, H.; Jang, J.-W.; Lee, D. W.; Ryu, J. Superaerophobic Hydrogels for Enhanced Electrochemical and Photoelectrochemical Hydrogen Production. *Science Adv.* **2020**, *6*, No. 2023, 3944.
- (314) Bae, M.; Kang, Y.; Lee, D. W.; Jeon, D.; Ryu, J. Superaerophobic Polyethyleneimine Hydrogels for Improving Electrochemical Hydrogen Production by Promoting Bubble Detachment. *Adv. Energy Mater.* **2022**, *12*, 2201452.
- (315) Kang, Y.; Lee, S.; Han, S.; Jeon, D.; Bae, M.; Choi, Y.; Lee, D. W.; Ryu, J. Versatile, Stable, and Scalable Gel-Like Aerophobic Surface System (GLASS) for Hydrogen Production. *Adv. Funct. Mater.* **2024**, 34, 2308827.
- (316) Kern, W. The Evolution of Silicon Wafer Cleaning Technology. J. Electrochem. Soc. 1990, 137, 1887.
- (317) Wang, Q.; Yao, X.; Liu, H.; Quéré, D.; Jiang, L. Self-Removal of Condensed Water on the Legs of Water Striders. *Proc. Natl. Acad. Sci. U.S.A.* **2015**, *112*, 9247–9252.
- (318) Song, Q.; Xue, Z.; Liu, C.; Qiao, X.; Liu, L.; Huang, C.; Liu, K.; Li, X.; Lu, Z.; Wang, T. General Strategy to Optimize Gas Evolution Reaction via Assembled Striped-Pattern Superlattices. *J. Am. Chem. Soc.* **2020**, *142*, 1857–1863.
- (319) Lake, J. R.; Soto, Á. M.; Varanasi, K. K. Impact of Bubbles on Electrochemically Active Surface Area of Microtextured Gas-Evolving Electrodes. *Langmuir* **2022**, *38*, 3276–3283.
- (320) Wang, J.; Zheng, Y.; Nie, F.-Q.; Zhai, J.; Jiang, L. Air Bubble Bursting Effect of Lotus Leaf. *Langmuir* **2009**, 25, 14129–14134.
- (321) Lu, Z.; Zhu, W.; Yu, X.; Zhang, H.; Li, Y.; Sun, X.; Wang, X.; Wang, H.; Wang, J.; Luo, J.; Lei, X.; Jiang, L. Ultrahigh Hydrogen Evolution Performance of Under-Water "Superaerophobic" MoS<sub>2</sub> Nanostructured Electrodes. *Adv. Mater.* **2014**, *26*, 2683–2687.
- (322) Li, Y.; Zhang, H.; Xu, T.; Lu, Z.; Wu, X.; Wan, P.; Sun, X.; Jiang, L. Under-Water Superaerophobic Pine-Shaped Pt Nanoarray Electrode for Ultrahigh-Performance Hydrogen Evolution. *Adv. Funct. Mater.* **2015**, 25, 1737–1744.

- (323) Akbar, K.; Hussain, S.; Truong, L.; Roy, S. B.; Jeon, J. H.; Jerng, S.-K.; Kim, M.; Yi, Y.; Jung, J.; Chun, S.-H. Induced Superaerophobicity onto a Non-Superaerophobic Catalytic Surface for Enhanced Hydrogen Evolution Reaction. *ACS Appl. Mater. Interfaces* **2017**, *9*, 43674–43680.
- (324) Zhang, Q.; Li, P.; Zhou, D.; Chang, Z.; Kuang, Y.; Sun, X. Superaerophobic Ultrathin Ni-Mo Alloy Nanosheet Array from In Situ Topotactic Reduction for Hydrogen Evolution Reaction. *Small* **2017**, *13*. DOI: 10.1002/smll.201701648.
- (325) Shan, X.; Liu, J.; Mu, H.; Xiao, Y.; Mei, B.; Liu, W.; Lin, G.; Jiang, Z.; Wen, L.; Jiang, L. An Engineered Superhydrophilic/Superaerophobic Electrocatalyst Composed of the Supported CoMoS<sub>x</sub> Chalcogel for Overall Water Splitting. *Angew. Chem., Int. Ed.* **2020**, *59*, 1659–1665.
- (326) Hao, J.; Yang, W.; Huang, Z.; Zhang, C. Superhydrophilic and Superaerophobic Copper Phosphide Microsheets for Efficient Electrocatalytic Hydrogen and Oxygen Evolution. *Adv. Mater. Interfaces* **2016**, *3*, 1600236.
- (327) Wendt, H.; Plzak, V. Electrocatalytic and Thermal Activation of Anodic Oxygen-and Cathodic Hydrogen-Evolution in Alkaline Water Electrolysis. *Electrochim. Acta* 1983, 28, 27–34.
- (328) Hall, D. E. Electrodes for Alkaline Water Electrolysis. J. Electrochem. Soc. 1981, 128, 740.
- (329) Ahn, S. H.; Choi, I.; Park, H.-Y.; Hwang, S. J.; Yoo, S. J.; Cho, E.; Kim, H.-J.; Henkensmeier, D.; Nam, S. W.; Kim, S.-K.; Jang, J. H. Effect of Morphology of Electrodeposited Ni Catalysts on the Behavior of Bubbles Generated during the Oxygen Evolution Reaction in Alkaline Water Electrolysis. *Chem. Commun.* **2013**, 49, 9323–9325.
- (330) Rocha, F.; Delmelle, R.; Georgiadis, C.; Proost, J. Electrochemical Performance Enhancement of 3D Printed Electrodes Tailored for Enhanced Gas Evacuation during Alkaline Water Electrolysis. *Adv. Energy Mater.* **2023**, *13*, 2203087.
- (331) Koj, M.; Gimpel, T.; Schade, W.; Turek, T. Laser Structured Nickel-Iron Electrodes for Oxygen Evolution in Alkaline Water Electrolysis. *Int. J. Hydrogen Energy* **2019**, *44*, 12671–12684.
- (332) Schalenbach, M.; Kasian, O.; Mayrhofer, K. J. J. An Alkaline Water Electrolyzer with Nickel Electrodes Enables Efficient High Current Density Operation. *Int. J. Hydrogen Energy* **2018**, *43*, 11932–11938.
- (333) Liu, X.; Zou, P.; Song, L.; Zang, B.; Yao, B.; Xu, W.; Li, F.; Schroers, J.; Huo, J.; Wang, J.-Q. Combinatorial High-Throughput Methods for Designing Hydrogen Evolution Reaction Catalysts. *ACS Catal.* **2022**, *12*, 3789–3796.
- (334) Ma, H.; Cao, M.; Zhang, C.; Bei, Z.; Li, K.; Yu, C.; Jiang, L. Directional and Continuous Transport of Gas Bubbles on Superaerophilic Geometry-Gradient Surfaces in Aqueous Environments. *Adv. Funct. Mater.* **2018**, *28*, 1705091.
- (335) Zhang, J.; Dong, F.; Wang, C.; Wang, J.; Jiang, L.; Yu, C. Integrated Bundle Electrode with Wettability-Gradient Copper Cones Inducing Continuous Generation, Directional Transport, and Efficient Collection of H<sub>2</sub> Bubbles. ACS Appl. Mater. Interfaces **2021**, 13, 32435–32441.
- (336) Winther-Jensen, O.; Chatjaroenporn, K.; Winther-Jensen, B.; MacFarlane, D. R. Towards Hydrogen Production Using a Breathable Electrode Structure to Directly Separate Gases in the Water Splitting Reaction. *Int. J. Hydrogen Energy* **2012**, *37*, 8185–8189.
- (337) Li, J.; Zhu, Y.; Chen, W.; Lu, Z.; Xu, J.; Pei, A.; Peng, Y.; Zheng, X.; Zhang, Z.; Chu, S.; Cui, Y. Breathing-Mimicking Electrocatalysis for Oxygen Evolution and Reduction. *Joule* **2019**, *3*, 557–569.
- (338) Jonville, P. Electrolyzer with Released Gas. US4086155A, April 25, 1978. https://patents.google.com/patent/US4086155A/.